

University of Nottingham
UK | CHINA | MALAYSIA

Statistical Analysis in Electromagnetic Compatibility

Thesis submitted to the University of Nottingham for the degree of **Doctor of Philosophy, November 2023.**

Karol Niewiadomski

20214984

Supervised by

David W.P. Thomas
Mark Sumner
Sharmila Sumsurooah
F.B.J. Leferink
Robert Smolenski

Signature _____

Date _____ / _____ / _____

Abstract

Power electronic (PE) converters are electronic devices designed to process electrical power, transforming the input voltage into an output voltage with desired characteristics. Their main function, which is power conversion, is enabled through the usage of switching devices, such as transistors. Due to the rapid development of the Smart Grid (SG) power devices are more often used alongside or close to communication systems, in particular serial communication devices. The operation of the power converters might induce electromagnetic interference (EMI) and bring about malfunction of these communication devices, which poses a challenge in achieving electromagnetic compatibility (EMC) of the system. The range of switching frequencies used in modern power converters corresponds to the conducted EMI range (9 kHz – 30 MHz), and the impact of conducted EMI is highly influenced by the presence of parasitic elements, values of which exhibit uncertain behaviour due to environmental conditions, geometrical layouts of the circuits, and manufacturing tolerances of the circuit elements.

This thesis presents a statistical approach to identify EMI issues that might occur due to the coexistence of power converters and serial communication systems and proposes the use of stochastic simulation, surrogate modelling, and statistical analysis to compare methodologies for EMI reduction, iden-

tify the most influential parasitic elements and enable optimization of PE circuits.

Firstly, it presents two mathematical models for analysing EMI induced by PE converters when the switching function is realized with Random Modulation (RanM) and Deterministic Modulation (DetM) techniques, along with a novel averaging scheme to facilitate their comparison, thereby overcoming the existing limitations of the models and enhancing its ability to directly calculate the probability of communication error. Contrary to expectations posed by many researchers, the research found that RanM does not improve EMC compliance in the context of PE converter's impact on serial communication devices, with RanM and DetM demonstrating similar influences on average. Additionally, the thesis determined that a Polynomial Chaos (PC)-based surrogate model outperforms Support Vector Machines (SVM) in modelling complex PE converters as judged by prediction error and stability against Monte Carlo simulations. Finally, it presents a methodology using Sobol' indices derived from the PC model to identify and optimize the most sensitive parasitic elements in PE converters, aiming to mitigate the influence of EMI on communication error probability.

This thesis provides the EMC engineers and system integrators methods to validate their approaches for achieving EMC compliance. Accompanying the thesis is an open source toolbox 'UQSpice' that allows to use the methods presented in this thesis for performing PC-based simulations and sensitivity analysis using an LTSpice circuit simulation software.

Acknowledgements

'Oh boy, it's probably over!' I know, maybe it's not the most gentle and desirable thought, but I can assure that most Ph.D. candidates think exactly this when the final is approaching. The last four years have been long and difficult, marked by the COVID pandemic and the war in Ukraine, the latter not having directly influenced me but many of my Ukrainian and Polish friends. Therefore, I am even more grateful that I was able to submit a Ph.D. thesis during these difficult times.

This thesis is an outcome of the Marie Skłodowska-Curie Actions project 'Smart Cities EMC Network for Training'. I am very grateful that I could become part of it, and that the examination board was open to employing a data scientist to help solve EMC problems. For me, this was an opportunity to test the view, conveyed by my math professors and lecturers, that as soon as you know mathematics, statistics and programming, you will manage in another field. Was it true? Well, I had to learn electrical engineering almost from scratch. However, I do believe that after gaining enough insights I was able to look at EMC problems from a different angle, and solve them by mathematical modelling and statistics. I hope this thesis is an example of how interdisciplinary work and collaboration between electrical engineers and data scientists can be beneficial for the EMC world.

I would like to acknowledge those who helped me during this journey. At first Marianna, who had to witness all the ups and downs, signs of ecstasy and depression, and bravely was always there to support me. Secondly, my parents without whom I would not be in a position to make any decision at all. My supervisors, Dave Thomas, Mark Sumner, Sharmila Sumsurooah, Frank Leferink and Robert Smoleński who did their very best to help whenever needed but left enough space for a free and unconstrained research work. I would like to thank Piotr Leżyński and Jacek Bojarski for all the help they offered in both the research work and polishing the manuscript, with their insights and time. Erjon for the time we spent together on col-

laboration and leisure activities that were keeping both of us sane. Niek Moonen and Robert Vogt-Ardatjew for discussions and opportunities given to me. Finally, Krzysztof Przesławski, without whom I would not have finished the Master's thesis on time, and therefore could not have joined the SCENT project, as well as for many discussions during these years.

Contents

Abstract **i**

Acknowledgements **iii**

List of Tables **ix**

List of Figures **x**

Abbreviations **xvii**

Chapter 1 Introduction **1**

1.1 PE converters as EMI sources 1

1.2 Impact of EMI on communication systems 4

1.3 The need for statistical approaches in EMC 5

1.4 Implications of the studies on real-world applications 8

1.5 Research Project - SCENT 12

1.6 Objectives 13

1.7 Contributions 13

1.8 Organization of this thesis 15

1.9 Research papers 15

Chapter 2 Comparative Analysis of Deterministic and Random Modulations **19**

2.1 Literature survey: RanM as an EMI-mitigation technique . . 19

2.2 EMC in Series Communication Systems 30

2.3 Statistical Evaluation of Time-Domain measurements 41

2.4 Comparison of RanM and DetM 52

2.5 Conclusion 60

Chapter 3 Surrogate modelling of EMI circuits **62**

3.1 Motivation 62
3.2 Simulation circuit 69
3.3 Simulations and the Quantity of Interest 77
3.4 Surrogate modelling methods 84
3.5 Validation measure 88
3.6 Conclusion 89

Chapter 4 Surrogate modelling results 90

4.1 Initial Monte Carlo simulations 90
4.2 SVM surrogate modelling results 93
4.3 PC surrogate modelling results 97
4.4 Sensitivity analysis 106
4.5 Discussion 113

Chapter 5 Conclusions 115

5.1 Chapters overview and contributions 115
5.2 Future work 119

Appendices 122

Appendix A Monte Carlo 123

Appendix B Polynomial Chaos 125

B.1 Selection of polynomial basis: Wiener-Askey scheme 126
B.2 Finding the coefficients of a PC model 129
B.3 Sparse Polynomial Chaos 130
B.4 PC-based derivation of moments 131

Appendix C Support Vector Machines 133

C.1 Nonlinearity 135
C.2 Solving the SVM problem 137
C.3 Hyperparameter optimization 139

Appendix D Sensitivity analysis through Sobol' decomposition 142

D.1 Sobol' indices 143
D.2 Estimation of Sobol' indices 144
Bibliography **147**

List of Tables

2.1 Parameters and results of the experiment depicted in Fig. 2.13 with transmission rate 58,409 Hz. 38

2.2 Results of exact binomial test for the investigated frequencies 54

2.3 The number of disrupted bits $L(t_0)$ and probability of error P_{error} for $M = 8$ and $M = 9$, with $D = 3$, $N = 4$ and $n = 6$. . 55

2.4 Exact Binomial test for frequencies higher and lower than 21 kHz and 24 kHz for which p-value $< 10^{-6}$ in the deterministic case. 57

3.1 Input parameters of the circuit under consideration 71

4.1 The 5%, 25%, 50%, 75%, and 95% quantiles of δ and the average value $\mathrm{E}(\delta)$ obtained from the two discussed methods, as well as the corresponding probabilities of frame rejection P_{error} derived for the Random Modulation (RanM) and Deterministic Modulation (DetM) models. 92

4.2 The 5%, 25%, 50%, 75%, and 95% quantiles of δ_1 and δ_2 and the average values $\mathrm{E}(\delta_1)$ and $\mathrm{E}(\delta_2)$, as well as the corresponding probabilities of frame rejection P_{error} derived for the RanM and DetM models. The values for C_{enc} and $C_{\text{MOS}\to\text{GND}}$ satisfy conditions (4.1)–(4.3) and nominal values are assumed for the remaining 41 input parameters. 112

4.3 The 5%, 25%, 50%, 75%, and 95% quantiles of δ_1 and δ_2 and the average values $\mathrm{E}(\delta_1)$ and $\mathrm{E}(\delta_2)$, as well as the corresponding probabilities of frame rejection P_{error} derived for the RanM and DetM models. The values for C_{enc} and $C_{\mathrm{MOS}\to\mathrm{GND}}$ satisfy conditions (4.1)–(4.3) and values for the remaining 41 input parameters are drawn from LHS sampling. 112

B.1 Wiener-Askey scheme for few known distributions. 128

List of Figures

1.1 (a) A simple RLC circuit with a voltage source, (b) The voltage V_R measured across the resistor R after a square impulse. 9

1.2 The voltage V_R for randomly selected values of the parameters R, L and C. 10

2.1 A theoretical explanation of the impact of Spread-Spectrum modulation on the harmonic level, compared to a Deterministic modulation, adopted from [36]. 20

2.2 Spectra of common mode (CM) voltage, obtained from EMI test receiver using (a) deterministic modulation, (b) random modulation, adopted from [51]. 21

2.3 The principle of PWM operation: a) the schematic of a DC/DC converter, b) the square PWM signal with indicated parameters, c) the spectrum of the PWM square signal, d) the spectra of CM and DM voltages obtained from the simulated spectrum analyser. 22

2.4 The effect of modulation the duty cycle on the presence of sideband harmonics. 23

2.5 3D spectrogram of EMI measured according to CISPR 11 using average detector for DetM, switching frequency 80 kHz, from [73]. 26

2.6 3D spectrogram of EMI measured according to CISPR 11 using average detector for randomized switching frequency rate of change control algorithm executed with high rate of change, switching frequency randomized symmetrically around 80 kHz, from [73]. 27
2.7 3D spectrogram of EMI measured according to CISPR 11 using average detector for the same conditions as presented in Fig. 2.6 for the rate of switching frequency change lower than dwell time of digital EMI receiver, switching frequency randomized symmetrically around 80 kHz, from [73]. 28
2.8 The schematic of the DC/DC converter used in the measurements, from [73]. 28
2.9 Half-violin chart of 200 final EMI measurements taken using average detector for 150 kHz and IF BW = 200 Hz, from [73]. 30
2.10 Half-violin chart of 200 final EMI measurements taken using average detector for 150 kHz and IF BW = 9 kHz, from [73]. 30
2.11 Schematic of a system with power supply, DC/DC converter and a load in grounded enclosure, from [75]. 32
2.12 Voltage of two asynchronously controlled converters: a) without coupling and b) with coupling, measured on the load side, from [75]. 33
2.13 The schematic of measuring arrangement consisting of the DC/DC converter injecting the noise to the USB/RS-232 converter through common cables, adopted from [73]. 35
2.14 The laboratory photo of the measuring arrangement from Fig. 2.13, adopted from [73] 36

2.15 Waveforms taken in measuring arrangement: (a) EMI current generated by converter, (b) serial transmission signal with superimposed interference coupled from converter, adopted from [73]. 37
2.16 The results of the experiment from Fig. 2.13: (a) Mean awaiting times for the transmission error, (b) Probability of the transmission error. Adopted from [73]. 39
2.17 Probability of errors obtained from the experiment with DetM and RanM, adopted from [73]. 40
2.18 Experimental voltage waveform with the width of the interference depicted. 41
2.19 A visual interpretation of the random modulation scheme used in developing RanM mathematical model, from [73]. . . 45
2.20 The predictions of RanM mathematical model vs. the experimental results in the RanM case, from [73]. 47
2.21 A visual interpretation of the deterministic modulation scheme used in developing DetM mathematical model, from [73]. . . 49
2.22 Predictions of the DetM mathematical model vs. results of the experimental investigation for DetM case, from [73]. . . . 52
2.23 Predictions of the deterministic model, simulated with a small frequency step, from [73]. 54
2.24 The probability of error predictions of the RanM and DetM models for the switching frequency range 0.01 MHz and 1 MHz; a) a direct evaluation of the mathematical models, b) the average trend of the error probability predictions using the mathematical models. Adopted from [73]. 59

3.1 Impedance measurement of two cables. 63
3.2 The experimental setup. 64

3.3 Line-to-Line and Line-to-Neutral measurements. 65
3.4 Capacitance and equivalent series resistance measurements of 3 different RIFA capacitors. 66
3.5 The experimental setup with the 470 pF RIFA capacitors placed between the DC/DC converter and the ground. . . . 66
3.6 Damped oscillation of the common mode current and output voltage obtained from the experimental setup presented in Fig. 3.5. 67
3.7 The schematic of the Wolfspeed Cree KIT-CRD-3DD065P Buck-Boost circuit used for the simulations. 70
3.8 Histogram of L obtained from 10,000 Monte Carlo samples using Eq. (3.2) with indicated $\mathrm{E}(L)$, $\mathrm{E}(L) + / - \mathrm{Std}(L)$, $\mathrm{E}(L) + / - 2\,\mathrm{Std}(L)$, and $\mathrm{E}(L) + / - 3\,\mathrm{Std}(L)$. 76
3.9 Time domain signals obtained from simulations. 78
3.10 Common and differential mode voltages obtained from the Matlab simulation. 79
3.11 Scaled output voltage to ground obtained from the simulations considering random values of the parameters. 80
3.12 a) Power spectrum of the voltage-to-ground with 0.1 MHz and 1 MHz indicated by the dashed lines and the envelope of the power spectrum depicted by the red solid line; b) The fragment of the power spectrum between 0.1 MHz and 1 MHz, with the peak of the oscillation frequency indicated by a blue dot and dashed line indicating -3 dB from the peak. 82
3.13 Extraction of δ using the two methods, based solely on time-domain signal and based on frequency-domain signal. 84

4.1 The distributions of δ, obtained from two discussed methods. 91
4.2 The errors $\hat{\epsilon}_{\mathrm{LOO}}$ and $\hat{\epsilon}$ of SVM models for δ_1. 94

4.3 The errors $\hat{\epsilon}_{\text{LOO}}$ and $\hat{\epsilon}$ of SVM models for v_0. 94
4.4 The errors $\hat{\epsilon}_{\text{LOO}}$ and $\hat{\epsilon}$ of SVM models for f. 95
4.5 The errors $\hat{\epsilon}_{\text{LOO}}$ and $\hat{\epsilon}$ of SVM models for λ. 96
4.6 The errors $\hat{\epsilon}_{\text{LOO}}$ and $\hat{\epsilon}$ of SVM models for δ_2. 97
4.7 The errors $\hat{\epsilon}_{\text{LOO}}$ and $\hat{\epsilon}$ of PC models for δ_1. 98
4.8 The errors $\hat{\epsilon}_{\text{LOO}}$ and $\hat{\epsilon}$ of PC models for v_0. 98
4.9 The errors $\hat{\epsilon}_{\text{LOO}}$ and $\hat{\epsilon}$ of PC models for f. 99
4.10 The errors $\hat{\epsilon}_{\text{LOO}}$ and $\hat{\epsilon}$ of PC models for λ. 100
4.11 The errors $\hat{\epsilon}_{\text{LOO}}$ and $\hat{\epsilon}$ of PC models for δ_2. 100
4.12 Correlation plots between the parameters v_0, f and λ of the damped oscillation, and parameters δ_1 and δ_2, with the Pearson correlation coefficient ρ computed for each pair of parameters. 102
4.13 The empirical cumulative distribution functions and corresponding approximations of distributions of δ_1 for the MC, sPC and SVM models, for $K = 50, 100, 150, 200$. 103
4.14 The empirical cumulative distribution functions and corresponding approximations of distributions of v_0 for the MC, sPC and SVM models, for $K = 50, 100, 150, 200$. 104
4.15 The empirical cumulative distribution functions and corresponding approximations of distributions of f for the MC, sPC and SVM models, for $K = 50, 100, 150, 200$. 104
4.16 The empirical cumulative distribution functions and corresponding approximations of distributions of λ for the MC, sPC and SVM models, for $K = 50, 100, 150, 200$. 105
4.17 The empirical cumulative distribution functions and corresponding approximations of distributions of δ_2 for the MC, sPC and SVM models, for $K = 50, 100, 150, 200$. 106
4.18 First-order Sobol' indices obtained from sPC model. 107

4.19 Total Sobol' indices obtained from sPC model. 108
4.20 2D scatter plots of selected parameter values obtained from 5,000 LHS samples with indicated $v_0 \geq V_{\mathrm{th}}$ and $v_0 < V_{\mathrm{th}}$. . . 109
4.21 Samples of C_{enc} and $C_{\mathrm{MOS}\rightarrow\mathrm{GND}}$ obtained from a linear SVM classification model with red and blue colour indicating the two classes. 110

C.1 Visual representation of the ε-parametrized SVM model and support vectors, adopted from [72]. 134

Abbreviations

CAN Controller Area Network.

ChS Charging Station.

CM common mode.

DetM Deterministic Modulation.

DM differential mode.

EMC Electromagnetic Compatibility.

EMI Electromagnetic Interference.

GCD Greatest Common Divisor.

IF BW Intermediate Frequency Bandwidth.

IGBT insulated gate bipolar transistor.

LARS Least-Angle Regression.

LCM Lower Common Multiple.

LHS Latin Hypercube Sampling.

LISN Line Impedance Stabilization Network.

MC Monte Carlo.

MOSFET metal oxide semiconductor field effect transistor.

OLS Ordinary Least Squares.

OMP Orthogonal Matching Pursuit.

PC Polynomial Chaos.

PE Power Electronic.

PLC Power Line Communication.

PWM Pulse Width Modulation.

QoI Quantity of Interest.

RanM Random Modulation.

SCENT Smart Cities EMC Network For Training.

SG Smart Grid.

SP Subspace Pursuit.

sPC sparse Polynomial Chaos.

SVM Support Vector Machine.

SVR Support Vector Regression.

Chapter 1

Introduction

1.1 PE converters as EMI sources

Power Electronic (PE) converters are electronic devices which process the electrical power between power input and power output by converting the raw input voltage to an output voltage with desired characteristics [1]. Generally, PE converters can be classified into [1]:

1. DC/DC converters, which provide conversion from an input DC voltage to an output DC voltage,
2. AC/DC rectifiers, which convert the input AC voltage to an output DC voltage,
3. DC/AC inverters, which transform an input DC voltage to an output AC voltage,
4. and AC/AC converters, which convert input AC voltage to output AC voltage.

In each case magnitude and polarity of the output signal can be adjusted to

specific needs; likewise, in the case of DC/AC and AC/AC converters the frequency of the output voltage can be set to a specified value [2]. The main function of PE converters, i.e. processing power, is achieved by utilization of a switching circuit, which comprises resistors, capacitors, magnetic elements such as transformers and inductors, as well as semiconductor devices, including diodes and transistors [1]. Particularly, in modern PE converters the switching function is realized with power transistors, such as insulated gate bipolar transistor (IGBT) and metal oxide semiconductor field effect transistor (MOSFET), that enable power conversion by transitioning between the states ON (conducting current) and OFF (blocking current flow) at a given switching frequency [3]. Due to high efficiency, PE converters are used in many applications with power requirements ranging from less than one watt (e.g., in portable electronics) to 1,000 Megawatts (e.g., in DC/AC inverters used to convert power from DC transmission lines to AC grid) [1]. Moreover, a general trend is observed of increasing the power density by reducing the size and weight of electrical components that comprise PE converters [4]. To achieve that aim, high switching frequencies are desirable [5], and in currently produced PE converters these are typically in the range between several kHz and few MHz [6–8].

The high-speed switching operation of the transistors results in fast changes of currents and voltages, which create electromagnetic disturbances [8, 9]. Such disturbances can spread as voltages and currents through elements of PE circuits, cables and unintentional conductive connections between different circuits (e.g. through parasitic capacitances between the circuit and its enclosure, or through protective earth wires) or can radiate into the environment as electromagnetic waves [9, 10]. These disturbances are commonly referred to as Electromagnetic Interference (EMI) [5, 7–9]. Because of significant amount of power processed by a PE converter, the levels of

currents and voltages as well as the electromagnetic field can be substantial, and may bring about malfunction of nearby devices [7]. Scientific and engineering field that considers ability of a device to operate within its electromagnetic environment without interfering with other devices under normal operating conditions is known as Electromagnetic Compatibility (EMC) [10, 11].

Because of the range of switching frequencies used by PE converters, most of the EMI-related issues caused by PE converters correspond with the conducted EMI range (9 kHz – 30 MHz) [12]. Of particular interest are the harmonics of the switching frequency, as well as oscillatory currents and voltages that result from resonances between inductive and capacitive elements of the circuits containing PE converters [12]. Due to the development of Smart Grid (SG), which includes incorporation of renewable energy sources into existing power systems, continuous improvement of electric transport and development of charging infrastructure, as well as tight integration of all these systems with metering devices and communication systems [13], more and more PE converters are used as interfaces for providing stable and reliable power conversion [7]. This results in increasing amount of problems occurring in the conducted EMI range [14]. In particular, as one aim of SG development is to achieve seamless communication between electrical systems for both control and metering applications [13], interference between PE devices and communication devices focuses attention of researchers [7, 14].

1.2 Impact of EMI on communication systems

The impact of EMI on communication systems can have several implications, such as degradation or interruption of signal transmission, loss of data, decreased system performance, increased error rates, and susceptibility to security breaches. In extreme situations, EMI can even cause complete system malfunction. These implications have been investigated in the research, especially in the automotive, aerospace and railways sectors, where the trend towards increasing the use of electronic equipment on board is observed, as well as in the industrial sector, which heavily relies on automation and has been recently experiencing integration of Internet of Things (IoT) technologies into industrial systems. Among the many examples, Jeschke *et al.* [15] study the impact of cable emissions on the signal integrity of automotive Ethernet communication and point out the importance of signal integrity to satisfy proper autonomous driving functions; Franco *et al.* [16] indicate the problems with EMI disturbing the railway control signalling systems; Fan *et al.* [17] refer the impact of EMI onto railway communication systems, which includes malfunction of sensors, failure of automatic train protection, and error occurrence in radio module systems; and Schaffenroth *et al.* [18] indicate the problems with data access delays, which prevents the real-time control of industrial process automation.

Moreover, in the context of SG, Leferink [14, 19], and recently Hartman *et al.* [20] and ten Have *et al.* [21, 22] showed that conducted EMI can cause unreliable readings in static energy meters, which may result in obtaining incorrect billing. The conducted EMI range overlaps with the frequency range of Power Line Communication (PLC), which is often utilized in SG

for communication between the power grid and 'smart' devices [23]. Hence, various researchers discuss the harmful EMI impact on PLC [24–27]. Moreover, because SG should enable seamless integration of plug-in electric vehicles [13], the automotive technologies such as Controller Area Network (CAN) are widely discussed, e.g. Basford [28] in his Ph.D. thesis discussed the impact of EMI onto CAN communication, Shirai *et al.* [29] discussed CAN communication failure due to conducted EMI induced by switched-mode power supplies, and Pena-Quintal *et al.* [30] showed the effects of EMI induced by DC/DC converter onto single wired communication link.

In the case of the research presented in this thesis, the direct motivation originated from practical *in situ* EMC work observations of an electric bus charging station, obtained from private communication [31]. In a system consisting of an AC/DC fast Charging Station (ChS) and an electric bus, EMI induced by operation of power converters halted the CAN communication between the ChS and the battery management system, i.e. most commands sent by the battery management system were rejected by the ChS due to errors such as bit flips [31].

1.3 The need for statistical approaches in EMC

The EMC problems such as the ones described above occur more often in the recent years, and the manufacturers and distributors of the electronic equipment, including PE converters, need guidance on how to overcome them. Therefore, regulatory bodies create EMC regulations that manufacturers need to comply with in order to sell their products. In the European Union, such regulation is the 2014/30/EU Directive which is imposed on

the manufacturers and distributors of electrical equipment in order for the equipment to be introduced to the EU market. Article 7 of the 2014/30/EU Directive expects manufacturers of the equipment to ensure it has been designed and manufactured in a way which prevents it from exceeding the levels "above which radio and telecommunications equipment or other equipment cannot operate as intended" [11].

Similar requirements are imposed on manufacturers in the British 'Electromagnetic Compatibility Regulations 2016', which specifies conditions that need to be met for the equipment intended for selling in the UK market [32].

In order to achieve EMC compliance, the PE converter needs to be designed in a way which mitigates the EMI, which is often achieved using EMI filters, optimizing circuit topologies, and selecting appropriate components [33]. The usual way of complying with the requirements is to conduct standardized EMI measurements in the accredited laboratory and verify whether the emissions, tested in the frequency domain, are below limits specified in the standards. According to standardized measurements such as the ones outlined in CISPR 11 [34], one measurement is satisfactory for each frequency point to be compared with the limit lines.

On the one hand, the standardized, measurement-based approach gives rise to so-called 'soft' EMI mitigation techniques, such as RanM [33, 35–49], which help to reduce the emissions in the frequency domain in order for the equipment to pass the standardized tests, however without actually improving the EMC [30, 50–52]. On the other hand, such standardized approaches do not reflect the real-world situations where many uncertainties are present in the environment in which the PE converters operate [53–55]. The sources of uncertainties are varied, and may be attributed to the changes of environmental conditions such as humidity or temperature, as

well as components' ageing, geometric tolerances, or different cable lengths, to name a few. All of this should be considered by the manufacturer to achieve EMC compliance, ideally at the design and simulation stage. Indeed, clause (31) of the 2014/30/EU Directive specifies that the manufacturer must foresee the representative configurations that the apparatus will operate in, or that the EMC assessment should be performed "on the basis of the configuration most likely to cause maximum disturbance and the configuration most susceptible to disturbance" [11].

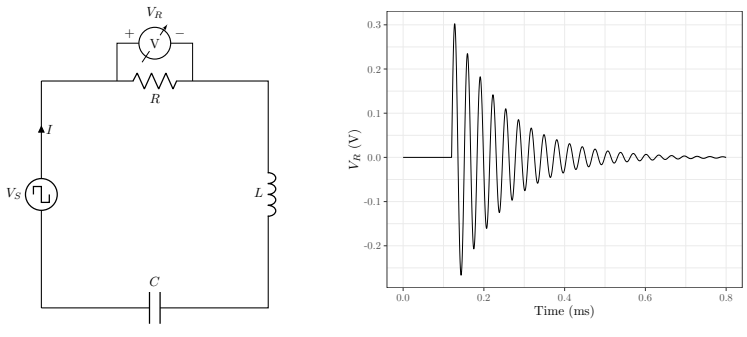
Here is where statistical analysis can help in taking these aspects into account. In the EMC and PE worlds, many researchers discuss the usage of RanM to eliminate or reduce EMI disturbances; new articles regarding RanM are being published every year [9, 35–49, 56–61]. Most researchers perform their EMC assessment in the frequency domain, by comparing values of the harmonics with the limits prescribed in the standards. However, in the context of serial communication systems, the EMC compliance should be assessed by finding the probability with which EMI induced by the operation of converters, influences the communication signal. This has been intuitively understood by some researchers [26, 30, 62], and it has been identified that in such cases the EMC assessment should be performed in the time rather than frequency domain [52, 63]. In this work however, by the application of statistical analysis a comparison between the RanM and DetM will be performed for the first time.

Secondly, statistical analysis can be used to identify the most influential uncertain circuit elements that cause EMI disturbances. This can be done with usage of stochastic simulation methods, correlation plots, statistical hypothesis testing and the analysis of variance approaches. The EMC world has already identified that the presence of uncertainties may influence the EMI [64], and used several techniques which incorporate these uncertainties

into simulations. Among these techniques, the EMC researchers primarily focus on stochastic simulation methods, such as genetic algorithms [65], affine arithmetic [66], unscented transform [67], dimension reduction techniques [68], μ-analysis [69], Polynomial Chaos (PC) [54, 55], and Support Vector Machine (SVM) [70, 71]. However, among the cited works, the author has not identified the ones in which the results of the stochastic simulations are later statistically analysed, the most influential parameters identified and selected to enable optimization of the circuit from the EMC perspective. These two aspects are the gaps that this thesis aims to bridge. In this work, the identified parameters allow reducing the probabilities of errors induced by the operations of PE converters onto communication circuits.

1.4 Implications of the studies on real-world applications

The EMI disturbances are often caused by the presence of parasitic elements which create resonant subcircuits in larger PE circuits [7]. Consider a simple RLC circuit, presented in Fig. 1.1a.



(a) (b)

Figure 1.1: (a) A simple RLC circuit with a voltage source, (b) The voltage V_R measured across the resistor R after a square impulse.

If the circuit is induced with a square impulse, it responds with a damped oscillation signal, which is visible in the measured voltage V_R in Fig. 1.1b. The amplitude, frequency and damping of the oscillation depend on the RLC parameters of the circuit. The frequency f of the damped oscillation signal can be computed from the well-known equation

$$f = \frac{1}{2\pi\sqrt{LC}}, \tag{1.1}$$

where L and C are respectively the inductance and capacitance of the RLC circuit. Depending on the manufacturing tolerances, i.e. how the circuit is made, as well as the environmental conditions, the RLC values may change. In this case f is related with the two parameters L and C, and can be computed directly from Eq. (1.1). However, complexity of real-world circuits makes it hard to identify analytically all the oscillations present in such circuits. Instead, one can assume that the RLC parameters are random variables with a given tolerance and nominal value and perform statistical assessment to collect the parameters of the damped oscillation.

Therefore, some questions that arise are:

- How does the distribution in one or more of the uncertain parameter propagate into the output quantity (for instance the oscillation frequency f)?
- Which uncertain parameters are the most influential on the output quantity?

These questions are tackled in Chapters 3 and 4 of this thesis.

Fig. 1.2 shows three responses of the RLC circuit from Fig. 1.1a where it has been assumed that the RLC parameters have 20% tolerances around

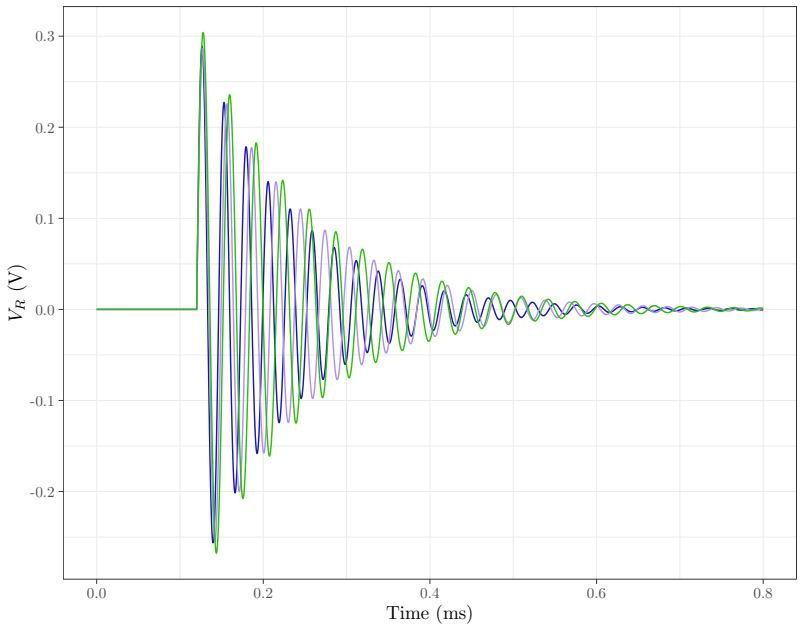


Figure 1.2: The voltage V_R for randomly selected values of the parameters R, L and C.

their nominal values, and their values were randomly selected from uniform distribution. As envisioned in Fig. 1.2, randomly selected RLC values change shapes of the damped oscillation.

Referring to Section 1.3, in the context of serial communication systems, the important information from the EMC compliance point of view is whether the circuit has a significant impact on the probability of errors induced on the communication systems rather than whether the value of the EMI is below a limit line. Indeed, in serial communication systems the value of the bit is established by measuring the instantaneous value of the voltage to ground. If EMI disturbance overlaps with the bit checking moment, the bit value may be corrupted. Whether and for how long these overlaps occur depends on the shape of the damped oscillation disturbances. Clearly, the change of the RLC parameters may bring about reduction or increase of the probability of error occurrence in the communication systems, due to the changing parameters of the EMI disturbances.

The presence of PE converters in proximity to the serial communication is increasingly found in many modern Smart Grid systems [7]. Generally, electric communication systems can be categorized into differential signalling circuits (such as RS-422, RS-485, HDMI, and CAN) and single-ended circuits (such as RS-232, I2C, SPI, and UART). The former uses two complementary signals, which eliminates common impedance coupling and makes communication more resistant to disturbances. Nonetheless, single-ended communication is still commonly implemented in some parts of the system. As an example of a single-ended asymmetric communication, one can consider the universal asynchronous receiver-transmitter (UART). The UART is often used in microcontrollers; for example, 112 different ARM microcontrollers manufactured by Texas Instruments are equipped with at least 2 UART modules out of all 121 ARM microcontrollers produced by this company. Similarly, among the 713 NXP microcontrollers, 683 include at least 2 UARTs[1].

By using additional modules, UART communication may be adjusted to other standards (USB or RS-485). Often, even if we use main transmission links immune to disorders (symmetrical communication, optical fibres, etc.), we still have single-ended parts of the system that might be sensitive to such disorders (short connections, printed boards, signal converters, etc.). Moreover, as discussed in Section 1.2 and shown in [28], differential signalling circuits can be also be susceptible to interference. Thus, the analyses presented in this thesis concern a wide range of microprocessor and communication systems.

Moreover, the problem addressed in this thesis regards the possibility of incorporating uncertain conditions very early at the design stage, using cir-

[1]Based on: https://www.nxp.com and https://www.ti.com (accessed January 2022).

cuit simulation software, and propagate these uncertainties to assess their impact on the communication systems. The developed surrogate models allow finding out the most sensitive parameters and, understand which values of the parameters may bring a reduction of error, thus optimizing the circuit. Furthermore, the methods used in this thesis are easily generalizable, and therefore, this work is applicable to all aspects of EMC, where uncertainty is an issue.

1.5 Research Project - SCENT

This thesis is an outcome of Smart Cities EMC Network For Training (SCENT), project funded by the European Union through Horizon 2020 funding call, grant no. 812391. The project recognizes that enabling the interoperability of electronic systems in Smart and Sustainable Cities faces the challenge related to the complexity of the electromagnetic environment, including the complex relations between the PE converters and communication systems. The project aims to bridge this gap by providing training and creating a network of highly skilled EMC engineers among three universities: University of Twente (UT) in the Netherlands, University of Zielona Gora (UZ) in Poland, and University of Nottingham (UN) in the United Kingdom. In the scope of the project, this thesis is part of the Work Package 6, focused on statistical analysis and grid optimization.

1.6 Objectives

The main objective of this thesis is to show that statistical analysis, including methods such as stochastic simulation, hypothesis testing and sensitiv-

ity analysis, enables solving EMC problems which incorporate uncertainty and randomness.

More specifically, the thesis has the following four objectives:

1. find a way to enable a comparison between RanM and DetM from the perspective of EMC of PE converters operating close to serial communication circuits;
2. verify whether RanM increases the EMC compliance in the context of PE converters' influence on the serial communication devices;
3. identify the suitable method for modelling a PE converter which includes uncertain parasitic elements;
4. find a methodology which identifies the most important parasitic elements that contribute to the EMI, and enable optimizing the circuit.

1.7 Contributions

The contributions of this thesis are as follows.

- This thesis identified two mathematical models that enabled modelling of EMI induced by PE converters, modulated using RanM and DetM techniques. The thesis proposed an averaging scheme that enable to compare RanM and DetM, which was previously not possible due to the limitations of the DetM model. Moreover, these limitations were discussed and the DetM model, originally developed in [63] was enhanced by providing direct calculations of the probability of obtaining an error in the communication (denoted P_{error}) in several special cases.

- This thesis verified that RanM does not increase the EMC compliance with respect to EMI induced by PE converters, operating close to serial communication devices. This result is based on the comparison between RanM and DetM, and it is concluded that on average the two modulation techniques do not differ in the context of PE converters' influence on the serial communication devices.

- The thesis found that a surrogate model based on PC is more suitable than SVM for modelling a complex PE converter which includes uncertain parasitic elements. The two methods were compared between each other and with Monte Carlo (MC) simulations, and the best among them was selected based on the prediction error and stability.

- This work presented a methodology based on Sobol' indices derived from the PC model, which enabled to identify the most sensitive parasitic elements that should be optimized in order to reduce the influence of the EMI disturbances on the probability of error in communication.

The work presented in this thesis is based on three conference and one journal paper authored by the author of this thesis [72–75].

Additional to the work presented here, the author developed a toolbox 'UQSpice' which links a popular simulation tool LTSpice with an uncertainty propagation library OpenTURNS. The toolbox was developed using Python programming language and is available open source on GitHub[2].

[2] https://github.com/karylsienn/UQSpice [online]. Accessed: 14.11.2023.

1.8 Organization of this thesis

The rest of the thesis is organized following the contributions listed above.

In Chapter II the comparative analysis of RanM and DetM with respect to their impact on serial communication devices is discussed.

Chapter III presents the PE circuit used in simulations, discusses modelling of the uncertain parasitic circuit parameters as random variables, and presents the surrogate models PC and SVM used in the analysis.

Chapter IV shows the results of the surrogate modelling and compares two surrogate methods. It also shows the results of the sensitivity analysis through Sobol' indices and presents the identification of the most influential circuit elements.

Finally, Chapter V concludes the thesis, and discusses further possible ways of extending this research, some of which have been already presented at international EMC conferences.

Moreover, the Appendices contain mathematical background regarding the used surrogate models and Sobol' indices.

1.9 Research papers

The following research papers have been authored by the author of this thesis during the course of the SCENT project:

- K. Niewiadomski, R. Smolenski, P. Lezynski, J. Bojarski, D. W. P. Thomas and F. Blaabjerg, "Comparative Analysis of Deterministic and Random Modulations Based on Mathematical Models of Trans-

mission Errors in Series Communication," in *IEEE Transactions on Power Electronics*, vol. 37, no. 10, pp. 11985-11995, Oct. 2022;

- K. Niewiadomski, A. Pena-Quintal, D. W. P. Thomas and S. Sumsurooah, "Sensitivity Analysis of Parasitics in Power Electronic Circuit through Sobol' Indices," *2021 Asia-Pacific International Symposium on Electromagnetic Compatibility (APEMC)*, Nusa Dua - Bali, Indonesia, 2021, pp. 1-4;

- K. Niewiadomski, S. Sumsurooah and D. W. P. Thomas, "Comparison of Selected Support Vector Machine Approaches for Stochastic Power Electronic Circuit Simulation with Parasitics," *2021 IEEE International Joint EMC/SI/PI and EMC Europe Symposium*, Raleigh, NC, USA, 2021, pp. 591-596;

- K. Niewiadomski, P. Lezynski, R. Smolenski, J. Bojarski, M. Sumner and D. W. P. Thomas, "Time-domain Assessment of Data Transmission Errors in Systems with Multiple DC/DC Converters," *2020 International Symposium on Electromagnetic Compatibility - EMC EUROPE,* Rome, Italy, 2020, pp. 1-6.

Additionally, during the course of the SCENT project the author has been a co-author of the following research papers

- E. Ballukja, K. Niewiadomski, D. W. P. Thomas, S. Sumsurooah, M. Sumner and J. Bojarski, "A Statistical Approach to Predict the Low Frequency Common Mode Current in Multi-Converter setups," *2023 IEEE Symposium on Electromagnetic Compatibility & Signal/Power Integrity (EMC+SIPI)*, Grand Rapids, MI, USA, 2023, pp. 7-12;

- E. Ballukja, I. Aitbar, K. Niewiadomski, D. W. P. Thomas, M. Sumner and R. Smolenski, "Stochastic Approach to Modelling Emissions

of Multiple Power Electronic Converters," *2023 IEEE 7th Global Electromagnetic Compatibility Conference (GEMCCON)*, Nusa Dua, Indonesia, 2023, pp. 28-28;

- S. Voskresenskyi, I. Aitbar, E. Ballukja, K. Niewiadomski, D. W. P. Thomas and S. Greedy, "State of the Art of Near-Field Scanning: Contemporary Standards and Methods," *2023 IEEE 7th Global Electromagnetic Compatibility Conference (GEMCCON)*, Nusa Dua, Indonesia, 2023, pp. 29-30;

- E. Ballukja, K. Niewiadomski, A. Pena-Quintal, D. W. P. Thomas, S. Sumsurooah and M. Sumner, "Stochastic Modelling of Power Electronic Converters under Uncertainties," *2022 IEEE International Symposium on Electromagnetic Compatibility & Signal/Power Integrity (EMCSI)*, Spokane, WA, USA, 2022, pp. 232-237;

- A. Pena-Quintal, K. Niewiadomski, S. Greedy, M. Sumner and D. Thomas, "The Influence of the Number of Frequencies and the Frequency Repetitions Rates in Spread Spectrum Sigma-Delta Modulated DC-DC Converters," *2021 Asia-Pacific International Symposium on Electromagnetic Compatibility (APEMC)*, Nusa Dua - Bali, Indonesia, 2021, pp. 1-4;

- A. Pena-Quintal, K. Niewiadomski, V. Muneeswaran, S. Greedy, M. Sumner and D. W. P. Thomas, "The Effect of Spread Spectrum Modulation for a Buck Converter Coupled with a Single Wired Communication Link," *2021 IEEE International Joint EMC/SI/PI and EMC Europe Symposium*, Raleigh, NC, USA, 2021, pp. 445-450;

- A. D. Khilnani et al., "Power Quality Analysis (0-2kHz) in DC/DC Converters under Steady State and Transient Conditions," *2020 In-*

ternational Symposium on Electromagnetic Compatibility - EMC EUROPE, Rome, Italy, 2020, pp. 1-5;

- A. E. Pena-Quintal, M. J. Basford, K. Niewiadomski, S. Greedy, M. Sumner and D. W. P. Thomas, "Data Links Modelling under Radiated EMI and its Impact on Sampling Errors in the Physical Layer," *2020 International Symposium on Electromagnetic Compatibility - EMC EUROPE*, Rome, Italy, 2020, pp. 1-5.

Chapter 2

Comparative Analysis of Deterministic and Random Modulations

This chapter describes the comparison between the random modulation and deterministic modulation, using specially developed mathematical models and statistical techniques. The main body of work presented hereafter was published in [75], presented during the 2020 EMC Europe Symposium, and [73] in IEEE Transactions on Power Electronics.

2.1 Literature survey: RanM as an EMI-mitigation technique

RanM is often treated as an EMI reduction technique, and used to assure the EMC of electronic devices. The reason for using it is commonly related to its cost-effectiveness; instead of investing in expensive filters, a cheap 'at

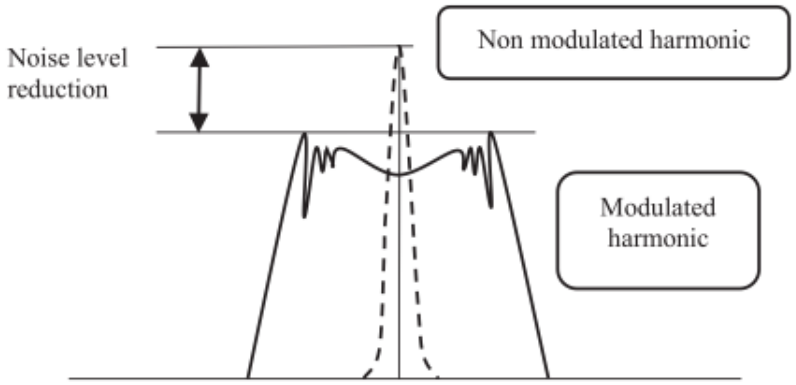


Figure 2.1: A theoretical explanation of the impact of Spread-Spectrum modulation on the harmonic level, compared to a Deterministic modulation, adopted from [36].

source' technique is used that enables to pass the standardized EMC tests. The principle of modulation techniques, in the context of EMC, dwells in dispersing the switching frequency of a PE converter. This spreads the interference over a wider frequency range, which allows to lower the amplitude of the interference with respect to that created by the DetM [76], as shown in Fig. 2.1. As a result, the interference is below the limits prescribed in standards and, therefore, the device passes the tests [60].

To exemplify the considered phenomenon, Fig. 2.2 shows EMI spectra for a CM voltage, obtained from a 3-phase inverter using Rhode & Schwartz ESCS30 EMI test receiver with peak and average detectors and bandwidth 200 Hz, adopted with permission from [51]. In that case, the switching frequency was set to 6 kHz. One can observe the reduction of EMI by looking at the harmonics of the switching frequency, particularly at the indicated 12 kHz. Easily noticeable are the sharp harmonics in the case of a fixed switching frequency, and a dispersion of spectra around the harmonics in the case of a modulated switching frequency. As a result, reduction of 4 dB (from 118.9 dBμV to 114.9 dBμV) and 11.2 dB (from 118.6 dBμV to 107.4 dBμV) is observed when measured with a peak detector and an

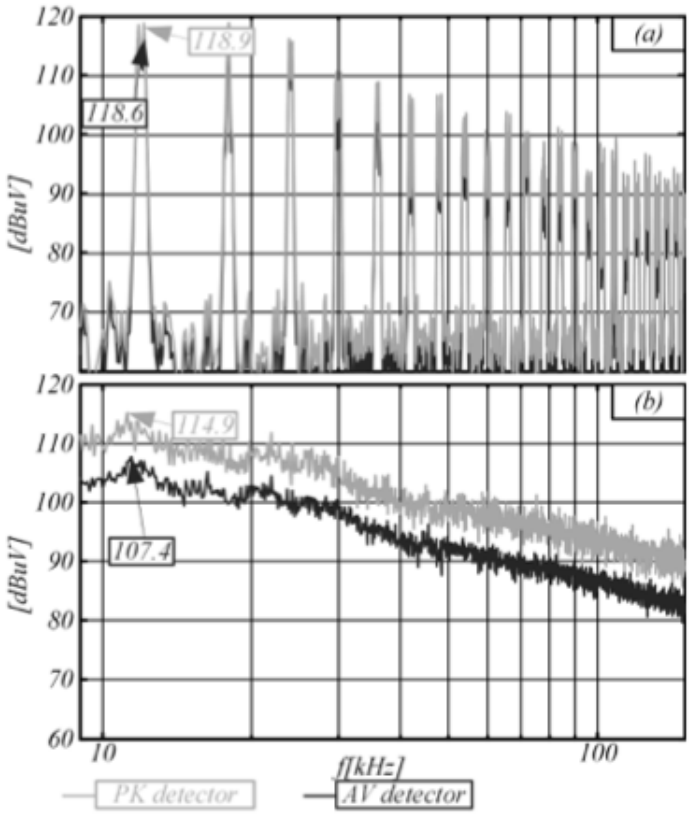


Figure 2.2: Spectra of CM voltage, obtained from EMI test receiver using (a) deterministic modulation, (b) random modulation, adopted from [51].

average detector, respectively.

2.1.1 Principle of PWM operation

Fig. 2.2 (a) presents a typical spectrum of a PE device, in which the switching operation is realized with a Pulse Width Modulation (PWM) driving signal. PWM is a technique widely used in PE converters to control the output amplitude and fundamental switching frequency of the transistors. An idealized PWM operation is explained visually in Fig 2.3, where square wave provides ON and OFF signals for the transistors in a PE circuit, and the spectrum of both the square signal and the spectra for CM and differential mode (DM) voltages are shown.

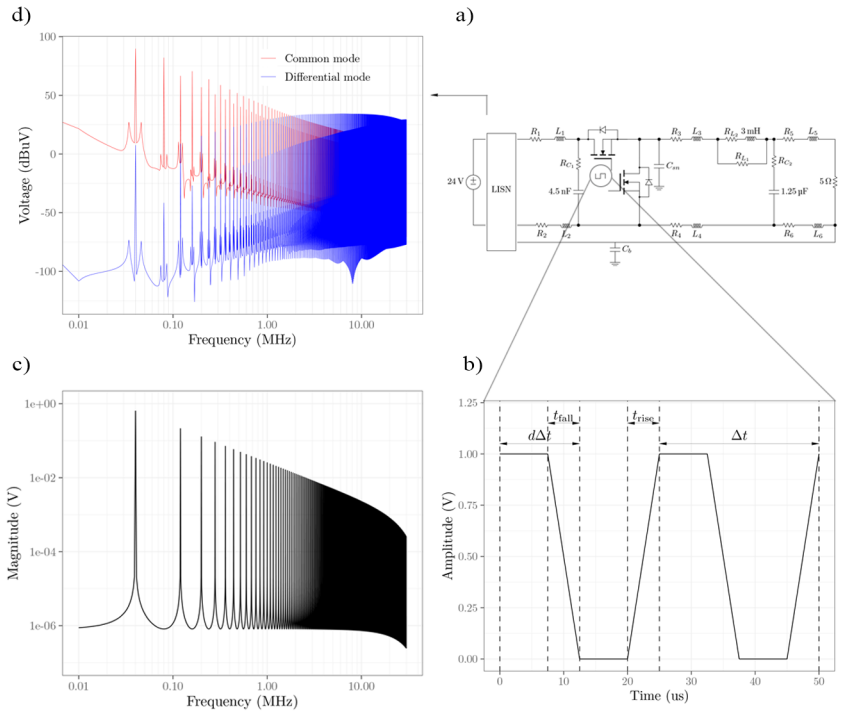


Figure 2.3: The principle of PWM operation: a) the schematic of a DC/DC converter, b) the square PWM signal with indicated parameters, c) the spectrum of the PWM square signal, d) the spectra of CM and DM voltages obtained from the simulated spectrum analyser.

As one can see, harmonics of the square signal are reflected in the CM and DM spectra. However, it is also noticeable that the spectrum of a pure square signal contains only the odd harmonics. This can be understood by considering the expansion of an ideal square wave into Fourier series, which reduces to

$$A_{\mathrm{PWM}}(t) = \frac{4}{\pi} \sum_{k=0}^{\infty} \frac{1}{2k+1} \sin\left(\frac{(2k+1)\pi t}{\Delta t}\right), \tag{2.1}$$

where Δt represents the switching period; the coefficient $2k+1$ indicates the presence of odd harmonics, which remain in the spectrum due to the linearity of a Fourier transformation.

Moreover, Fig. 2.3 indicates the characteristics of a square PWM signal, often used when discussing different PWM techniques. These characteristics

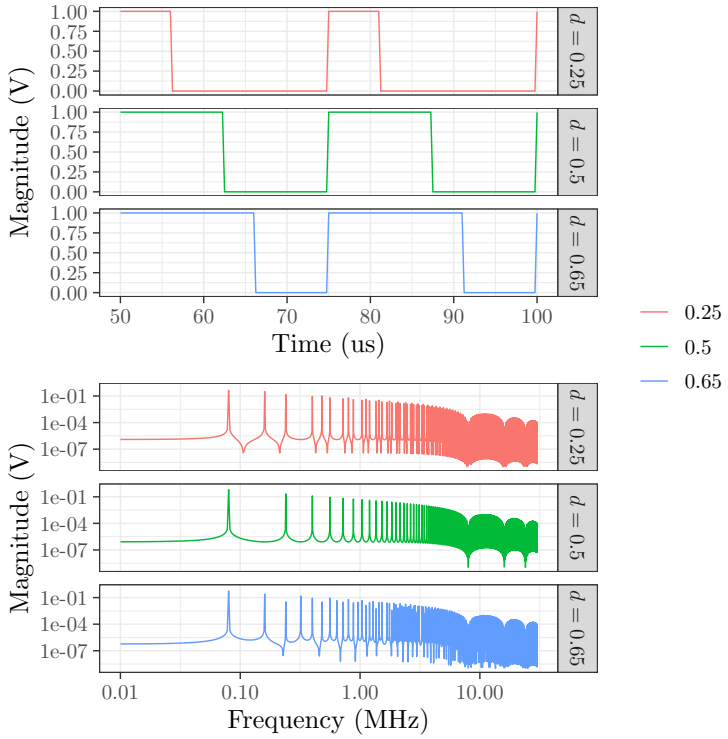


Figure 2.4: The effect of modulation the duty cycle on the presence of sideband harmonics.

are: duty cycle d, time of rising edge t_{rise} and falling edge t_{fall}. Modulating the duty cycle is used to control the output voltage levels [6], and is manifested in the EMI spectra with the presence of so-called sideband harmonics around the fundamental switching frequency, shown in Fig. 2.4 [33].

As most of the high frequency emissions of a PE circuit are due to the fast switching action of the transistors, controlling the rising and falling time enables to therefore tackle some EMC issues by controlling the envelope of the EMI spectra [10].

The remaining spectral content of the CM and DM voltages is related to these characteristics of realistic non-ideal square signals [10], and more importantly with the electrical characteristics of a PE circuit. The rising and falling times will not be considered in the work presented in this chapter, as this would greatly complicate the analyses, while the impact of electrical

parameters of the circuits on the EMI will be discussed in the following chapters.

2.1.2 RanM algorithms

Various techniques have been used for modulating the switching frequency. Chen *et al.* [59] refer so-called Periodic PWM techniques where, as the name suggests, the PWM is changed periodically according to different modulation signals. The techniques can be based on deterministic signals, such as sinusoidal, cubic, triangular or hyperbolic waves [59, 76], as well as probabilistic distributions, such as uniform, normal, or exponential [46, 51, 59, 77].

However, under the same operating conditions, differences between these techniques with respect to obtained reduction of EMI levels can be negligible [59], and therefore, to simplify the analysis, only selected modulation technique can be studied.

In recent years researchers developed an array of techniques for randomizing the PWM operation. Chen *et al.* [35] present EMI reduction of a buck converter using a continuous-time second order delta-sigma modulation and burst-mode techniques. In [36], Gamoudi *et al.* review spread-spectrum-based PWM techniques that enable to meet EMC standards without incurring significant costs. Yang *et al.* [37] use a random number pseudo-hysteresis controller to avoid cyberattack on the Internet-of-Everything devices; as a result they reduce EMI of PE converters without degrading their performance. A hybrid pulse modulation technique was presented in [38], where experiments with a quasi-Z-source DC/DC converter driven by an FPGA showed a 10 dB suppression of EMI. A spread-spectrum technique

was improved with an enhanced phase-shift algorithm and implemented in a 500 W LLC-resonant converter in [44]. EMI mitigation for drive system was achieved with Uniform Distribution Pulse-width Modulation Strategy, presented in [47]. Moon *et al.* [49] propose a spread-spectrum modulated digital PWM for a buck converter in IoT applications, and refer 6.1 dB reduction of EMI levels.

In order to efficiently lower the harmonic peaks, it is desirable to evenly spread the interference over a frequency range. To this end, Dove *et al.* [39] used a random generator based on maximum entropy, Wang *et al.* [41] applied a direct sequence spread spectrum, Li *et al.* [43] used a chaotic sinusoid, Chen *et al.* [46] employed a so-called 'uniform distribution' PWM, and Kim *et al.* [78] proposed spread spectrum technique with random-linear modulation. The variety of techniques indicates a high interest in developing efficient RanM methods; however, regardless of these developments, the principle behind RanM does not change, and the EMI reduction is only apparent, as discussed in the next subsection.

2.1.3 Ostensible reduction of EMI

The aforementioned authors refer various EMI reduction levels. Some researchers reduce EMI by only several decibels [38, 49, 78]. EMI reduction on the scale of 10 to 20 dB is observed in other works [35, 41, 44–46, 48, 76]. Reduction above 20 dB is declared in [36, 47, 77] with Yan *et al.* [37] reaching a 35 dB peak reduction. These results are often perceived as sufficient for the purpose of passing the tests, however are usually outperformed by the application EMI filtering solutions, where reduction of 20 dB and more is achieved.

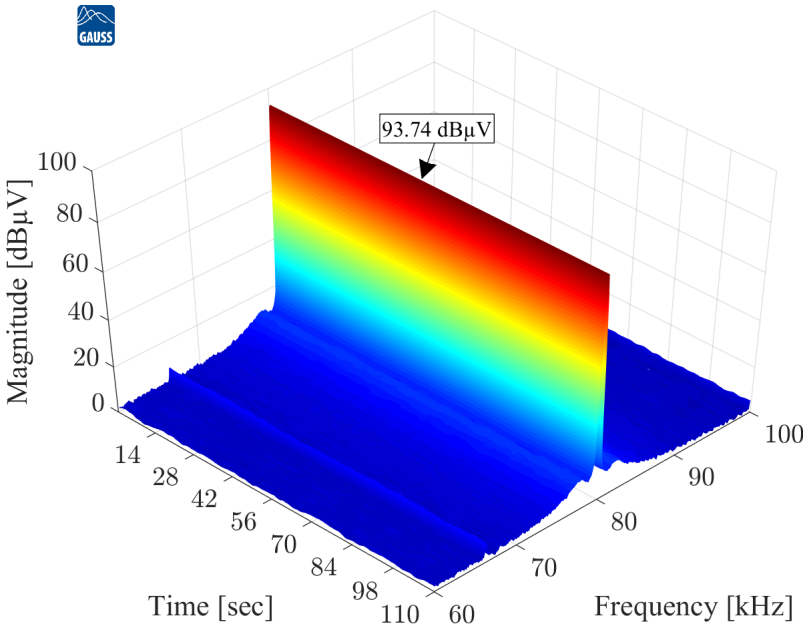


Figure 2.5: 3D spectrogram of EMI measured according to CISPR 11 using average detector for DetM, switching frequency 80 kHz, from [73].

Nevertheless, such variability poses a problem in the interpretation of the influence of RanM on EMI reduction. On the one hand, Lezynski [51] indicates that when reporting the achieved EMI reduction due to RanM, some researchers do not perform their EMI assessment in a standardized manner. On the other hand, if measured according to standards, such as CISPR 11 [34], the reduction of EMI is ostensible, and results from the adopted measurement procedure [52]. More specifically, it depends on the relationship between converters' switching frequency, and the Intermediate Frequency Bandwidth (IF BW) and dwell time of the EMI receiver, as discussed below.

Fig. 2.5 shows 3D EMI spectrogram of a buck converter measured with an average detector according to CISPR 11 [34] using fast, digital TDEMI X6 EMI receiver compliant with CISPR 16-1-1 as well as ANSI C63.2 with dwell time 100 ms. The converter was modulated with DetM and switching frequency equal to 80 kHz. Indicated is the harmonic peak at the switching frequency, the value of which is 93.74 dBμV.

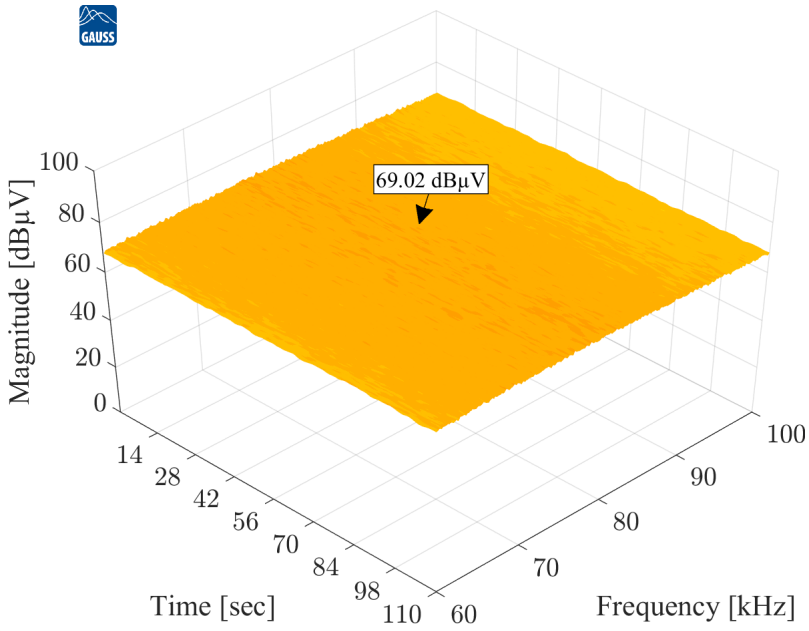


Figure 2.6: 3D spectrogram of EMI measured according to CISPR 11 using average detector for randomized switching frequency rate of change control algorithm executed with high rate of change, switching frequency randomized symmetrically around 80 kHz, from [73].

Fig. 2.6 shows 3D EMI spectrogram, when the RanM algorithm is applied and the switching frequency is spread uniformly around 80 kHz. A reduction of around 33 dB is observed in the RanM case, compared to DetM. However, Fig. 2.7 shows again a RanM algorithm applied to the buck converter but when the rate of change of the switching frequency is slower than the dwell time of the digital EMI receiver, and all other parameters remain the same as in Fig. 2.6. Easily noticeable are the EMI peaks remaining at the original level, i.e. above 90 dBμV. One can therefore hypothesize that the reduction of the interference, seen in Fig. 2.6 is only apparent and does not depend on the applied RanM algorithm but rather on the dwell time of the EMI receiver and its relationship with the rate of change of the switching frequency.

To further test this hypothesis, following the measuring methodology outlined in [7], an experiment was constructed using a converter presented in Fig. 2.8, in a standardized system conforming to CISPR 11 [34]. The

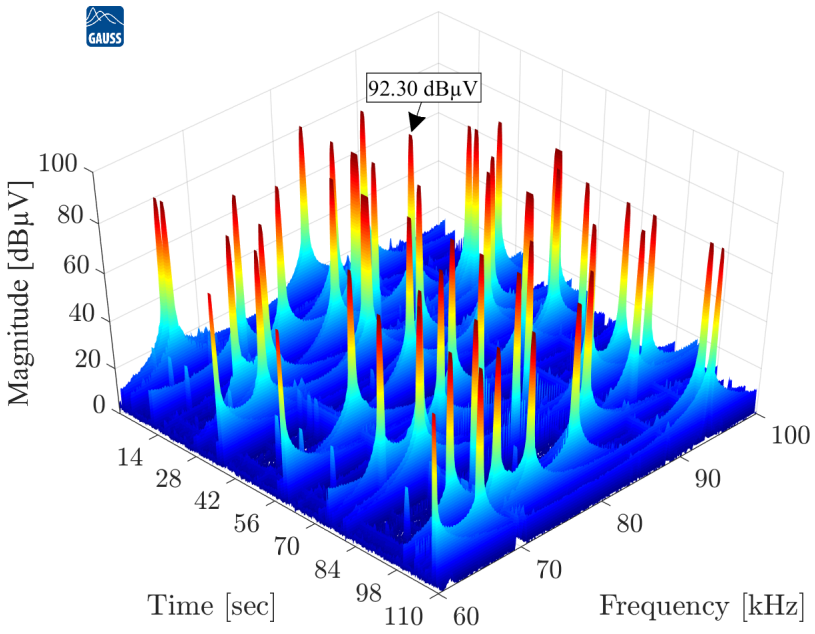


Figure 2.7: 3D spectrogram of EMI measured according to CISPR 11 using average detector for the same conditions as presented in Fig. 2.6 for the rate of switching frequency change lower than dwell time of digital EMI receiver, switching frequency randomized symmetrically around 80 kHz, from [73].

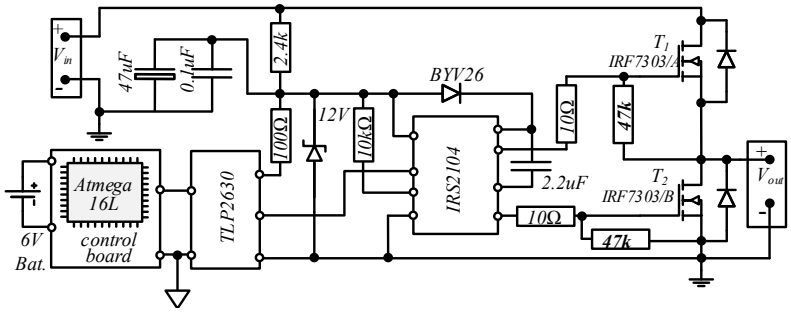


Figure 2.8: The schematic of the DC/DC converter used in the measurements, from [73].

power converter was modulated with a switching frequency equal to 6 kHz in DetM case and dispersed around 6 kHz for RanM. According to [34], to compare the emissions with limits one measurement is required for each frequency point. However, to account for statistical variations, 200 final measurements were collected with an average detector, each with a measuring time equal to 1 s. To see the influence of the receiver's selectivity setting on the results, the comparison was carried out for 150 kHz, which is the 25th harmonic of the converter's switching frequency. The selected frequency is also a border frequency between CISPR A and CISPR B ranges. Both CISPR A and CISPR B are treated as conducted EMI frequency ranges, the former being between 9 kHz and 150 kHz, while the latter starting at 150 kHz and finishing at 30 MHz. However, the IF BW for CISPR A is equal to 200 Hz, while for CISPR B it is equal to 9 kHz, and therefore the EMI for border frequency 150 kHz can be measured with these two selectivity settings.

The results of the measurements are presented in Fig. 2.9 and Fig. 2.10 in the form of distributions. One can observe that if 150 kHz is treated as CISPR A frequency, the RanM algorithm shows a significant reduction of the EMI; indeed, the distributions do not overlap, and therefore there is no need to apply statistical tests to verify whether the results are significantly different. However, the reverse situation is seen on Fig. 2.10: if 150 kHz is treated as CISPR B frequency, applying the RanM algorithm actually increases EMI; again the distributions are clearly separated, without the need to perform statistical tests.

It can be therefore concluded that the receiver's selectivity settings influence the EMI measurements, and as a result, the conclusion about RanM effectiveness. Moreover, in [50], Lezynski *et al.* present a spectrum aggregation technique that allows to compare the DetM and RanM techniques

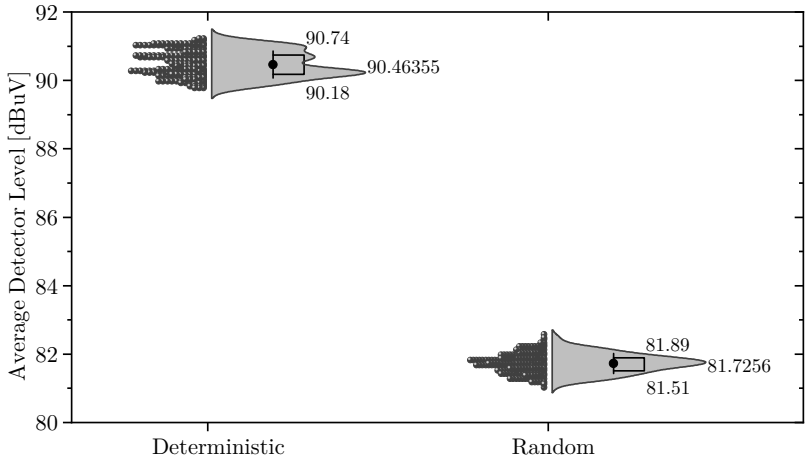


Figure 2.9: Half-violin chart of 200 final EMI measurements taken using average detector for 150 kHz and IF BW = 200 Hz, from [73].

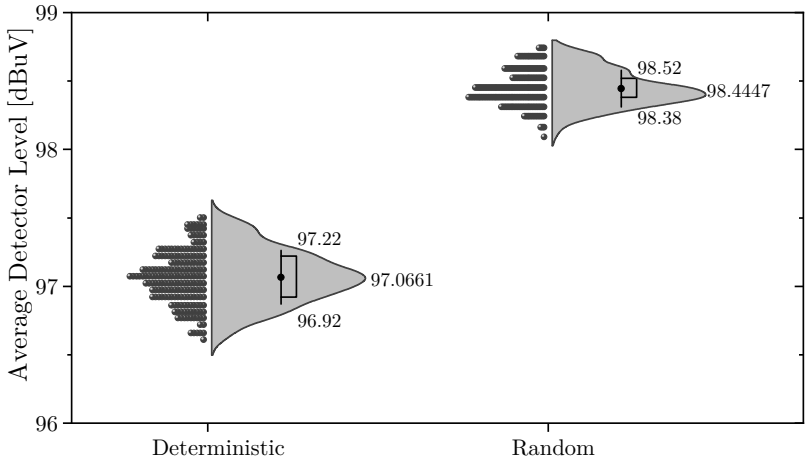


Figure 2.10: Half-violin chart of 200 final EMI measurements taken using average detector for 150 kHz and IF BW = 9 kHz, from [73].

in a more representative way than the currently binding standards; the results presented there confirm that the EMI spectra can be measured in a way which shows that no significant EMI reduction is achieved with RanM.

2.2 EMC in Series Communication Systems

Despite the achieved EMI reduction levels, whether ostensible or not, EMC compliance refers to the ability of not interrupting the work of other devices

in the electromagnetic environment. As already discussed in the Introduction, the concept that sparked interest in these studies originated from observing a real-world EMC problem, i.e. CAN communication being disturbed between the ChS and an electric bus, despite the usage of RanM (see Section 1.2).

The influence of RanM on communication systems has been studied in several research works. In fact, original principles of EMC were oriented towards assuring proper radio-television (RTV) signal reception. To sufficiently simulate an RTV receiver during EMC tests a selective superheterodyne receiver was used, and the interference was evaluated only in the frequency domain [7]. Nowadays, many researchers consider the problem of RanM influence on the communication signal where the communication is realized with PLC [24, 25, 56, 57, 61, 79–83]. In such cases, applying RanM may bring about real benefits, as the nature of PLC modulation is similar to that of the superheterodyne receivers used in EMC tests. An in-depth analysis of such scenarios is given by Musolino and Crovetti in [62] and [26], where the authors consider the problem of EMI and communication channel coexistence in the framework of Shannon's information theory [84]. In particular, they propose to compute the EMI-induced loss of channel capacity by considering the overlap between the EMI and communication channel bandwidths, and the signal-to-noise ratio. This framework has been also adopted to explain why increasing the spread of the RanM may result in reducing channel capacity, presented in works by El-Sayed *et al.* [25, 81], which is counterintuitive with the fact that during EMC tests RanM generally results in a reduction of EMI, albeit apparent.

Under Shannon's framework, adopted by Musolino and Crovetti, if there is little or no overlap between the EMI bandwidth and communication channel frequency range, this should prevent reduction of communication

channel capacity. Therefore, the proposed approach is particularly useful for analysis in PLC applications, as the allowed frequencies for the PLC signal correspond to the conducted EMI frequency ranges. However, in the smart metering and control applications, many communication devices and microprocessors use asymmetric series transmission rather than communication based on selective signal receiving [7]. In this type of transmission, in order to detect a communication signal, one needs to measure the voltage to the ground at specific moment in time. Therefore, the analysis of disturbances in such systems should incorporate examining the signals in time domain; while the proposed framework does not incorporate any time-domain related phenomena. In particular, it does not explain why slightly changing the switching frequency in a DetM increases the communication capacity [31], as discussed in Section 1.2.

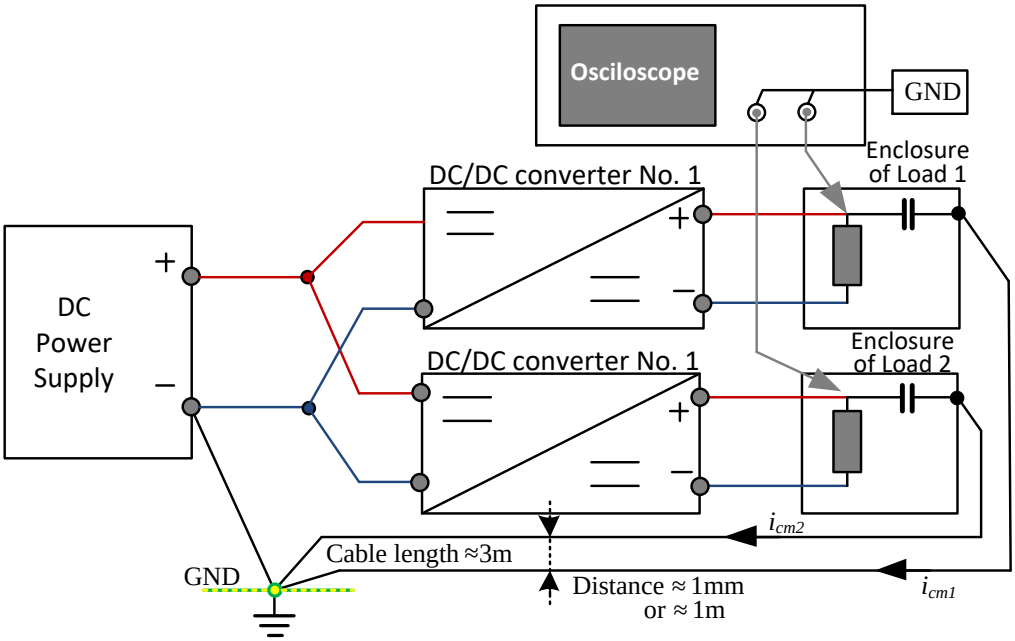


Figure 2.11: Schematic of a system with power supply, DC/DC converter and a load in grounded enclosure, from [75].

As a first step towards understanding what the signals look in time domain, an experiment consisting of two dc/dc converters from Fig 2.8 was devised, the schema of which is shown in Fig. 2.11, representing a simplified scenario

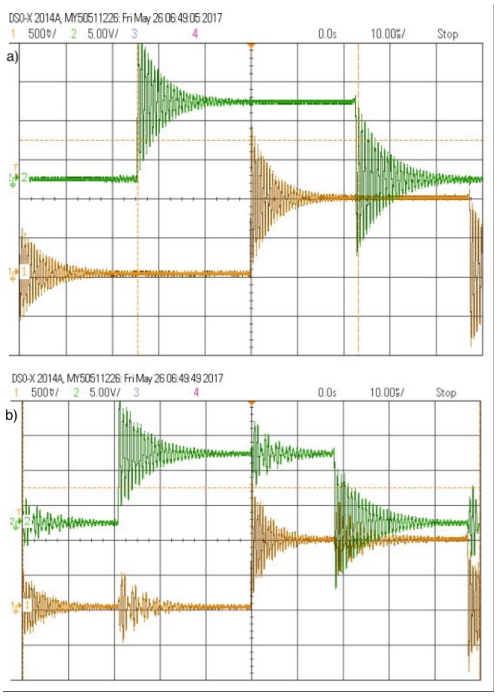


Figure 2.12: Voltage of two asynchronously controlled converters: a) without coupling and b) with coupling, measured on the load side, from [75].

of power electronic converters supplying power to resistive loads, placed in grounded enclosures [75]. In such a scenario, the DM current flows through the load and the internal circuitry, while the CM current i_{CM} flows between the load and its enclosure through the parasitic capacitance. In this example, the parasitic capacitance was simulated by 5 nF capacitors placed between the positive load clamp and grounded cables.

The switching operation of the converters excites the CM current to flow, which in turn leads to voltage drops on the series circuit elements. To see the shapes of these voltages, for each converter voltage-to-ground was measured on the load side. Because of the presence of the parasitic elements, such as the capacitor between load and the grounded enclosure, the voltage drops have the shape of a high frequency damped oscillations, as depicted in Fig. 2.12 a). A single damped oscillation can be modelled as [75]:

$$v(t) = v_0 \sin(2\pi f t) \exp(-\lambda t)\mathbf{1}(t), \tag{2.2}$$

or

$$v(t) = v_0 \cos(2\pi f t) \exp(-\lambda t)\mathbf{1}(t), \tag{2.3}$$

where:

- v_0 is the ringing gain,
- f is the ringing frequency,
- λ is the decay rate,
- $\mathbf{1}(t)$ is the Heaviside (step) function.

Such voltage drops propagate using common impedance, e.g., PE wires and may lead to disturbances of the series communication, as was the case in the scenario discussed in Section 1.2. In Fig. 2.12 b) the result of interference coupling is visible, when the PE wires of the respective converter circuits are brought to a close distance of ∼1 mm, while Fig. 2.12 a) presents a situation in which the PE wires are separated at a large distance of 1 m. It can therefore be seen that separation of the cables may lead to elimination of the interference coupling, which can further prevent the generation of communication disturbances. Nevertheless, as discussed previously in some applications such counteractions are not feasible, and therefore many researchers still discuss using RanM to achieve that aim [30, 35–38, 41, 44–49, 76, 78, 85–87].

2.2.1 Experiments with Series Transmission

Having the initial insight into the shapes of the damped oscillation the hypothesis that the disturbances occur due to the high-frequency oscillations

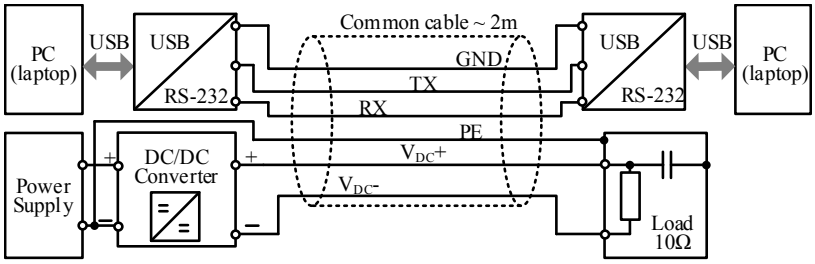


Figure 2.13: The schematic of measuring arrangement consisting of the DC/DC converter injecting the noise to the USB/RS-232 converter through common cables, adopted from [73].

rather than the switching frequency itself have been postulated. In order to test this assumption the experiment has been proposed, schematic of which is shown in Fig. 2.13. The experiment consisted of the 24 V power supply; DC/DC converter, supplying power to a resistive load and responsible for providing representative digital signals such as microprocessor-based control devices, for which DetM and RanM techniques were used; a 10 Ω resistive load with a simulated parasitic capacitance; and two laptops representing a transmitter and a receiver; and USB/RS232 converters, responsible for converting the USB signal into RS232 data protocol. The schematic from Fig. 2.13 also indicates the cabling arrangement used in the experiment. Fig. 2.14 presents the photo of the experimental setup, indicating as well the time-domain and frequency-domain measurement devices, represented by, respectively, oscilloscope and an EMI test receiver.

The time-domain measurements of the EMI current generated by the switching converter are depicted in Fig. 2.15 (a). Again, as with the previous experiments, the damped oscillation shape can be easily distinguished. Fig. 2.15 (b) shows the serial transmission signal, measured between RX and GND nodes (see Fig. 2.13 for reference), with superimposed interference. As already mentioned, in serial communication the value of the signal is established by measuring the voltage level at a particular time instant and comparing it with some predefined level. In the communication scheme ap-

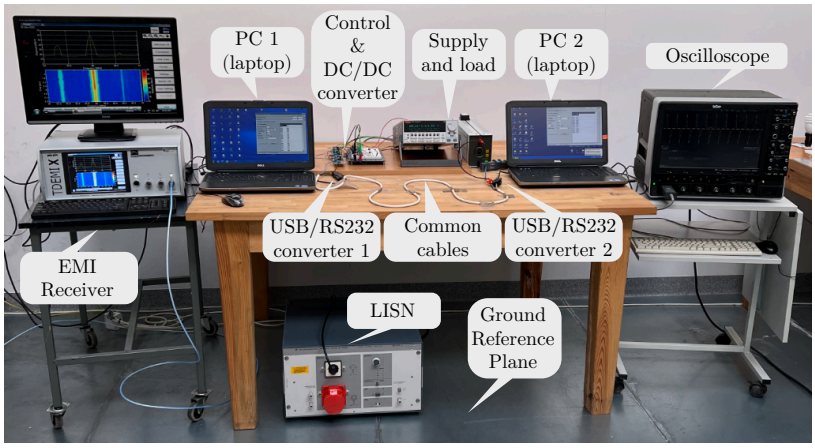


Figure 2.14: The laboratory photo of the measuring arrangement from Fig. 2.13, adopted from [73]

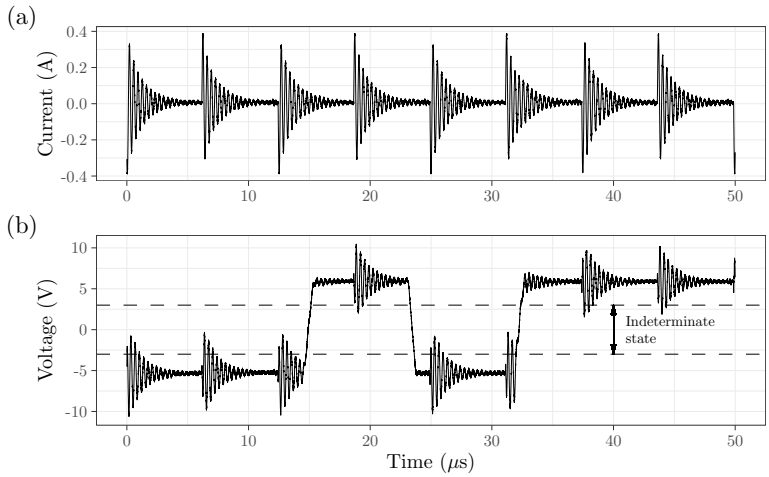


Figure 2.15: Waveforms taken in measuring arrangement: (a) EMI current generated by converter, (b) serial transmission signal with superimposed interference coupled from converter, adopted from [73].

plied in this experiment, voltage signals between -5 V and -3 V correspond to the binary '1', while signals between 3 V and 5 V represent the binary '0'. Therefore, if the measured signal is in the indeterminate zone, depicted in Fig. 2.15 (b), the value of the bit may be flipped or read incorrectly, which can bring about a rejection of the entire data frame and thus prevent the communication from being established or at least lower the communication capacity.

In the case of serial data transmission, EMC compliance testing should con-

centrate on achieving a reliable transmission. One possibility to quantify the transmission reliability is to measure the awaiting times for obtaining an error in the reading. This metric was applied in the discussed experiment. In order to test the influence of different switching frequencies, the nominal frequency was changed from 20 kHz to 25 kHz with step of 1 kHz. In the RanM algorithm, the variance of frequency change was set to 50%, and the frequency was modulated uniformly around the nominal frequency. The RS232/USB converter operated with data transmission rate equal to ∼58,409 Hz and received data frames consisting of 280 bits. For each switching frequency over 1,000 data frames were exchanged between PC1 and PC2. Table 2.1 collects the exact number of the data frames sent to the USB/RS232 converter.

Table 2.1: Parameters and results of the experiment depicted in Fig. 2.13 with transmission rate 58,409 Hz.

f_s (kHz)	Number of frames sent	Number of frames rejected	Probability of error	Mean error awaiting time (s)
DetM				
20	1,520	330	0.2171	0.5689
21	1,515	209	0.1380	0.8993
22	1,530	338	0.2209	0.5579
23	1,516	420	0.2770	0.4670
24	1,511	432	0.2859	0.4367
25	1,519	312	0.2054	0.7980
RanM				
20	1,513	300	0.1983	0.6538
21	1,528	327	0.2140	0.5942
22	1,515	337	0.2224	0.5814
23	1,525	347	0.2275	0.5502
24	1,521	378	0.2485	0.5181
25	1,517	396	0.2610	0.4684

The experiment showed many data frames are rejected by the receiver, due to an error in the reading. At a first glance, the mean error awaiting time does not seem to reveal any relationships neither with the switching fre-

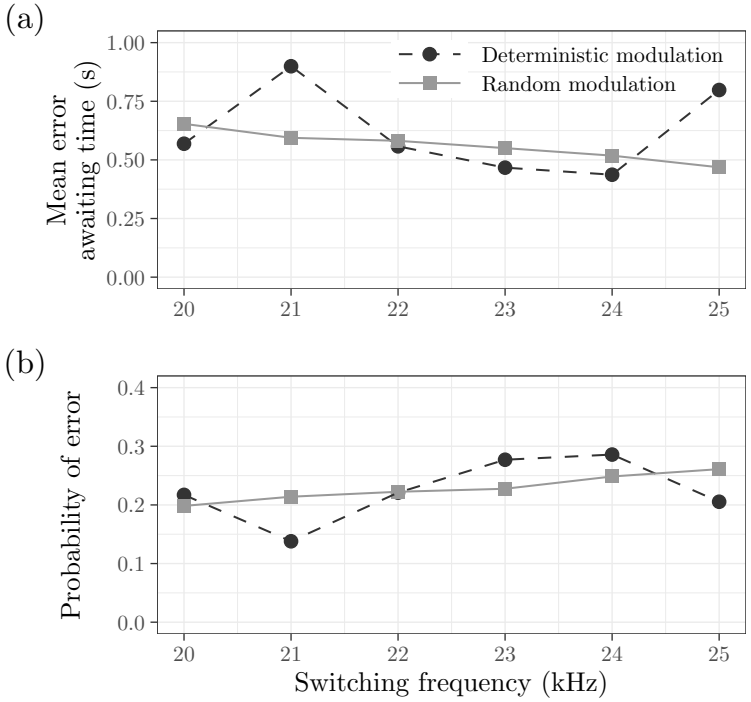


Figure 2.16: The results of the experiment from Fig. 2.13: (a) Mean awaiting times for the transmission error, (b) Probability of the transmission error. Adopted from [73].

quency, nor with the applied modulation. This is also depicted in Fig. 2.16 which visually presents the data from Table 2.1. In particular, one can see the mean error awaiting times as a function of frequency, separately for RanM and DetM depicted in Fig. 2.16 (a). Visible is an apparent decreasing relationship between the mean awaiting time and the switching frequency for RanM; however, the presented data does not allow to draw any meaningful conclusions as to the relationship between RanM and DetM. For example, for the switching frequencies of 21 and 25 kHz the mean awaiting time for an error is larger for DetM than for RanM, while for the frequencies 20, 22, 23 and 24 kHz the mean awaiting time is higher in RanM case compared to DetM.

Since the number of sent frames differs between the cases for each frequency, in Table 2.1, to normalize the results, the probability of error is

introduced, computed using the 'frequentist' probability definition as the number of rejected frames over the number of the total frames sent. This metric is also depicted in Fig. 2.16 (b). It can be immediately noticed that the higher the number of rejected frames, the lower the mean error awaiting time; the results seem to mirror each other. This can be intuitively understood by considering that in a fixed period of time, if the proportion of rejected frames is high, then this translates to shorter times of obtaining the next error. However, again, the collected data does not allow to draw any conclusions as to the advantage of using RanM over DetM.

2.2.2 Bernoulli trials for the series transmission

To gather further insights about the influence of the modulation techniques on the obtained probability of errors the experiment described in the previous section was repeated with an increased range of switching frequencies; the switching frequency was changed between 10 kHz and 34 kHz with a step of 1 kHz. As the previous results did not reveal any useful relationships it was decided to use a statistical significance test alongside. This enabled to focus on the results which were significantly different between the two modulation techniques. To this end, the experiment was modelled in the framework of a Bernoulli trial, which distinguishes between the 'success' and 'failure' events. In the presented case, the 'success' was observing an error in the reading, associated with the probability p; while the complementary 'failure' was not receiving the error, and therefore reached with probability $1 - p$. Further, for a fixed a switching frequency, p_d was denoted the probability of success in DetM case (thus, $1 - p_d$ the probability of failure) and p_r was the probability of success in RanM case (with $1 - p_r$ denoting the probability of failure). To verify for which frequencies the

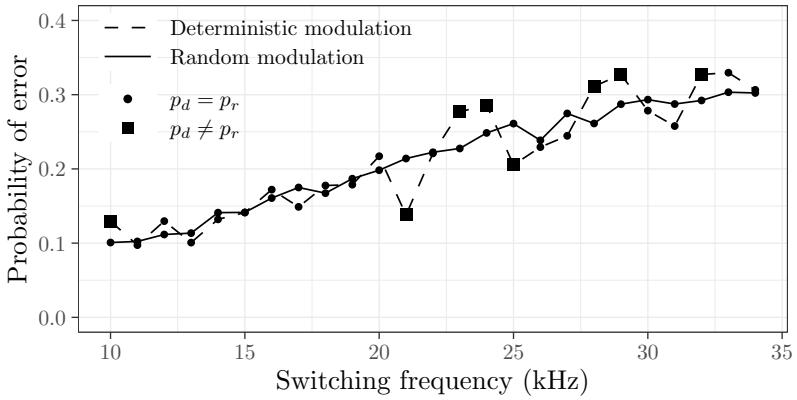


Figure 2.17: Probability of errors obtained from the experiment with DetM and RanM, adopted from [73].

probability of obtaining an error was significantly different between RanM and DetM, the proportions test [88] was employed. The null hypothesis H_0 stated that no significant difference can be observed between p_d and p_r, versus the alternative H_1 that the two probabilities are different. The results of the experiment are presented in Fig. 2.17, with probabilities p_d and p_r indicated, respectively, by a dashed and a solid line. The hypothesis H_0 was rejected at a significance level $\alpha = 0.05$ in favour of H_1 for switching frequencies 10, 21, 23, 24, 25, 28, 29, and 32 kHz, which is indicated in Fig. 2.17 by the black squares. For the rest of the switching frequencies the null hypothesis was accepted, and therefore no difference between the RanM and DetM was found.

2.3 Statistical Evaluation of Time-Domain measurements

The initial time-domain measurements of the voltage signals revealed that the only differences between RanM and DetM with respect to the interference were the moments in time at which this interference occurs. In order

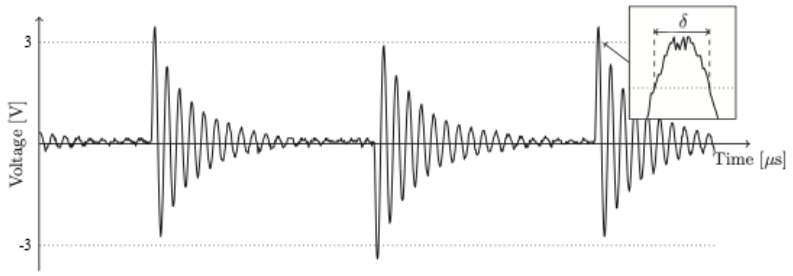


Figure 2.18: Experimental voltage waveform with the width of the interference depicted.

to understand how these signals influence the errors obtained in such systems, alongside the frequency domain analysis, a time-domain analysis is needed. Moreover, time-domain analysis that can support EMC tests was postulated by other researchers [89, 90]. Regarding the context of series communication, the time-domain analysis should focus on understanding under what circumstances the communication signal can exist within the interference zone, as shown in Fig. 2.15 (b). This information can be gathered from observing a single damped oscillation signal, such as the one presented in Fig. 2.18, which depicts the width of the interference, denoted δ. This width indicates the time for which the interference signal exceeds the threshold and creates a risk of interference with the communication channel. Parameter δ can be obtained from time-domain experiments or simulations, but is also linked to the dominant frequency of the oscillation and decay rate, and can be obtained through frequency domain data, as will be discussed in the following chapters.

Another important parameter in the time-domain analysis is the switching period (the reciprocal of the switching frequency), which indicates the time moments at which the damped oscillatory signals emerge. Moreover, in the presented scenario, the data transmission frequency (or the bit checking frequency) is also important, as it allows to understand the relation between the data transmission signals and the interference voltages. Time-domain

mathematical models which incorporate these three parameters were developed in [52], for RanM, and in [63] for DetM. However, due to their complexity an equivocal comparison between the two modulation schemes was not possible. In the remainder of this Chapter, work published in [73] is presented with additional information, in which for the first time:

1. The motivation for the statistical model is given,
2. Direct calculations of probability of errors in several special cases in the DetM model are provided,
3. It is shown that DetM model is very sensitive to changes in switching frequency and an explanation of this phenomenon is given,
4. The two models are compared, and the conclusion is drawn that on average RanM does not have any advantage over DetM with respect to mitigating the interference in series communication systems.

In the following subsections the models are recalled in the appropriate mathematical framework. It should be noted that the mathematical models were derived for simplified assumptions; in particular, they consider that the converter's driving signal is a square wave with 50% duty cycle ($\lambda = 0.5$). Therefore, the models do not explain intricate relationships between different modulation depths, signal shapes, electrical parameters of the circuits, or different communication protocols. Nevertheless, in the considered context, they prove to be useful; therefore, they will be extended to account for these parameters, as part of the future work.

2.3.1 The motivation for a statistical model

As seen in Fig. 2.15 and Fig. 2.18, each switching produces a damped oscillation interference pattern. Therefore, it should be easy to predict the value of this interference at any given point in time. Indeed, when the considered system employs DetM, assuming that the single interference pattern can be modelled using Eq. (2.2) and that the converter operates in a steady-state mode, one can express the voltage $V(t)$ at a given time t as [75]

$$V(t) = \sum_{k=0}^{\infty} \left(v(t - t_{k,\text{ON}}) - v(t - t_{k,\text{OFF}}) \right), \tag{2.4}$$

where $t_{k,\text{ON}}$ and $t_{k,\text{OFF}}$ are moments in time when the converter produces the k-th switch-ON and switch-OFF event, respectively. Let us denote by $\Delta S_0 = 1/f_s$ the nominal switching period of the converter. Then, moments $t_{k,\text{ON}}$ and $t_{k,\text{OFF}}$ can be expressed conveniently as [75]

$$\begin{aligned} t_{k,\text{ON}} &= \left\lfloor \frac{t}{\Delta S_0} \right\rfloor \Delta S_0, \\ t_{k,\text{OFF}} &= \left\lfloor \frac{t}{\Delta S_0} - \lambda \right\rfloor \Delta S_0 + \lambda \Delta S_0, \end{aligned} \tag{2.5}$$

where $\lfloor \cdot \rfloor$ represents the floor function. However, if the converter is operated with a RanM technique, such deterministic prediction is not possible. To understand this limitation, suppose for simplicity that in the steady-state the duty cycle $\lambda = 0.5$ is fixed. In the case presented above, after every $\lambda \Delta S_0$ the new interference pattern emerges; therefore, after n switching actions, the value of $V(t)$ will be approximately the same as after $n-1, n-2$ etc. This question can be now asked about the value of $V(t)$ after n switching actions for RanM. To answer it, one can look at RanM from a mathematical perspective and consider the sequence of successive switching periods $\Delta S_1, \ldots, \Delta S_n$ as a sequence of random variables. Suppose

that $\Delta S_1, \ldots, \Delta S_n$ are random variables drawn from uniform distribution, where for each $i = 1, \ldots, n$, one has $\Delta S_i \sim \mathcal{U}((1-\kappa)\Delta S_0, (1+\kappa)\Delta S_0)$, for some $\kappa \in (0, 1)$. Further, one can consider the sum $S_n = \Delta S_1 + \ldots + \Delta S_n$, and notice that S_n is a random variable. Indeed, let us rewrite S_n as

$$S_n = (1-\kappa)\Delta S_0 + 2\kappa\Delta S_0 \sum_{i=1}^{n} X_i, \tag{2.6}$$

where $X_i \sim \mathcal{U}(0, 1)$ for each $i = 1, \ldots, n$. The sum $Y_n = \sum_{i=1}^{n} X_i$ is a random variable of Irwin-Hall distribution [91]. By central limit theorem, for sufficiently large n (or sufficiently long observation time), Y_n approximately follows Normal distribution with mean $n/2$ and variance $n/12$. From this and from Eq. (2.6) one has

$$S_n \sim \mathcal{N}\left((1-(1-n)\kappa)\,\Delta S_0, \frac{1}{6}n\kappa\Delta S_0\right). \tag{2.7}$$

This line of reasoning shows that it is not possible to predict the value of interference at a given point in time in a system which employs RanM. Thus, in order to predict the probability of interference a statistical approach is needed. Such an approach, however without presenting the above motivation, lead to the development of the model originally published in [52], which will be now briefly recalled.

2.3.2 Probability of error in systems with Random Modulation

Let us repeat the notation used previously. We have

- ΔS_0 is the nominal switching period,
- $\kappa \in (0, 1)$ is a (fixed) spreading factor,

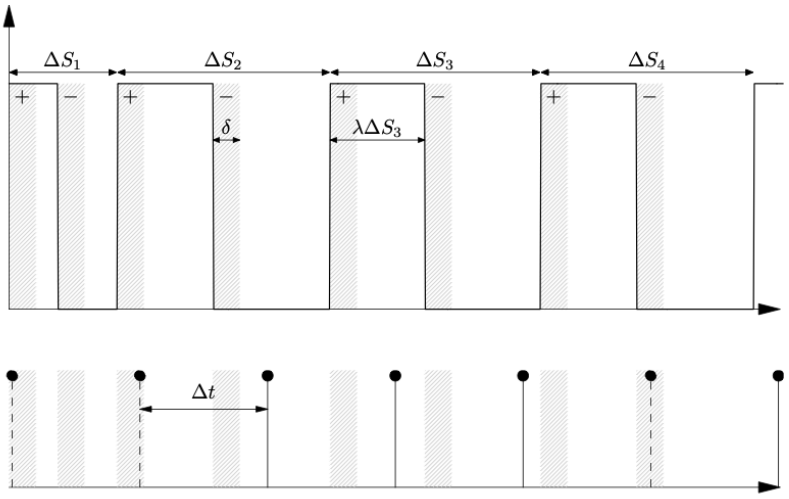


Figure 2.19: A visual interpretation of the random modulation scheme used in developing RanM mathematical model, from [73].

- $\Delta S_1, \Delta S_2, \ldots$ is a sequence of random variables, where $\Delta S_i \sim \mathcal{U}((1-\kappa)\Delta S_0, (1+\kappa)\Delta S_0)$ for each $i \geq 1$,
- Δt is the time difference between successive bit checking moments,
- $\lambda \in (0, 1)$ is the PWM duty cycle,
- δ is the time period for which the damped oscillation signal exceeds threshold, leading to the signal being in the indeterminate zone.

The above parameters are depicted in Fig. 2.19, where the simplified PWM operation with RanM is shown. The width of the interference δ is shown with a grey stripe, with '+' and '−' signs indicating the interference signal being, respectively, above the 2 V and below the -2 V thresholds. When the bit with value 0 overlaps with the '+' signal, the value of the bit is flipped and an error may occur in the reading; similarly, when the bit with value 1 overlaps with '−' zone, the bit value is corrupted and an error occurs. *What is therefore the probability of a single bit being flipped?* Let us denote by q the probability of occurrence of the bit 1 (thus, by $1 - q$ the probability of occurrence of the bit 0) and by p the probability of the

emergence of interference zone '+' (therefore, $1 - p$ being the probability of the emergence of interference zone '−'). It is clear that the two events are independent, therefore their join probability can be written as

$$p_c = q + p - 2pq. \tag{2.8}$$

The value of p_c expresses the probability that a single bit can be corrupted. If bits 0 and 1 occur with the same probability, i.e., $q = 1/2$ then the probability of a single bit corruption reduces to $p_c = 1/2$. This is also the assumption made for the remainder of this analysis.

Even though many data protocols implement safe modes enabling signals being transmitted successfully even if several bits are corrupted, in the simplest arrangement, used in the experiment presented above, the whole data frame is rejected if at least one bit in the data frame is flipped. Therefore, the probability of a data frame rejection should be considered, where it can be assumed that the data frame consists of n bits (in the earlier example $n = 280$). Let $X \in \{1, \ldots, n\}$ be a discrete random variable which indicates the number of bits appearing in any of the indeterminate zones of length δ. The probability of rejecting an entire frame can therefore be written as

$$P_{\text{error}} = \sum_{k=1}^{n} \left(1 - (1 - p_c)^k\right) P(X = k), \tag{2.9}$$

where $P(X = k)$ expresses the probability that k bits in the n-bit frame will appear in the indeterminate signal zone, while the term $1 - (1 - p_c)^k$ represents the total probability with which at least one bit out of k will be corrupted. Further, let $n_0 = \lfloor n\Delta t/\Delta S_0 \rfloor$. It has been shown, that for sufficiently large n and $\kappa > 0.25$, the probability of the appearance of k-th

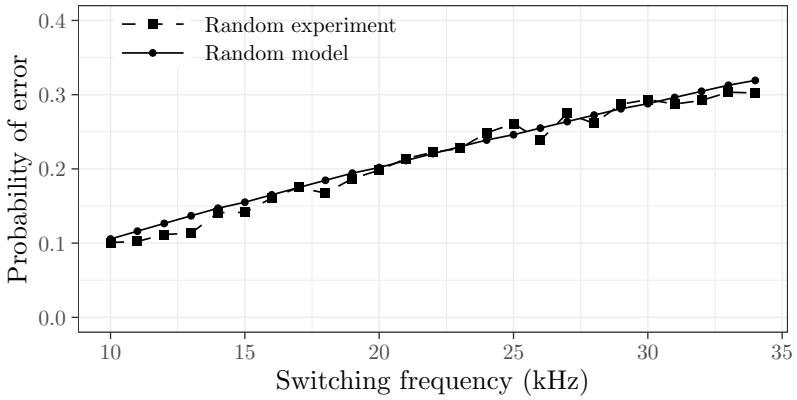


Figure 2.20: The predictions of RanM mathematical model vs. the experimental results in the RanM case, from [73].

bit in the distorted signal zone may be approximated by

$$P(X=k)=\begin{cases}\binom{n_0}{k}\left(\frac{2\delta}{\Delta t}\right)^k\left(1-\frac{2\delta}{\Delta t}\right)^{n_0-k} & \text{for } k=1,\ldots,n_0,\\ 0 & \text{for } k>n_0.\end{cases} \tag{2.10}$$

From Eq. (2.9) and Eq. (2.10) after simple manipulations, one can derive the expression for the probability of data frame rejection P_{error} as

$$P_{\text{error}}\approx 1-\left(1-\frac{\delta}{\Delta t}\right)^{\left\lfloor n\frac{\Delta t}{\Delta S_0}\right\rfloor}. \tag{2.11}$$

The implementation of Eq. (2.11) for the experimental data results in the predictions presented in Fig. 2.20; dashed line and black squares indicate the experimental data, and solid line and points indicate random model. It can be noticed that the model performs well, however small deviations between the model and experiment are likely a result of few repetitions of the experiment.

2.3.3 Probability of error in systems with Deterministic Modulation

This subsection gives an overview of the deterministic originally developed in [63], and provides a deeper insight into the predictions of the model by providing calculations of the probability of error in few special cases. The main rationale behind the model developed for DetM was that it should capture the highly complex relationship between the switching frequency and the bit checking frequency. To this end, one can switch from the domain of the real numbers to the integers and consider the problem of overlap between the data checking moments and switching moments in terms of number-theoretic relations between integers. To this end, let us first express any point in time in terms of integer numbers. Based on the simple observation that every digital device used for time-domain measurements has a certain time step with which the data is collected, and assuming that this time step is fixed and denoted by τ, one can express a time instant t as

$$t = T\tau, \quad \text{for } T = 0, 1, \ldots \tag{2.12}$$

Further, the three parameters described in the RanM model, i.e., the switching period ΔS_0, bit checking period Δt and the width of the interference δ can be expressed in terms on integers, by putting $M, N, D \in \mathbf{Z}$ such that

- $\Delta S_0 = M\tau$ is the nominal switching period,
- $\Delta t = N\tau$ is the time between bit checking moments,
- $\delta = D\tau$ is time that the signal may occur in the distorted zone.

Next, let Mi be the moment in time of the i-th converter's switching-ON

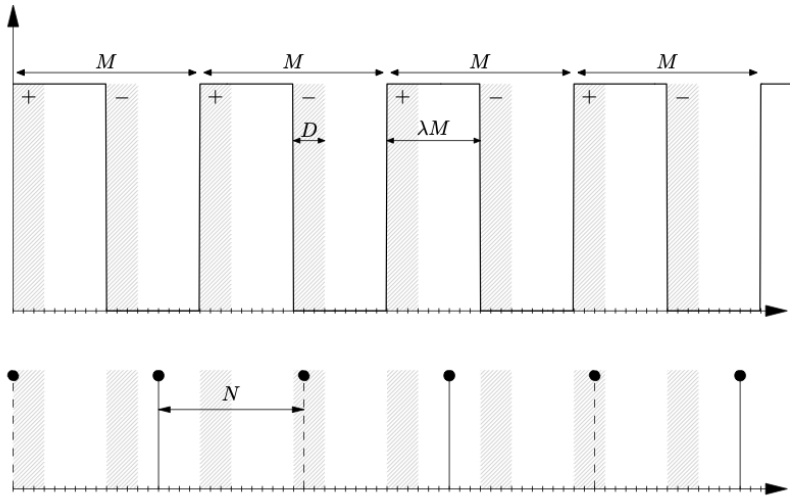


Figure 2.21: A visual interpretation of the deterministic modulation scheme used in developing DetM mathematical model, from [73].

action, for $i = 0, 1, \ldots$; and let Nj denote the j-th bit checking moment for $j = 0, \ldots, n-1$. Moreover, let $t = 1 - M, 2 - M, \ldots, 0$ be the initial time moment when the converter starts switching, assuming that there is no settling period and let $d = 0, \ldots, D-1$ denote the d-th moment of the interference within the (single) indeterminate signal zone of length D. Finally, let λ be the duty cycle of the PWM, such that λM is an integer.

The depiction of the mathematical model, which presents a simplified PWM modulated by DetM technique, which includes the discussed parameters is shown in Fig. 2.21. To gain some basic understanding it could be useful to play around with the parameters of the model, using an online tool developed by the author of this thesis[1].

Further, in order to predict the probability of error occurrence one can ask a question as to the prediction of moments at which the bit emerges in the interference zone. As it has been shown in [63] for such a meeting to occur

[1] https://karylsienn.shinyapps.io/Diophantine_model/ [online]. Accessed: 6.05.2023.

the following Diophantine equation must hold

$$Nj - M\left(\lambda(i \bmod 2) + \lfloor i/2 \rfloor\right) - t - d = 0, \tag{2.13}$$

for $j = 0, 1, \ldots, n-1$, $d = 0, 1, \ldots, D-1$ and $t = 1-M, 2-M, \ldots, 0$. Let $L(t_0)$ denote the number of quadruples (i, j, d, t) which satisfy Eq. (2.13) for $t = t_0$. Under the assumption that bit values 0 or 1 appear with the same probability 1/2 and from the theorem of total probability, the probability of frame rejection in the deterministic case can be estimated from the following equation

$$P_{\text{error}} = 1 - \frac{1}{M} \sum_{t_0=1-M}^{0} \left(\frac{1}{2}\right)^{L(t_0)}. \tag{2.14}$$

Note, that there is no general formula for $L(t_0)$ and its evaluation is based on numerical simulations. However, it can be derived for several special cases along with the probability of error; these are provided below.

N is a multiple of M

Let us assume that for some $m \in \mathbf{Z}$, we have $N = mM$. In such case for $t_0 = 1 - M + d$ and $t_0 = 1 - (1-\lambda)M + d$, where $d = 0, 1 \ldots, D-1$, all n bits will be present in the indeterminate zone. Thus, one can express the probability of error as below

$$\begin{aligned} P_{\text{error}} &= 1 - \frac{1}{M}\left(2D\left(\frac{1}{2}\right)^n + (M - 2D)\right) \\ &= \frac{D}{M}\left(2 - \frac{1}{2^{n-1}}\right). \end{aligned} \tag{2.15}$$

Note that for a fixed frame length n and interference width δ and the above provides a model linearly dependent on the switching frequency.

M is a multiple of N

Similarly, let $M = mN$ for some even integer m. If such t_0 is found for which the first bit meets the indeterminate zone, one can easily see that the successive $2n/m$ bits also meet the indeterminate zone; and this occurs for mD different positions of t_0. For the remaining $M - mD$ positions $L(t_0) = 0$. Thus, one has

$$\begin{aligned} P_{\text{error}} &= 1 - \frac{1}{M}\left(mD\left(\frac{1}{2}\right)^{2n/m} + (M - mD)\right) \\ &= \frac{D}{N}\left(1 - \frac{1}{4^{n/m}}\right). \end{aligned} \tag{2.16}$$

N and M are co-prime

Two numbers N and M are co-prime if their Greatest Common Divisor (GCD) is 1; then, their Lower Common Multiple (LCM) is simply the product NM. In such a case, if the first bit and first switching instant occur at the same time, $(M+1)$-st bit and N-th switching instant will also occur at the same time. Between these two instants, D bits will be present in the interference zone, thus $L(t_0) = D$. With an additional assumption that the number of bits in the frame n is a multiple of M, i.e. $n = kM$ for some $k \in \mathbf{Z}$, the probability of frame rejection can be expressed as

$$\begin{aligned} P_{\text{error}} &= 1 - \frac{1}{M}\sum_{t_0=1-M}^{0}\left(\frac{1}{2}\right)^{\frac{D}{M}n} \\ &= 1 - \left(\frac{1}{2}\right)^{\frac{D}{M}n}. \end{aligned} \tag{2.17}$$

Fig. 2.22 presents the predictions of the DetM model along with the experimental probabilities. The DetM model is represented by squares connected by a dashed line, and the DetM experimental probabilities are shown by

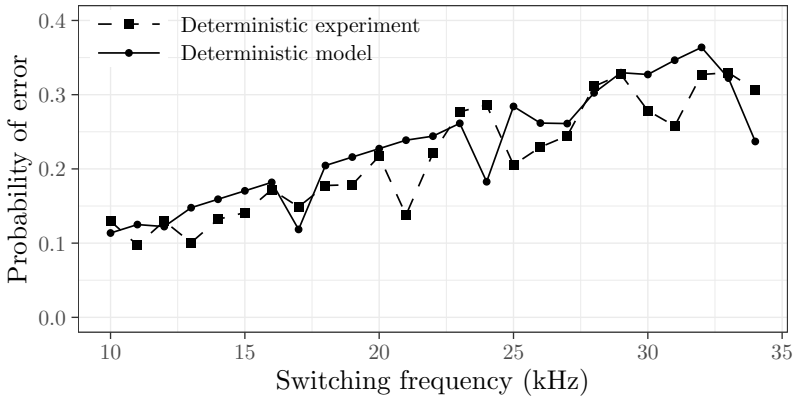


Figure 2.22: Predictions of the DetM mathematical model vs. results of the experimental investigation for DetM case, from [73].

black circles connected by solid line. What can be seen from the plot is that, although the trend seems to match between the experiment and the model, for many switching frequencies the results differ between the two. As an example for the frequency of 20 kHz the probability of error are almost the same, however for the corresponding 21 kHz the probability of error obtained from the experiment is much larger than the one obtained from the model. This issue has not been recognized nor answered in the original paper [63], and will be discussed below.

2.4 Comparison of RanM and DetM

In Section 2.2.2 it has been identified that for the frequencies 10, 21, 23, 24, 25, 28, 29, and 32 kHz the probabilities of errors obtained from the experiment were significantly different between the RanM and DetM, while for the remaining frequencies no significant differences were found. Therefore, for the clarity of results the comparison between RanM and DetM will be presented only for those selected frequencies; for the rest of the frequencies it can be concluded that no significant difference between RanM and

DetM can be found. As it has been presented in the section, for the deterministic model there exists a certain mismatch between the model and the experimental data. Therefore, as a first step towards the comparison of the two models, it was verified for which frequencies do the models match the experimental data.

To this end, the exact binomial test was conducted. Let us denote by p_{m} the probability of a frame rejection predicted by the model for a fixed switching frequency f_s, and by p_{e} the probability of the frame rejection as obtained from the experiment. The following hypothesis was stated at significance level $\alpha = 0.05$

$$H_0 : p_{\mathrm{m}} = p_{\mathrm{e}} \quad \text{vs.} \quad H_1 : p_{\mathrm{m}} \neq p_{\mathrm{e}}. \tag{2.18}$$

The results of the test are shown in Table 2.2. For the cases where p-value > 0.05 the null hypothesis H_0 has been accepted; this is the case for all predictions of the RanM model. Nevertheless, in the DetM case the null hypothesis should be rejected for the frequencies 10, 21, 24 and 32 kHz. In particular, small p-value for 21 and 24 kHz (p-value $< 10^{-6}$) indicates that a particular attention should be placed in explaining the poor predictions of the model at these two frequencies.

2.4.1 Sensitivity of DetM model

The DetM model is highly dependent on the chosen time step τ, which can affect the other parameters. However, after sufficiently small τ has been chosen ($\tau = 1\,\mathrm{ns}$), there still exists a complex relationship between the integers M, N, and D. That is, a small change in one parameter will result in substantial change in the predictions of the DetM model. In

Table 2.2: Results of exact binomial test for the investigated frequencies

f_s (kHz)	Experiment (p_e)	Prediction (p_m)	95% CI	p-value
DetM				
10	0.1295	0.1120	(0.116, 0.145)	0.0339
21	0.1380	0.2352	(0.124, 0.153)	$< 10^{-6}$
23	0.2770	0.2576	(0.258, 0.297)	0.0885
24	0.2859	0.2228	(0.267, 0.306)	$< 10^{-6}$
25	0.2054	0.1950	(0.188, 0.223)	0.3154
28	0.3112	0.3136	(0.292, 0.331)	0.8683
29	0.3272	0.3248	(0.307, 0.348)	0.8482
32	0.3272	0.3584	(0.307, 0.348)	0.0111
RanM				
10	0.1009	0.1056	(0.088, 0.114)	0.5870
21	0.2140	0.2113	(0.197, 0.232)	0.8021
23	0.2275	0.2298	(0.21, 0.246)	0.8551
24	0.2485	0.2389	(0.23, 0.267)	0.3832
25	0.2610	0.2461	(0.243, 0.28)	0.1798
28	0.2612	0.2725	(0.243, 0.28)	0.3412
29	0.2872	0.2810	(0.268, 0.307)	0.5885
32	0.2922	0.3046	(0.273, 0.312)	0.3020

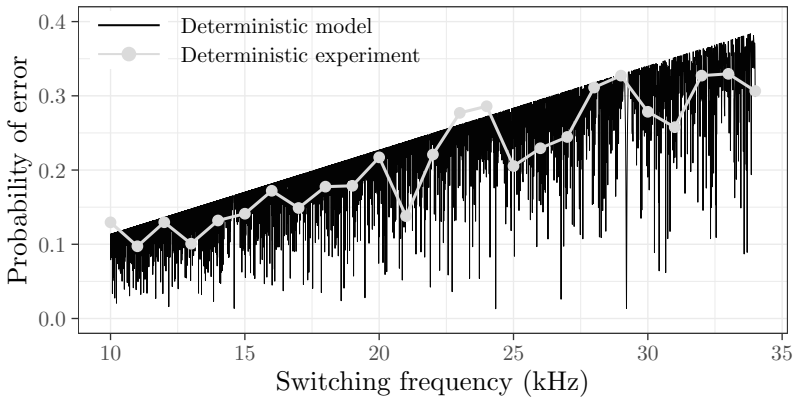


Figure 2.23: Predictions of the deterministic model, simulated with a small frequency step, from [73].

Fig. 2.23 such a situation has been depicted. The plot presents the DetM model simulated for a small frequency step, with the original experimental data overlaid represented by a gery line connected with dots. One can see that the probability of errors is unstable and even a small change in the switching frequency leads to a large change in the predicted probability of error.

In order to understand this sensitivity to small changes in parameters, let us consider two idealized and simple cases, one with $M = 8$ and the second one with $M = 9$, where for both cases $D = 3$, $N = 4$ and $n = 6$. Now, let us consider the number of distorted bits $L(t_0)$ for each position of $t_0 = 1 - M, \ldots, 0$ derived by solving the Diophantine equation (2.13). The results are juxtaposed in Table 2.3, which additionally indicates the final probability of error P_{error}. It can be seen that even for a small change in M the distribution of distorted bits among the different positions of t_0 is completely different, i.e. in the first case, when $M = 8$, we have only two positions when no bits are interfered and 6 positions with 3 interfered bits, while in the second case, for $M = 9$, at least 1 bit is interfered for all positions. Hence, the resulting probability of error varies significantly between the two cases.

Table 2.3: The number of disrupted bits $L(t_0)$ and probability of error P_{error} for $M = 8$ and $M = 9$, with $D = 3$, $N = 4$ and $n = 6$.

$M = 8$

t_0	-7	-6	-5	-4	-3	-2	-1	0	P_{error}
$L(t_0)$	0	3	3	3	0	3	3	3	0.65625

$M = 9$

t_0	-8	-7	-6	-5	-4	-3	-2	-1	0	P_{error}
$L(t_0)$	2	3	2	1	1	2	3	2	2	0.7222

Now, let us consider a case with the integer parameters corresponding to the experiment, i.e. when $N = 17,120$, $D = 41$ and $n = 280$. Furthermore, let us focus on two switching frequencies 29109 Hz and 29208 Hz, depicted in Fig. 2.23, for which the corresponding values of M are, respectively, $M = 17,177$ and $M = 17,119$. For $M = 17,177$ only 1 bit is interfered at 11480 different positions t_0, while for the remaining 5697 positions no bits are interfered. However, for $M = 17,119$ the number of interfered bits between 1 and 40 occurs for exactly two positions in each case, and there are

240 positions where 41 bits are interfered. This also means that for 16799 different t_0 no bits are interfered. The resulting probabilities of error are respectively, $P_{\text{error}} \approx 0.3342$ and $P_{\text{error}} \approx 0.0186$, i.e. significantly different. It is therefore clear that the sensitivity of the DetM model is a result of the relationships between the integer numbers, and that even small changes in one the parameters results in different predictions. Similarly, one can understand that the differences in the probability of error in the experiments with deterministic modulation are due to the relationships between the switching frequency, data transmission frequency and the length of the indeterminate zone.

2.4.2 Brute-force selection of neighbouring frequencies

After a simple explanation of the sensitivity of the DetM model, we can come back to the results of the exact binomial test presented in Table 2.2. Considering the above explanation, it can be hypothesized that in the cases, for which the p-value was smaller than the significance level α, the actual switching frequency in the experiment was different from the nominal. Indeed, it can be shown that by picking a neighbouring frequency the predictions of the error correspond at a significance level $\alpha = 0.05$ to the experimental probabilities. Table 2.4 presents results of a brute-force analysis with the frequencies 21 and 24 kHz, for which the p-value presented in Table 2.2 test was the smallest. To perform this analysis, the following algorithm was applied:

1. for a chosen τ and switching frequency f_s calculate the integer M,
2. for the specific M compute the error probability using Eq. (2.10),

3. apply the exact binomial test for the newly predicted probability and experimental probability,

4. if the computed p-value is less than a significance level α, go to the last step,

5. increase (decrease) M and repeat previous steps,

6. calculate new switching frequency f_s from M and compute the prediction of the RanM model for that switching frequency.

Table 2.4: Exact Binomial test for frequencies higher and lower than 21 kHz and 24 kHz for which p-value $< 10^{-6}$ in the deterministic case.

f_s (Hz)	Experiment	Prediction	95% CI	p-value
DetM				
21000	0.1380	0.2352	(0.121, 0.156)	$< 10^{-6}$
20913		0.1297		0.3390
21014		0.1456		0.4229
24000	0.2859	0.2228	(0.263, 0.309)	$< 10^{-6}$
23993		0.2687		0.1314
24003		0.2688		0.1389
RanM				
21000	0.2140	0.2113	(0.194, 0.235)	0.8021
20913		0.2113		0.8021
21014		0.2113		0.8021
24000	0.2485	0.2389	(0.227, 0.271)	0.3832
23993		0.2389		0.3832
24003		0.2389		0.3832

This simple analysis presents the possibility of finding frequencies both below and above the nominal switching frequency for which predictions of the model are close to the experimental probabilities. Indeed, instead of 21 kHz, the switching frequency might have been 20,913 Hz or 21,014 Hz and instead of 24 kHz the actual switching frequency might have been 23,993 Hz or 24,003 Hz. As it can be seen the differences do not exceed 100 Hz. Moreover, the predictions of the RanM model do not differ up to 4 digits from the ones obtained with stated switching frequencies 21 kHz and 24 kHz,

due to the smoothness of the model, which confirms that the choice of the 'new' switching frequencies is viable. It can therefore be concluded that the actual switching frequency might have been different from the assumed one either because of not sufficient precision of the measurement or the tolerances associated with the switching devices. Thus, the application of the DetM model should incorporate some uncertainty bounds that indicate how the nominal switching frequency may change.

2.4.3 Averaging DetM and RanM

Furthermore, previous observations indicate that comparison between DetM and RanM cannot be carried out by looking at predictions of the error on a point-by-point basis. Fig. 2.24 a) presents a visual comparison between the models for a wider frequency range 10 kHz – 1 MHz with fixed parameters

- $\Delta t \approx 17.12\,\mu$s,
- $\delta \approx 40.6\,$ns,
- $\tau = 1\,$ns,

which correspond to the ones obtained in the experiment. As it has been presented, the complexity of the DetM does not allow for a simple comparison. When looking at Fig. 2.24 a) one can see that the trend in the DetM case seem to indicate a worse performance of the DetM model over RanM. However, this is only apparent, as the 'worst-case' trend in fact corresponds to one of the special cases described in Section 2.3.3, i.e., when N and M are co-prime numbers.

Therefore, to compare the two models one needs to average the results. An intuitive average scheme for any frequency-related changes is to group the

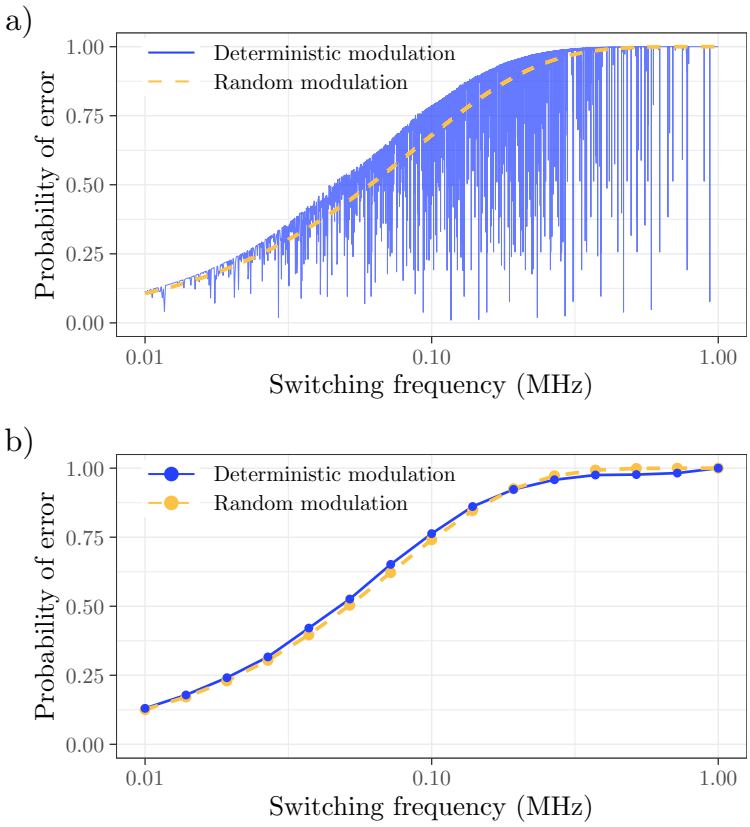


Figure 2.24: The probability of error predictions of the RanM and DetM models for the switching frequency range 0.01 MHz and 1 MHz; a) a direct evaluation of the mathematical models, b) the average trend of the error probability predictions using the mathematical models. Adopted from [73].

results by logarithmic differences between the frequencies and average the results in a bin. This average has been applied for the predictions of the two models and the results are depicted in Fig. 2.24 b). As expected, the results indicate that on average there is no significant difference between RanM and DetM in the investigated switching frequency range, in the context of influence of generated EMI on the reliability of serial transmission.

2.5 Conclusion

This chapter presented the first known approach to compare influence of EMI generated by converters with RanM and DetM on the probability of error appearance in single-ended serial transmission, as presented in the already published works by the author of this thesis, Niewiadomski *et al.*, in [75] and [73].

The presented literature review indicated that although problems with utilizing RanM techniques are known, and approaches to understand their usefulness and limitations have been proposed [26, 62], many researchers still revert to utilizing the RanM-based modulation techniques to help mitigate EMI. The inspiration for the analysis presented in this chapter were *in situ* EMC observations, described in greater detail in the Introduction, of CAN communication being disturbed by EMI. In regard to the EMC work, applying RanM technique did not bring about satisfactory EMC compliance, whereas changing the parameters of DetM in the same arrangement brought a significant reduction EMI-induced error. In this chapter, this phenomenon has been investigated and the two modulations techniques were explored, in terms of their influence on the probability of error, both in an experimental setting, and later, based on two mathematical models and statistical significance tests.

The complexity of the mathematical model for DetM prevented an equivocal comparison between the modulation techniques, however the proposed averaging scheme, which used logarithmic distances between the frequencies mitigated that limitation. As a result a conclusion was drawn confirming that in spite of the lower levels of EMI measured in a standardized manner, RanM on average does not have advantage over DetM in the context of EMI influence on the serial transmission reliability. Even though such a

result has been intuitively understood by researchers, in this chapter, the first mathematical confirmation of it has been provided. As such, this result might be useful for system integrator, PE engineers or EMC engineers who want to use RanM in their system designs.

Moreover, this chapter further develops the mathematical model for DetM by providing direct calculations of the predictions of the model in several special cases. Additionally, the limitations of the model and the way to overcome these are discussed.

The results presented in this chapter are subject to various improvements, which have either been already tackled or will be taken forward in a frame of future work. Some of them are listed below. The developed models have been derived for simple assumptions. Further work is therefore needed to extend these models to take into account more realistic and complex assumptions, e.g. different or varying modulation depths. The analysis, results of which were presented in Table 2.4, used a simplistic brute-force algorithm; this algorithm could be optimized and applied to real-time systems. Moreover, comparison of DetM model presented here with other works should be performed, most notably with the framework proposed by Li *et al.* in [92], where the authors applied χ^2 tests for inferring errors in serial communication systems disturbed by repetitive (deterministic) EMI disturbances was discussed. The DetM model reveals that in order to use it the uncertainty bounds should be applied for the switching frequency. Since this is highly related to an uncertain behaviour of circuit components, tolerances, presence of parasitics and environmental conditions, an efficient way of proposing such uncertainty bounds should be discussed. Finally, a direct link between the PE circuit and the predictions of the model could be given. The last two enhancements will be discussed and partially presented in the next chapters.

Chapter 3

Surrogate modelling of EMI circuits

3.1 Motivation

Previous chapter showed that RanM technique is not a valid EMC-assuring technique in the context when PE converters operate close to serial data transmission circuit. This result was obtained from the experimental data and the comparison of two mathematical models, developed with an assumption that the EMI signal is a damped oscillation which occurs after every switching instant. In this and next chapters, a link will be provided between the predictions of the RanM and DetM models and the electrical parameters of the PE circuits. This will be done through stochastic simulation techniques, such as Support Vector Machine and Polynomial Chaos, and verified using Monte Carlo simulations. It will also be assessed which parameters influence the most the Quantity of Interest (QoI), which in this case will be the parameters of the damped oscillation signal f, v_0 and λ, as well as the parameter δ, i.e. the time during which the damped oscilla-

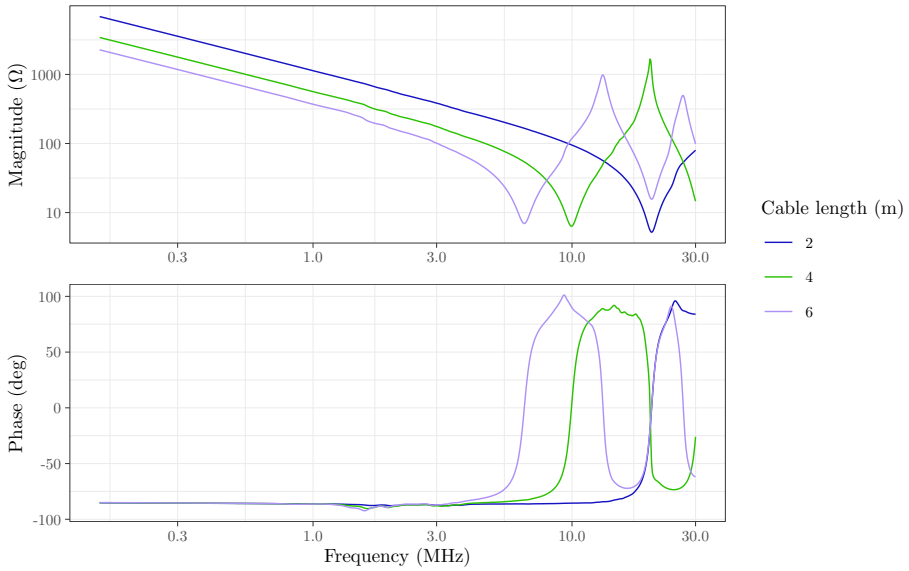


Figure 3.1: Impedance measurement of two cables.

tion signal is above the predefined threshold. This assessment will be done through the usage of sensitivity indices, known as Sobol' indices.

Before referring the methods used in the remainder of this thesis, let us give a brief motivation for the work presented hereafter. The EMI currents that propagate between the PE devices and communication circuits are introduced by the means of capacitive or inductive couplings, as well as by the means of common impedance. When analysing the circuits, such interactions are often modelled in terms of lumped-parameter elements such as capacitors, resistors, and inductors. However, because of spatial geometries as well as environmental conditions it is often unclear what the actual impact of these parasitics on the EMI currents and voltages is. As an example, Fig. 3.1 shows the measured impedance between two insulated wires for 3 different cables, of lengths, respectively, 2 m, 4 m and 6 m using an impedance analyser. The two wires were kept close to each other, at a distance of around 1 mm and left with open terminations; a situation which can happen if a cable wears out and breaks at some point. It can be noticed how the magnitude and phase of the impedance reacts to the

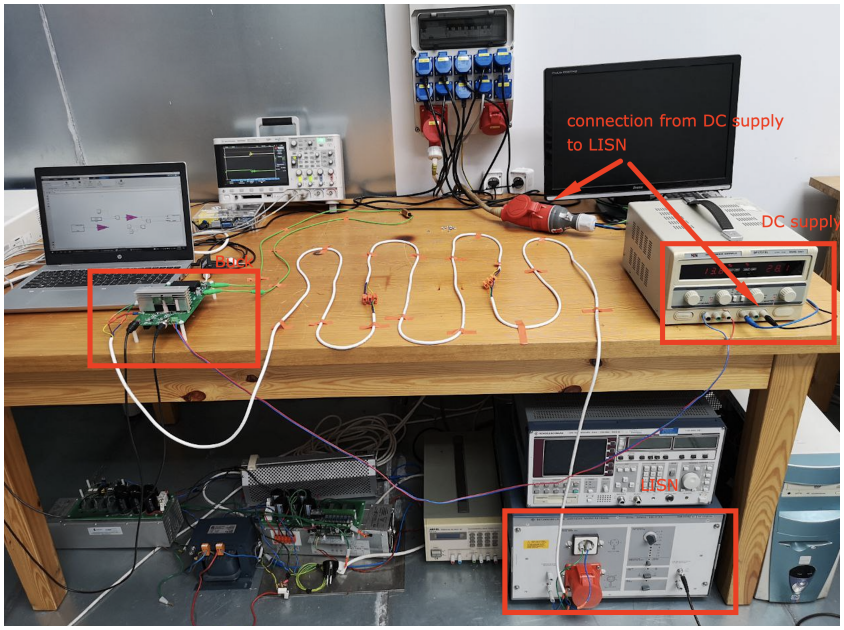


Figure 3.2: The experimental setup.

length of the cable, changing properties from inductive to capacitive and vice versa. The resonances that occur at the spectrum above 3 MHz will allow the coupling of currents and voltages.

The measured cables have been used in the experimental setup as a connection between Line Impedance Stabilization Network (LISN) and a DC/DC buck converter Wolfspeed Cree KIT-CRD-3DD065P Buck-Boost evaluation kit, shown in Fig. 3.2. Results of the experiment are presented in Fig. 3.3 which shows the Line-to-Line and Line-to-Neutral spectra obtained from an EMI Spectrum Analyser. Apart from the characteristic harmonics at the low frequency, reflecting the switching operations of the converters, one can also notice the upward trend above 1 MHz, and in particular the peaks and valleys that depend on the cable lengths, and correspond to the variable changes in impedance presented in Fig. 3.1.

As another example, consider Fig 3.4 which presents the capacitance and equivalent series resistance measurements of five identical RIFA capacitors, made with an impedance analyser. According to the data sheet, the nomi-

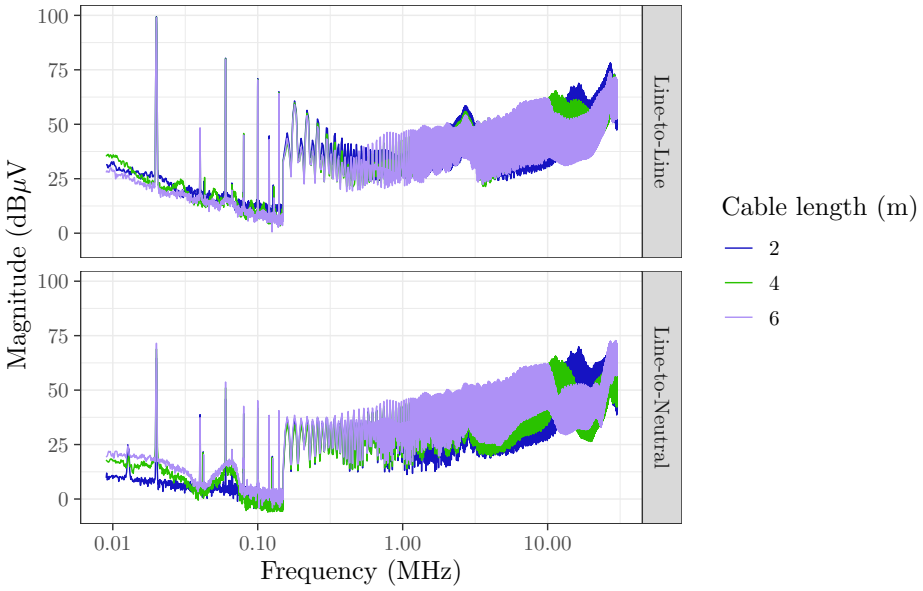


Figure 3.3: Line-to-Line and Line-to-Neutral measurements.

nal capacitance of the capacitors is 470 pF with 20% tolerance. As it can be seen from the impedance curves, the real capacitance is below 470 pF and increases in value above 10 MHz; small differences in the value of both the frequency-dependent capacitance and the frequency-dependent resistance can also be seen between the different capacitors.

The capacitors have been used in another experimental setup, presented in Fig. 3.5 with the same DC/DC buck converter, and placed between the switching circuit and the ground plane, to simulate parasitic capacitance between the converter, and it's grounded enclosure.

As a result Fig. 3.6 presents common mode current and output voltage, obtained with capacitors 1, 2, 3 used singularly, and capacitors 4 and 5 connected in parallel theoretically doubling the capacitance. It can be seen that the usage of single but different capacitors has a small impact on the overall shape of the damped oscillation, however still visibly affecting the damping, while doubling the value of the capacitance increases the common mode current amplitude. No obvious difference on the output voltage is

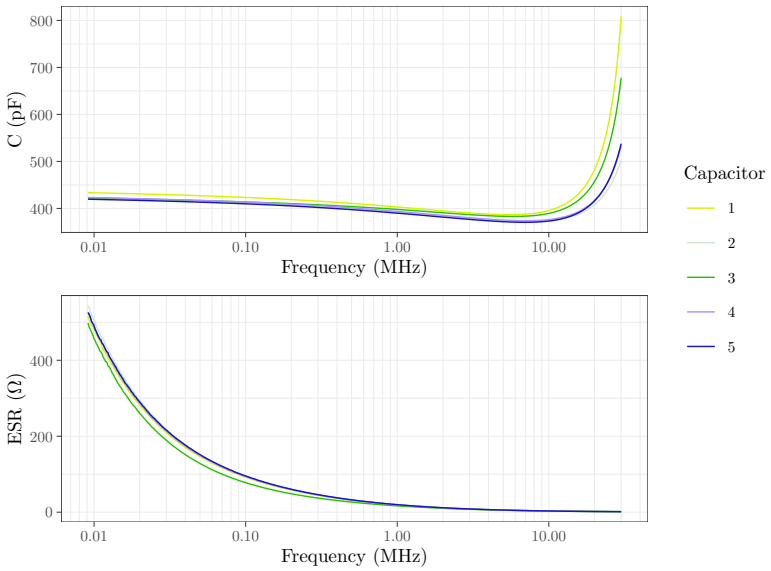


Figure 3.4: Capacitance and equivalent series resistance measurements of 3 different RIFA capacitors.

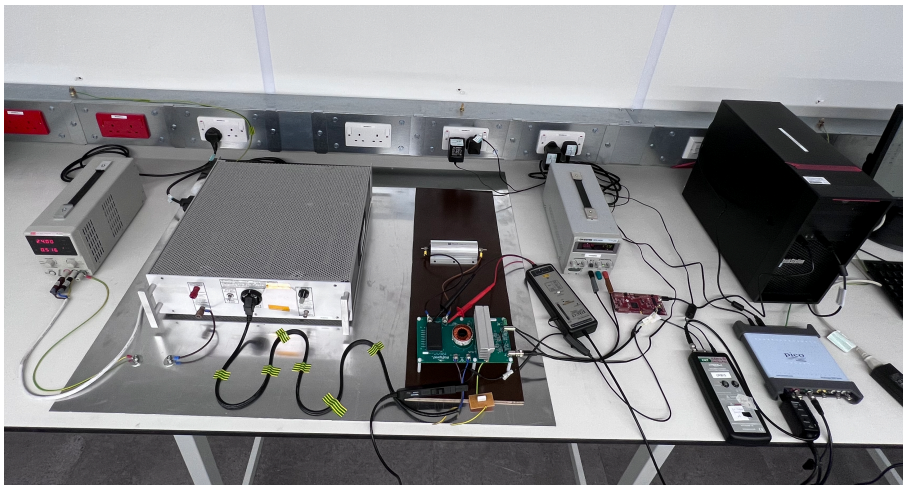


Figure 3.5: The experimental setup with the 470 pF RIFA capacitors placed between the DC/DC converter and the ground.

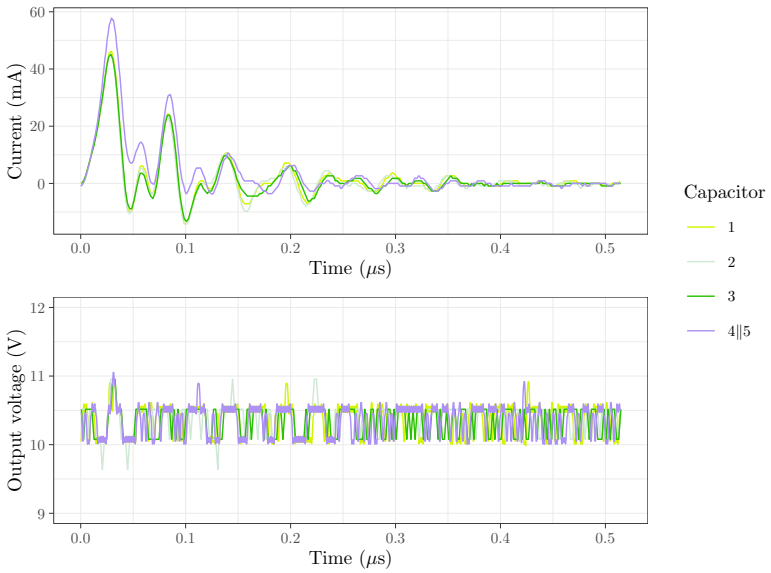


Figure 3.6: Damped oscillation of the common mode current and output voltage obtained from the experimental setup presented in Fig. 3.5.

however observed.

In the first case the impact of the different lengths of cables can be easily identified in the spectrum, due to evident increase (and decrease) in the magnitude at frequencies corresponding to the resonant frequencies of the cables, while in the second case there is a visible but small impact of the different capacitors on the common mode current, and no significant impact on the output voltage. In reality however, it is often unclear what the conditions are in the environment in which the PE will be used. Hence, it is difficult to identify the most important parasitics and assess their impact on the EMI currents and voltages. Proper identification of the most sensitive parasitic elements can help in focusing the attention of a designer or system integrator to overcome the problems caused by these parasitic elements. In this chapter, a methodology based on surrogate modelling techniques will be presented. The methodology allows to assess the influence of the parasitics elements on the QoI, and identify those which contribute the most to the variation of the QoI.

To that aim, the approach that has been taken in the next two chapters, is to assume that the values for the electrical parameters of the circuit are independent random variables. If the distributions of the random variables are not known, it is a standard approach to assume that they follow some maximum entropy distribution, i.e., a distribution which has the highest uncertainty [93]. In a continuous case, if random variable X has an infinite support, i.e. $(-\infty, \infty)$ and the mean μ and variance σ^2 are known, such maximum entropy distribution is a Normal distribution $\mathcal{N}(\mu, \sigma^2)$. However, in the case presented here, where each electrical parameter has bounded support $[a, b]$ such a maximum entropy distribution is a uniform distribution $\mathcal{U}(a, b)$ with a and b corresponding to, respectively, minimum and maximum value assumed for a given parameter. After modelling the electrical parameters as random uniform variables, simulations are used to consider the impact of these uncertain parameters on the QoI. Let us recall that in order to assess the probability of data frame rejection P_{error}, the models for RanM and DetM, shown in the previous chapter, require the knowledge of 3 parameters: the time between bit checking instants Δt, switching frequency f_s and parameter δ, i.e. the time during which the considered EMI signal is above a threshold V_{th}. While the first two parameters are decided by the designer of the PE circuit or dictated by the use of a particular communication standard, the last parameter depends on shape of the damped oscillation signal, which in turns relates to the electrical parameters of the circuits including parasitics. In this case, the final desired QoI is the parameter δ, obtained using two different methods: directly from comparison of the time-domain output signal with a threshold V_{th} (which will be denoted as δ_1); and indirectly, through a fusion of frequency-domain and time-domain signals from which the parameters v_0, f and λ of the damped oscillation signal can be recreated (which will be denoted δ_2). Therefore, effectively five parameters δ_1, v_0, f, λ, and δ_2 will

be considered as the QoI.

Moreover, the stochastic methods described in this chapter enable performing sensitivity analysis; that is, understanding which circuit parameters have the highest influence on the change in the QoI; this allows to understand which are the important parameters from a designer's or integrator's point of view. In order to perform the simulations, a simulation model of the circuit used in the experiment from Fig. 3.2 and Fig. 3.5 will be used. However, it should be noted that the intention of this chapter is not to exactly reproduce the experimental circuit, but rather to show a methodology which can be used in similar circuit simulations.

The structure of the next two chapters is as follows. First, the surrogate modelling methods PC and SVM will be referred. Next, sensitivity measures, known as Sobol' indices will be introduced. The measure used for validation of surrogate models with Monte Carlo will then be referred. Further, the simulation circuit will be shown together with the indication of the methods by which the parameters of the circuit were obtained. Finally, the results of the comparison between two surrogate modelling methods will be presented; the most sensitive parameters based on the Polynomial Chaos model will be shown.

3.2 Simulation circuit

The circuit used in the experiment depicted in Fig. 3.2 and Fig. 3.5 is Wolfspeed Cree KIT-CRD-3DD065P Buck-Boost evaluation kit. In this work, this circuit was modelled using Matlab Simulink. Schematic of the circuit modelled in Simulink is depicted in Fig 3.7.

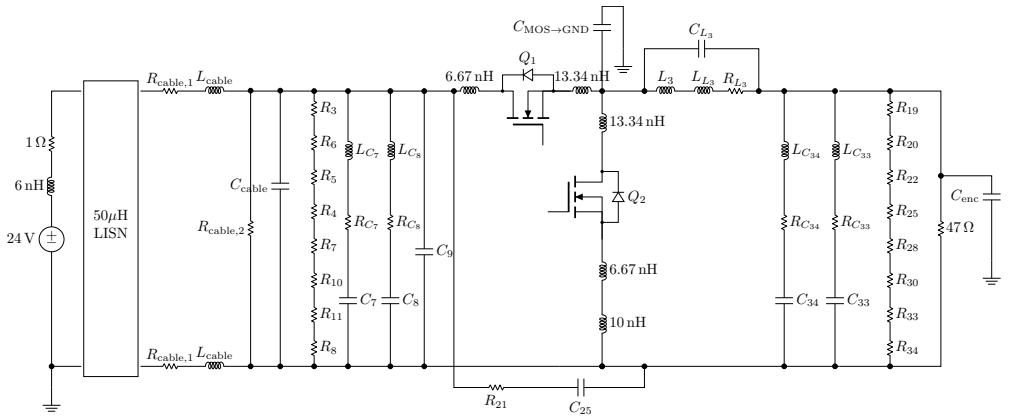


Figure 3.7: The schematic of the Wolfspeed Cree KIT-CRD-3DD065P Buck~~-Boost~~ circuit used for the simulations.

It should be noted that the Simulink model has not been made to represent as close as possible the real circuit used in the experiments but rather to show a methodology which can be applied to any given PE circuit. The circuit is connected to an equivalent model of a standard 50 μH CISPR-16 LISN, which is supplied by a DC voltage of 24 V. It is also assumed that the source has some internal impedance with resistance of 1 Ω and inductance of 6 nH. The DC/DC converter supplies a 47 Ω load. The values of both the load and LISN are considered static and fixed. The electrical parameters considered as random are indicated on the schematic with their symbol names.

The electrical elements of the circuit have been obtained from 'Appendix C: Schematic' and 'Appendix D: Bill of Materials' of the KIT-CRD-3DD065P Application Note[1]. When representing the circuit elements, the control part and auxiliary circuit has not been taken into account; instead, the focus was on representing the passive circuit elements that may have influence on power conversion. Moreover, the circuit elements were not modelled only in terms of 'ideal' capacitors, resistors and inductors, but their parasitic influences have been introduced as equivalent circuit models. When no

[1] https://assets.wolfspeed.com/uploads/2020/12/kit-crd-3dd065p_application_note.pdf [online]. Last accessed: 12.10.2023

information was provided regarding the parasitics of the respective circuit elements, the element was assumed to be 'ideal.' Additional inductances representing the parasitic inductances of the transistors have been obtained from an LTSpice simulation provided by the manufacturer of the circuit[2].

Additional to the circuit elements found on the DC/DC converter schematic, the input cables have been modelled as one RLC branch, representing the connection between the LISN and the PE circuit.

Furthermore, two additional capacitors have been included: C_{enc} to simulate capacitance between the load and the enclosure, and $C_{\text{MOS}\rightarrow\text{GND}}$ to simulate the capacitance between the board and the ground.

Following initial observations presented in previous sections, particularly in Fig. 2.15 and Fig. 3.6 those two capacitors were assumed to have the most impact onto the QoI. However, this assumption will be validated by the results of the simulations. The electrical parameters of the circuit are collected in Table 3.1.

Table 3.1: Input parameters of the circuit under consideration

Variable name	Nom. value	Tolerance (%)	Units	Description
R_3	1	1	MΩ	Input filter resistors
R_6	1	1	MΩ	
R_5	1	1	MΩ	
R_4	1	1	MΩ	
R_7	1	1	MΩ	
R_{10}	1	1	MΩ	
R_{11}	1	1	MΩ	

[2] https://www.wolfspeed.com/kit-crd-3dd065p/ [online]. Last accessed: 12.10.2023

Table 3.1: Input parameters of the circuit under consideration (continued)

Variable name	Nom. value	Tolerance (%)	Units	Description
R_8	1	1	MΩ	
R_{19}	1	1	MΩ	Output filter resistors
R_{20}	1	1	MΩ	
R_{22}	1	1	MΩ	
R_{25}	1	1	MΩ	
R_{28}	1	1	MΩ	
R_{30}	1	1	MΩ	
R_{33}	1	1	MΩ	
R_{34}	1	1	MΩ	
C_7	10	5	μF	Input filter capacitor
R_{C_7}	13	10	mΩ	ESR of C_7
L_{C_7}	21.13	50	nH	ESL of C_7
C_8	10	5	μF	Input filter capacitor
R_{C_8}	13	10	mΩ	ESR of C_8
L_{C_8}	21.13	50	nH	ESL of C_8
C_9	150	20	nF	Input filter capacitor
C_{33}	10	5	μF	Output filter capacitor
$R_{C_{33}}$	13	10	mΩ	ESR of C_{33}
$L_{C_{33}}$	21.13	50	nH	ESL of C_{33}
C_{34}	10	5	μF	Output filter capacitor
$R_{C_{34}}$	13	10	mΩ	ESR of C_{34}
$L_{C_{34}}$	21.13	50	nH	ESL of C_{34}
R_{21}	10	1	Ω	Auxiliary resistor
C_{25}	22	20	nF	Auxiliary capacitor
L_3	650	15	μH	Main inductor

Table 3.1: Input parameters of the circuit under consideration (continued)

Variable name	Nom. value	Tolerance (%)	Units	Description
L_{L_3}	1	15	nH	ESL of L_3
R_{L_3}	36	10	mΩ	ESR of L_3
C_{L_3}	60	30	pF	EPC of L_3
$R_{Q1,\text{on}}$	90	30	mΩ	ON-resistance of the MOSFET Q_1
$R_{Q2,\text{on}}$	90	30	mΩ	ON-resistance of the MOSFET Q_2
$C_{\text{MOS}\rightarrow\text{GND}}$	5	30	nF	Capacitance between the board and the ground
C_{enc}	5	30	nF	Capacitance between the load and the enclosure
$R_{\text{cable},1}$	52	10	mΩ	ESR of the input cable
L_{cable}	33.12	30	μH	ESL of the input cable
C_{cable}	0.95	30	pF	EPC of the input cable
$R_{\text{cable},2}$	1	1	MΩ	EPC of the input cable

3.2.1 Tolerances for electrical parameters

The nominal values and tolerances have been obtained in the following ways. Where possible, for elements contained in the 'Bill of Materials' obtained from the Application Note, the respective data sheets were collected through an internet search. Many of these data sheets contained information about the tolerances as well as the nominal values for the parasitics of the respective elements. In case of several exceptions, the following rules have been adopted.

Extraction of ESR tolerances

If the tolerances of ESR have not been provided in the data sheet, the work of Sumsurooah *et al.* [94] has been followed, where the authors showed that the resistances exhibit 10% deviations due to temperature changes; this is the case for the ESRs R_{C_7}, R_{C_8}, $R_{C_{33}}$, $R_{C_{34}}$, of the input and output capacitors, and ESR R_{L_3} of the main inductor as well as the ESR $R_{cable,1}$ of the input cable.

Extraction of Equivalent Series Inductance for Film Capacitor

Elements C_7, C_8, C_{33} and C_{34} are Vishay $10\,\mu$F film capacitors with serial number MKP1848S61010JY2B. The data sheet is available from the manufacturer's website[3]. The data sheet states the tolerance for the capacitance, equal to 5%. Also specified is the value of the ESR, equal to $13\,\mathrm{m}\Omega$, while the tolerance for the ESR has been assumed to be 10% as stated above.

The ESL of the capacitor is not given explicitly, nor is the tolerance for the ESL. In this case however, Page 8 of the data sheet presents plots of the impedance, with indicated resonant frequency. One can aim to estimate the resonant frequency by looking at the plot, which cannot be reproduced here due to copyright issues. Since the nominal value is not clear, one can instead assume that the resonant frequency is between a certain range $[f_{\min}, f_{\max}]$, where, in this case $f_{\min} = 0.3\,\mathrm{MHz}$ and $f_{\max} = 0.4\,\mathrm{MHz}$. Similarly, the value of the capacitance C can be assumed to be within the range $[C_{\min}, C_{\max}]$. Then, the value of L as well as the tolerance can be taken from the well-known relationship between the resonant frequency, inductance and capacitance in an LC circuit.

[3] https://www.vishay.com/docs/26010/mkp1848sdclink.pdf [online]. Last accessed: 12.10.2023.

In simple LC circuits the equation for a resonant frequency writes

$$f_0 = \frac{1}{2\pi\sqrt{LC}}, \tag{3.1}$$

which, solved for L gives

$$L = \frac{1}{4\pi^2 f_0^2 C}. \tag{3.2}$$

Assuming that both the resonant frequency and the capacitance are uniform variables, one calculate the mean and standard deviation of L, using direct derivations or with the help of a symbolic computer software such as Mathematica or Maxima. We have

$$\begin{aligned} \mathrm{E}(L) &= \frac{1}{4\pi^2 f_{\max} f_{\min}} \frac{\log C_{\max} - \log C_{\min}}{C_{\max} - C_{\min}} \\ \mathrm{Var}(L) &= \frac{f_{\max}^2 + f_{\max} f_{\min} + f_{\min}^2}{48\pi^4 C_{\max} C_{\min} f_{\max}^3 f_{\min}^3} \\ &\quad - \frac{(\log C_{\min} - \log C_{\max})^2}{16\pi^4 (C_{\min} - C_{\max})^2 f_{\max}^2 f_{\min}^2} \end{aligned} \tag{3.3}$$

The nominal capacitance stated in the data sheet is $C_{nom} = 10\,\mu\mathrm{F}$ and the tolerance is 5%. Therefore, substituting real numbers for $C_{\min}, C_{\max}$, obtained from the data sheet and for $f_{\min} = 0.3\,\mathrm{MHz}$ and $f_{\max} = 0.4\,\mathrm{MHz}$ we obtain

$$\begin{aligned} \mathrm{E}(L) &= 21.1262\,\mathrm{nH}, \\ \mathrm{Var}(L) &= 1.27807 \cdot 10^{-17}(\mathrm{H})^2, \\ \mathrm{Std}(L) &= 3.57501 \cdot 10^{-9}\mathrm{H} \\ &= 3.57501\,\mathrm{nH}. \end{aligned} \tag{3.4}$$

Next, a sanity check can be performed to derive the oscillation frequency based on the nominal value of capacitance and the mean value of the equivalent series inductance. Using equation (3.1) one can check that the resonant frequency $f_0 \approx 0.346\,\mathrm{MHz}$ which is visually consistent with the data sheet figure.

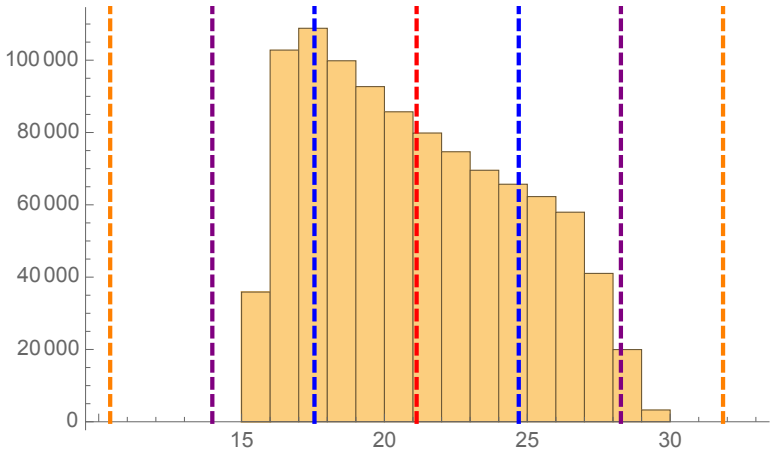


Figure 3.8: Histogram of L obtained from 10,000 Monte Carlo samples using Eq. (3.2) with indicated $\mathrm{E}(L)$, $\mathrm{E}(L)+/-\mathrm{Std}(L)$, $\mathrm{E}(L)+/-2\,\mathrm{Std}(L)$, and $\mathrm{E}(L)+/-3\,\mathrm{Std}(L)$.

In order to find the tolerance, one can simply find the proportion between the standard deviation and the mean value, which amounts to around 16%. However, use of that proportion as input to simulations needs explanation. In fact, the resulting distribution for L is not uniform, as is shown on Fig. 3.8, which presents a 10,000 Monte Carlo samples of L obtained from Eq. (3.2). Indicated on the figure are also the mean $\mathrm{E}(L)$ as well as the standard deviations. The resulting distribution is asymmetric and right-skewed. One can see that the estimated distribution fits within 3 standard deviations. In this case one standard deviation corresponds to around 16% tolerance, 2 standard deviations to around 33% and 3 standard deviations to around 50% tolerance. For the purpose of simulations presented in this work, we follow the original assumption that any random electrical parameter of the circuit follows a maximum entropy distribution, and instead of assuming that the value of L follows a right-skewed distribution as shown in Fig. 3.8, we assume it follows a uniform distribution with nominal value $E(L)$ and the tolerance 50% corresponding to 3 standard deviations. The latter choice was made due to the fact that the range of values obtained from 10,000 MC simulations fits within the 3 standard deviations as seen

in Fig. 3.8.

Resistances for the MOSFET

The power transistor used in the original circuit is the Cree C3M0060065K Silicon Carbide Power MOSFET. The data sheet of the MOSFET is available at the manufacturer's website[4]. The parameters of the MOSFET are assumed to follow the values specified in the data sheet, and the only random variable is the ON-resistance, where it can be supposed that the value of the resistance may change significantly, particularly due to temperature changes during operation. Fig. 5 and 6 on Page 4 of the data sheet shows the value of ON-resistance for different operating conditions. It can be seen that the value varies between 60 mΩ and 120 mΩ. For the purpose of this work it can be therefore assumed that the nominal value of the ON-resistances $R_{Q1,\text{on}}$ and $R_{Q2,\text{on}}$ are equal to 90 mΩ with 30% tolerance.

3.3 Simulations and the Quantity of Interest

As stated in Section 3.1 in order to use the models developed for DetM and RanM, one needs to know three important parameters: the switching frequency f_s, the time between bit checking Δt and finally the time δ during which the damped oscillation signal is above a predefined threshold. The first two parameters are set by the designer or user of the circuit, while the last parameter depends on the random parameters of the circuit. This section provides two ways of obtaining the parameter δ.

The circuit from Fig. 3.7 was implemented in Matlab Simulink using Sim-

[4] https://assets.wolfspeed.com/uploads/2020/12/C3M0060065K.pdf [online]. Last accessed: 12.10.2023.

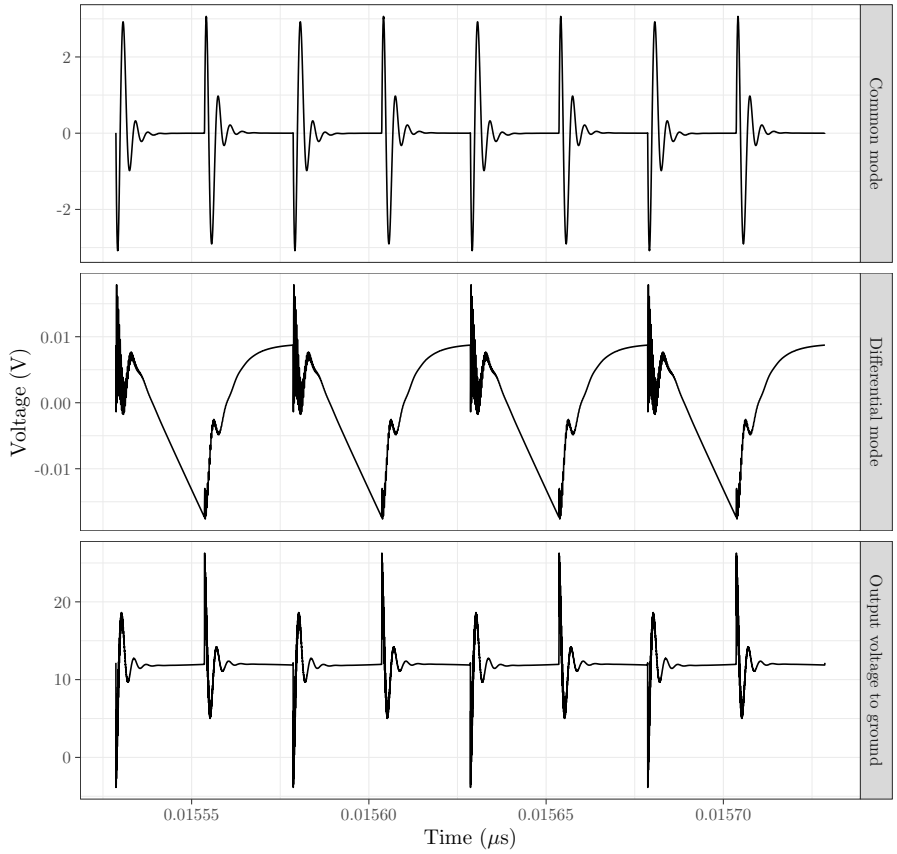


Figure 3.9: Time domain signals obtained from simulations.

scape Electrical toolbox. The circuit was simulated for 0.02 s with a sampling frequency of 80 MHz. Fig. 3.9 presents three time-domain voltages obtained from the last three switching periods of a single simulation run. The three signals are CM voltage, DM voltage and Output voltage-to-ground, i.e. the voltage between the positive terminal of the load to ground. The damped oscillation both at the CM voltage and output voltage-to-ground are clearly visible. A high frequency damped oscillations are also seen in the DM voltage. The peak and average spectra of the CM and DM voltages are depicted in Fig. 3.10.

Visible are clear modes of the resonant frequencies. However, the dominant resonance of the highest magnitude is between 0.1 MHz and 1 MHz, which can be clearly seen on the panel presenting the CM voltage.

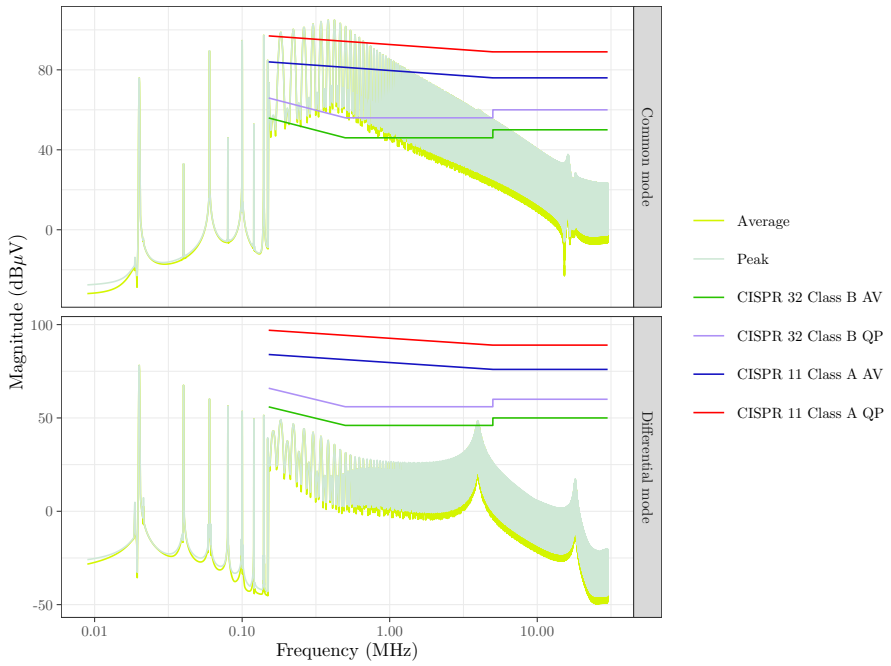


Figure 3.10: Common and differential mode voltages obtained from the Matlab simulation.

The dominant oscillation frequency of the CM voltage seems to be similar to the dominant oscillation of the output voltage to ground. This is the signal that will be of focus here.

Let us recall the parameters of the damped oscillation from Eq. (2.2). They are

- v_0 - the ringing amplitude,
- f - the ringing frequency,
- λ - the decay rate.

These parameters can be obtained directly from time-domain simulations (v_0) and frequency-domain data (f and λ). It is also clear that these parameters depend on the values of circuit elements and parasitics. Fig. 3.11 a) presents half of the last switching period, and is a result of 10 different simulations, where the parameters for the circuit under consideration were

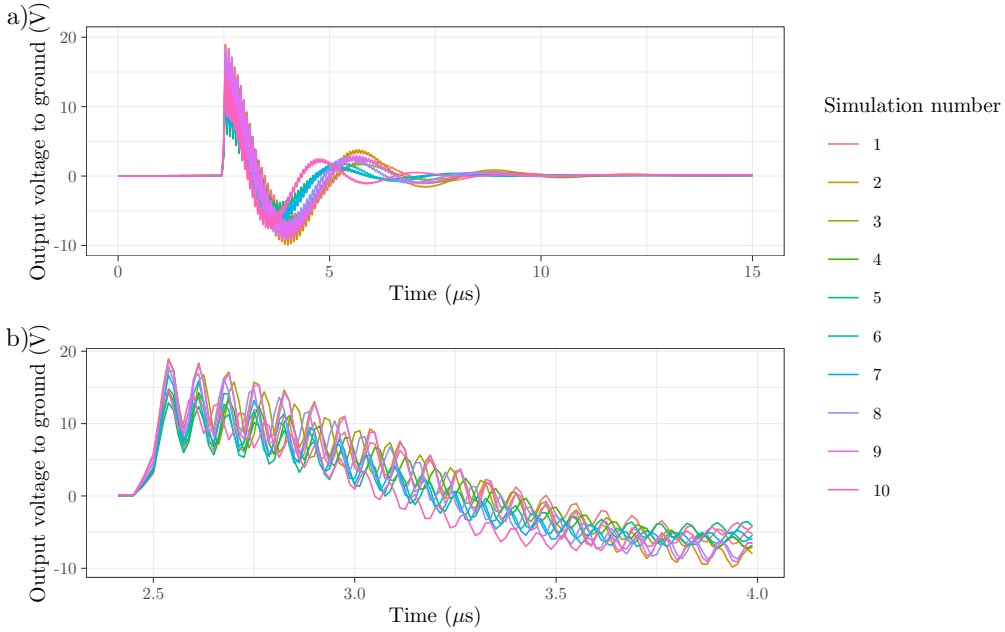


Figure 3.11: Scaled output voltage to ground obtained from the simulations considering random values of the parameters.

randomly selected from a Latin Hypercube Sampling (LHS) scheme. Moreover, in the figure, the output voltage was standardized by subtracting the DC output value 11.9 V from the signal. One can see that resonant frequency, as well as the damping parameters and the amplitude are different between the 10 trials. Therefore, the resulting δ will also be different between the different trials.

Parameter δ can be obtained directly from time domain simulations by imposing a threshold on the signal and assessing the time that the signal is above the threshold. In this case the threshold was set to 10 V. However, the time-domain signals visible on Fig. 3.11 have many high-frequency oscillations. Therefore, to simplify the task, the dominant signal needs be extracted. Two methods of extracting δ have been used and described below.

Extraction of δ from time-domain simulations

The first method extracts δ directly from the last portion of the time-domain signal. Since the time-domain signal $V(t)$, as seen on Fig. 3.11 is not a smooth damped oscillation, the high and low envelope, respectively $V_h(t)$ and $V_l(t)$ of the signal were first obtained, using Matlab's function `envelope`. Then, the envelopes were averaged, i.e. $V_1(t) = 0.5(V_h(t) + V_l(t))$, and the parameter δ was obtained directly as the length during which the signal $V_1(t)$ exceeds the threshold V_{th}.

Extraction of δ from frequency-domain simulations

Fig. 3.12 a) presents the power spectrum of the output voltage to ground. Indicated is the range between 0.1 MHz and 1 MHz.

In order to collect the frequency f and decay rate λ, the fragment of the spectra between 0.1 MHz and 1 MHz was filtered. Next, an envelope was computed using Matlab's function `envelope` to smooth the peaks. Point with the highest magnitude was later found using function `findpeaks`, and is indicated on Fig. 3.12 b) with a blue point. The corresponding frequency is the oscillation frequency f.

Next, in order to estimate λ, the following procedure was applied.

Find the farthest frequency f_l smaller than f, for which the value of power spectrum $S(f_l)$ at f_l is less than 3 dB smaller than the value of the power spectrum $S(f)$ at f, i.e. $S(f) - S(f_l) > 3$. Since the frequency vector is discretized with a step of 100 Hz, find the next frequency $f_{l_1} < f_l$ and the

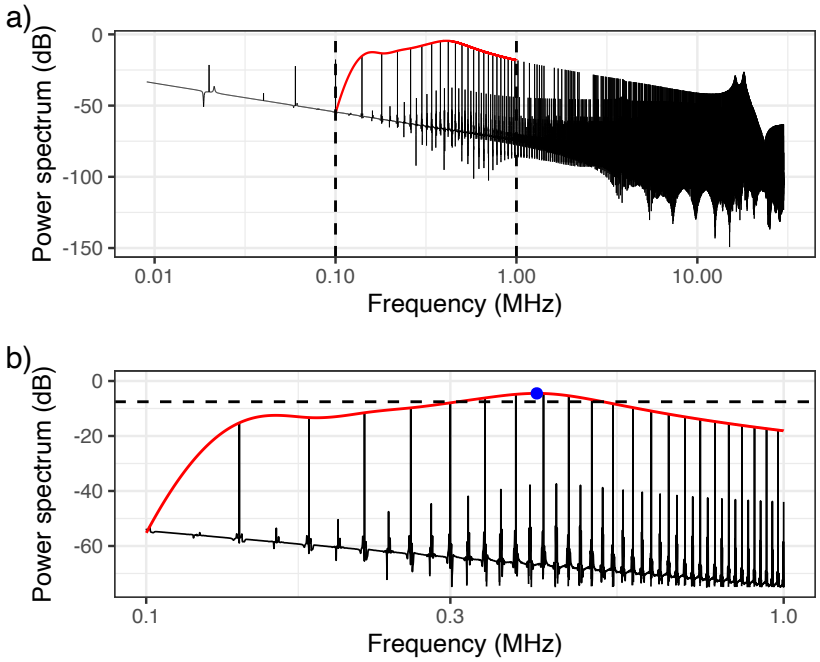


Figure 3.12: a) Power spectrum of the voltage-to-ground with 0.1 MHz and 1 MHz indicated by the dashed lines and the envelope of the power spectrum depicted by the red solid line; b) The fragment of the power spectrum between 0.1 MHz and 1 MHz, with the peak of the oscillation frequency indicated by a blue dot and dashed line indicating -3 dB from the peak.

corresponding value of $S(f_{l_1})$. Next, create a linear function

$$S(f) = \frac{S(f_{l_1}) - S(f_l)}{f_{l_1} - f_l} f + \frac{f_{l_1} S(f_l) - f_l S(f_{l_1})}{f_{l_1} - f_l} \tag{3.5}$$

and use a Newton-Raphson algorithm to find the f_l^* which solves the equation $S(f_l^*) - 3 = 0$. Repeat the same procedure to find $f_r^* > f$, a frequency located to the right of f for which the value of the power spectrum $S(f_r^*)$ is 3 dB lower than $S(f)$.

Now, having f_l^* and f_r^*, use the following equations to compute the decay rate λ [95]

$$Q = \frac{f}{f_r^* - f_l^*}, \tag{3.6}$$

$$\beta = \frac{\pi}{Q}, \tag{3.7}$$

$$\zeta = \frac{\beta}{\sqrt{\beta^2 + (2\pi)^2}}, \tag{3.8}$$

$$\lambda = \left| \frac{2\pi f \zeta}{\sqrt{1-\zeta^2}} \right|. \tag{3.9}$$

This set of equations is used to compute the decay rate from the so-called Q-factor, i.e. a parameter that measures the strength of damping of the oscillations in a circuit.

The amplitude v_0 is obtained from the time-domain simulation as the maximum of the averaged signal $V_1(t)$. Next, the damped oscillation signal is created from equation

$$V_2(t) = v_0 \cos(2\pi f t) \exp(-\lambda t), \tag{3.10}$$

and parameter δ is obtained as the duration of $V_2(t)$ exceeding the threshold V_{th}.

Extraction of the parameter δ from signals $V_1(t)$ and $V_2(t)$ obtained with the usage of the above methods is depicted in Fig. 3.13. These parameters will be referred to as δ_1 and δ_2 respectively. It can be seen that there is a small difference between the two techniques, which will be likely present in the results of the simulations. It should be also mentioned that there are other methods which could be used to reproduce the damped oscillation signals, such as vector fitting [96, 97] or Prony's method [98]. However, in this case two simplest and intuitive methods were selected that do not require gathering poles and residuals of the rational function, nor eigenvalues of such functions. The described methods will be considered in the next chapter for the creation of the surrogate models and optimizing the circuit.

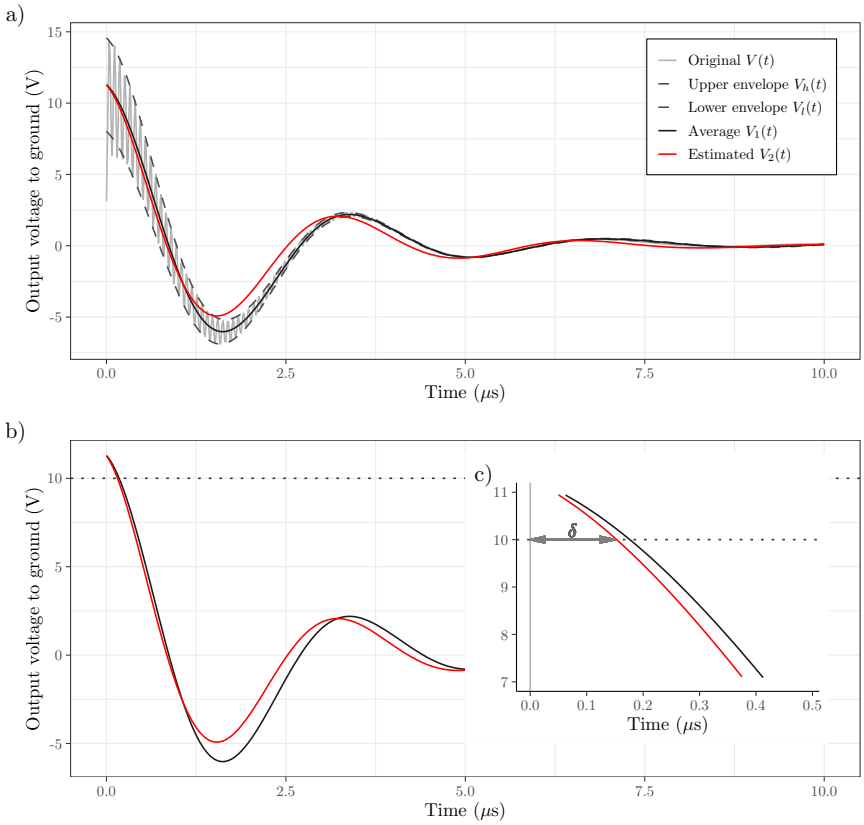


Figure 3.13: Extraction of δ using the two methods, based solely on time-domain signal and based on frequency-domain signal.

3.4 Surrogate modelling methods

Having described the circuit as well as the QoI, now the methods will be presented, used for the remainder of this thesis. The methods will be recalled only briefly, and the interested reader is referred to the Appendices A-D in which the methods are described in a greater detail with mathematical background.

In particular, MC method will be used as a benchmark for the comparison of the two surrogate modelling methods. In this work, the samples to perform MC simulations are obtained through the usage of LHS scheme [99], which proved to be the best among four compared sampling schemes in the previous work co-authored by the author of this thesis [100].

As widely, known MC is a time-consuming technique, therefore surrogate modelling will be used to alleviate the need for performing many time-consuming simulations. Broadly speaking, surrogate modelling consists of drawing a few input samples of the random vector $\boldsymbol{X}$, collecting the QoI Y evaluated at these samples, and building a mathematical model $\mathcal{M}$ that approximates the QoI as follows

$$\mathcal{M}(\boldsymbol{X}) \approx Y. \tag{3.11}$$

This equation is a general form of a surrogate model; however, in the case of simulations presented hereafter vector $\boldsymbol{X}$ collects the random parameters from Table 3.1, while Y is a random variable representing any of $\delta_1, v_0, f, \lambda$ and δ_2. The approximation $\mathcal{M}$ can later be used for analysis, or for an MC-like sampling.

In the EMC world, some surrogate modelling techniques that have been already used are genetic algorithms [65], affine arithmetic [66], unscented transform [67], dimension reduction techniques [68], Polynomial Chaos (PC) [54, 55], and μ-analysis [69]. The two surrogate methods that will be used in the remainder of this thesis are sparse Polynomial Chaos (sPC) method and Support Vector Machine (SVM), following the two previous papers published by the author of this thesis [72, 74].

A surrogate model built by the PC method will be denoted $\mathcal{M}^{\mathrm{PC}}$, and a surrogate model obtained with SVM will be denoted $\mathcal{M}^{\mathrm{SVM}}$. The rationale behind selecting these two particular techniques is that neither of them depends on the number of input variables. Therefore, the number of simulations does not need to increase when increasing the number of input variables; what is known as a *curse of dimensionality* [101].

For the clarity of the discussion presented hereafter, the mathematical details regarding the models can be found in the Appendices. However, let us only mention a general form of the two surrogate models. The PC model expresses the QoI in terms of orthogonal polynomials as follows [101]

$$\mathcal{M}^{\mathrm{PC}}(\boldsymbol{X}) = \sum_{\boldsymbol{\alpha}\in\mathcal{A}} c_{\boldsymbol{\alpha}} \Psi_{\boldsymbol{\alpha}}(\boldsymbol{X}), \tag{3.12}$$

where

- $\mathcal{A} \subset \mathbb{N}^n$ is a set which consists of multi-indices $\boldsymbol{\alpha} = (\alpha_1, \ldots, \alpha_n)$,
- $\Psi_{\boldsymbol{\alpha}}(\cdot)$ are the orthogonal polynomials,
- $c_{\boldsymbol{\alpha}}$ are the coefficients of the expansion.

In traditional PC approaches the number of coefficients $c_{\boldsymbol{\alpha}}$ grows exponentially with increasing number of input variables. For instance, for the number of parameters 43 assumed in this work, the usual number of required simulations would amount to $15,180$. However, the sPC method used in the remainder of this thesis selects only a fraction of the orthogonal polynomials, therefore significantly reducing the needed number of simulations. Three algorithms for selecting the sparse basis of polynomials will be compared: Least-Angle Regression (LARS), Orthogonal Matching Pursuit (OMP), and Subspace Pursuit (SP) [102].

The SVM model expresses the QoI as follows [103]

$$\mathcal{M}^{\mathrm{SVM}}(\boldsymbol{X}) = \sum_{i=1}^{K} c_i k\left(\boldsymbol{X}; \boldsymbol{x}^{(i)}, \sigma\right) + c_0, \tag{3.13}$$

where

- $\boldsymbol{x}^{(1)}, \ldots, \boldsymbol{x}^{(K)}$ are the K samples of input variables,

- $k\left(\boldsymbol{X}; \boldsymbol{x}^{(i)}, \sigma\right)$ is a *kernel* function,
- σ is one of the hyperparameters of the SVM model,
- c_i are the coefficients of the model.

Parameter σ represents the width of the kernel function $k\left(\boldsymbol{X}; \boldsymbol{x}^{(i)}, \sigma\right)$. Kernels are called *anisotropic* if for each random variable $X_1, \ldots, X_n$ a separate width $\sigma_1, \ldots, \sigma_n$ is used, which results in the kernel function created as product of one-dimensional kernels, i.e.

$$k\left(\boldsymbol{X}; \boldsymbol{x}^{(i)}, \boldsymbol{\sigma}\right) = \prod_{j=1}^{n} k\left(X_j; x_j^{(i)}, \sigma_j\right), \tag{3.14}$$

for each $i = 1, \ldots, K$. If parameter σ is constant throughout the dimensions, then such kernel is called *isotropic*. In this work, several isotropic and anisotropic kernels will be compared: Gaussian, Matern 3/2 and Matern 5/2 (see Appendix C).

The coefficients c_i are found by minimizing a certain loss function ℓ^{ε}, which is dependent on the width ε of the so-called error tube. In this work, two types of loss functions will be used, according to L1 and L2 formulations, denoted respectively ℓ_1^{ε} and ℓ_2^{ε} [103].

In the EMC world the SVM method has only been studied recently, and apart from the author's own work [72], no other researchers studied the impact different loss functions [70, 71, 104]. Which will be considered in the next chapter. Moreover, the author of this thesis, in paper [72] presented a comparison between different algorithms which tune the hyperparameters of an SVM model, such as the kernel parameter σ and the width ϵ, with respect to the accuracy and computational efficiency. As a result, in the next chapter, the winning algorithm, BFGS will be used to train hyperparameters of SVM models.

The sPC method, on the other hand, is a widely adopted method [54, 55]. However, apart from comparing three algorithms for selecting the sparse basis, additionally, the so-called Sobol' indices [105] are collected, which help to identify the most important parameters of the circuit. It is also shown how the identification of these parameters can help in reducing the parameter δ, which in turn reduces the probability of error P_{error}; all of which has not been discussed by other researchers.

3.5 Validation measure

Two notions of error will be used in the next chapter. The first one, the so-called leave-one-out error (LOO), is used to train the $\mathcal{M}^{\text{SVM}}$ and $\mathcal{M}^{\text{PC}}$ models. The LOO error will be denoted $\hat{\epsilon}_{\text{LOO}}$, and the interested reader is referred to Appendices B and C for information on how to compute $\hat{\epsilon}_{\text{LOO}}$ for PC and SVM models.

The second notion is the error used to compare the results of the surrogate models with the MC results, a validation measure known as *a posteriori* error, which reads

$$\hat{\epsilon} = \frac{K-1}{K}\left(\frac{\sum_{i=1}^{K}(y^{(i)} - \mathcal{M}(\boldsymbol{x}^{(i)}))^2}{\sum_{i=1}^{K}(y^{(i)} - \hat{\mu}_Y)^2}\right), \tag{3.15}$$

where $y^{(i)}$ is the true response of the system for the input $\boldsymbol{x}^{(i)}$, and $\hat{\mu}_Y$ is the sample mean of those responses. The interpretation of this validation measure is as follows. First, it is clear that $\hat{\epsilon} > 0$; however $\hat{\epsilon}$ is not bounded by any b such that $\hat{\epsilon} < b$. Now, if the value of $\hat{\epsilon}$ is higher than 1, it can be concluded that the validated model performs worse than a sample mean. That is, instead of using the predictions of the model $\mathcal{M}(\boldsymbol{X})$, one can use $\hat{\mu}_Y$ and this would on average yield better predictions. Finally, the closer

the value of $\hat{\epsilon}$ to 0, the better the predictions of the model $\mathcal{M}(\mathbf{X})$.

3.6 Conclusion

This section presented the modelling of a PE converter which includes uncertain parasitic elements. The PE circuit was modelled in Matlab Simulink, following the specification of Wolfspeed Cree KIT-CRD-3DD065P Buck-Boost evaluation kit and simulation models provided by the manufacturers. The nominal values and tolerances for the uncertain parameters were obtained directly from the data sheets of converter's electrical elements, as well as indirectly through computations based on the data provided in the data sheets. Further, these values were incorporated in the simulations by modelling the electrical parameters of the circuit as independent uniform random variables. Next, the parameter δ, i.e. the time above which a signal exceeds a threshold V_{th} was identified as the final QoI that needs to be captured to assess the harmful impact of the PE converter onto nearby serial communication devices. Two methods of extracting δ from the simulations were then shown, one based solely on time-domain signals, and the second based on the fusion of time domain and frequency domain data. Finally, two surrogate modelling methods, PC and SVM, were presented. These two methods will be used and compared in the next chapter, and the best among them will be selected to allow identifying the most important parasitic elements and enable optimization of the circuit.

Chapter 4

Surrogate modelling results

The previous section presented the modelling of a PE circuit with parasitic elements modelled as uniform random variables. Moreover, the two surrogate modelling techniques PC and SVM were introduced, together with two notions of error. In this chapter, these methods are used to perform simulations. The most suitable surrogate modelling technique is then selected based on the prediction error and the stability of the behaviour. Finally, the selected surrogate model is used for performing the sensitivity analysis, identifying the most important parasitic parameters and enabling optimization of the circuit, i.e. reducing the probability of error P_{error}.

4.1 Initial Monte Carlo simulations

Let us recall that δ_1 and δ_2, represent parameter δ obtained from, respectively, signal $V_1(t)$ and $V_2(t)$, i.e. obtained directly from time-domain simulations and from the fusion of time-domain and frequency-domain calculations. For verification purposes 5,000 MC simulations were computed, using LHS sampling scheme. From each simulation, five parameters were

obtained, namely the oscillation frequency f, the decay rate λ (computed from the procedure described above), the maximum amplitude v_0 and parameter δ_1 obtained directly from time-domain simulations. For each triple f, λ, v_0, parameter δ_2 was then computed. Fig. 4.1 presents distributions of δ_1 and δ_2 obtained from the MC simulations. Both methods indicate that

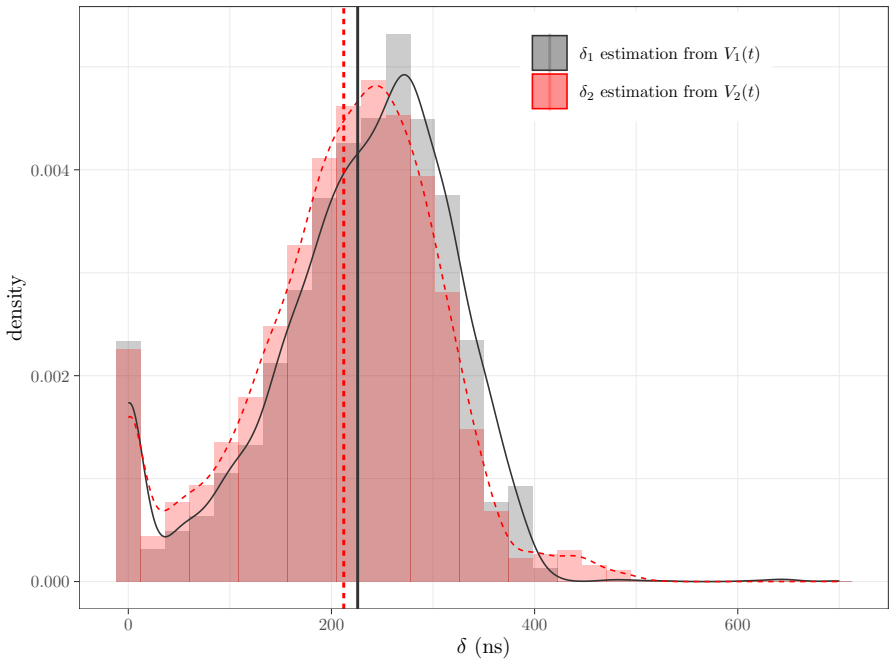


Figure 4.1: The distributions of δ, obtained from two discussed methods.

for a large proportion of the simulations, the damped oscillation signal was always below the threshold V_{th}, i.e. parameter δ was nearing zero. In the analysis it turned out that for each of these cases, the maximum amplitude v_0 was below the threshold $V_{\text{th}} = 10$.

Moreover, it can be clearly recognized that the distributions of δ obtained from the two methods are different. In fact, without considering all the cases for which $\delta_1 = \delta_2 = 0$, the mean error between the predictions of the model is approximately 16.42 ns. Applying a paired t-test to all the pairs of δ_1 and δ_2, (neglecting all the cases with $\delta_1 = \delta_2 = 0$) with a confidence level $\alpha = 0.95$ indicates that hypothesis $\mathrm{E}(\delta_1) = \mathrm{E}(\delta_2)$, should be rejected in favour of the alternative hypothesis that $\mathrm{E}(\delta_1) \neq \mathrm{E}(\delta_2)$ with a p-value

$< 2.2 \cdot 10^{-12}$. However, if δ_2 is adjusted by adding 16.42 ns to it, the t-test indicates that the difference in means is not significantly different, that is the null hypothesis can be accepted with p-value equal to 0.9916, i.e. close to 1. If one considers that the parameter δ_1 obtained directly from time-domain simulations is the benchmark, that implies there is a systematic error in extracting δ_2, which however can be adjusted after adding the appropriate constant of 16.42 ns to it. Note, that the phase portion of the spectrum was not considered when obtaining δ_2, therefore it is conceivable that such a time delay might occur when performing the FFT. Moreover, one might be more interested in the range of δ rather the mean value itself.

Now, let us consider the probabilities of rejection of the whole data frame, using models for RanM and DetM. Let us consider the following parameters: $f_s = 20\,\text{kHz},\ \Delta t = 17.12\,\mu\text{s},\ \tau = 1\,\text{ns}, n = 280$ last three being the same as in Chapter 2.

Table 4.1 presents the quantiles of δ_1 and δ_2 along with the prediction of errors considering the values of δ_1 and δ_2 derived for RanM and DetM models.

Table 4.1: The 5%, 25%, 50%, 75%, and 95% quantiles of δ and the average value E(δ) obtained from the two discussed methods, as well as the corresponding probabilities of frame rejection P_{error} derived for the RanM and DetM models.

		5%	25%	50%	75%	95%	E(δ)
	δ_1 (ns)	0	175	237	287	350	226
P_{error}	RanM	0.00	0.6232	0.7340	0.7993	0.8595	0.7170
	DetM	0.00	0.4427	0.5794	0.6464	0.7155	0.5551
	δ_2 (ns)	1	160	223	275	344	212
P_{error}	RanM	0.0055	0.5901	0.7122	0.7853	0.8546	0.6939
	DetM	0.00	0.4096	0.5485	0.6310	0.8450	0.5243

The discussed Monte Carlo simulations will be used to measure the accuracy of the surrogate models, developed with PC and SVM. That is, for

models $\mathcal{M}^{\mathrm{SVM}}$ and $\mathcal{M}^{\mathrm{PC}}$ the *a posteriori* error $\hat{\epsilon}$ will be computed. Moreover, the models will be also compared by the showing the values of the leave-one-out error $\hat{\epsilon}_{\mathrm{LOO}}$.

4.2 SVM surrogate modelling results

This section presents the comparison between the surrogate models in predicting the QoI, that is, respectively δ_1, v_0, f, λ, and δ_2. We will start with discussing the SVM models. Let us recall that the SVM models were built using two types of penalization scheme, l_1^ε and l_2^ε, three kernel functions: Gaussian, Matern 3/2 and Matern 5/2, and each kernel function was either isotropic or anisotropic. The hyperparameters of the kernel function, that is the ε-boundary, complexity parameter H and kernel parameter σ (or kernel parameters σ_i in case of anisotropic kernels), were trained using the BFGS algorithm, following my earlier paper [72]. That gives 12 different models to be trained. Moreover, let us recall that the $\hat{\epsilon}_{\mathrm{LOO}}$ error was used for training the models, and the *a posteriori* error $\hat{\epsilon}$ was then computed on the validation data.

Fig. 4.2 presents the errors $\hat{\epsilon}_{\mathrm{LOO}}$ and $\hat{\epsilon}$ for δ_1. It can be noticed that there is not much difference between the models for this parameter. Errors obtained from all models decrease with increasing experimental design size K. Moreover, the errors are below 1, i.e. the models perform better than the simple average, however they do not reach close to zero; in fact, they are always above 0.2. In general, it can be supposed that the validation error $\hat{\epsilon}$ will be larger than the leave-one-out error $\hat{\epsilon}_{\mathrm{LOO}}$ used for training, however what is interesting is that $\hat{\epsilon}_{\mathrm{LOO}}$ is very similar to $\hat{\epsilon}$. This indicates that the models generalize well; that is, the model did not overfit during

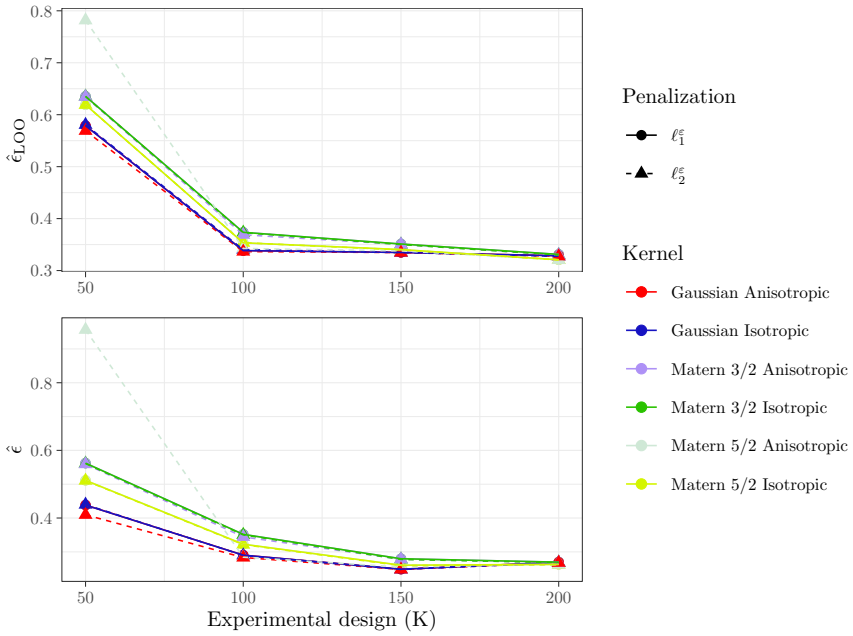


Figure 4.2: The errors $\hat{\epsilon}_{\text{LOO}}$ and $\hat{\epsilon}$ of SVM models for δ_1.

the training phase.

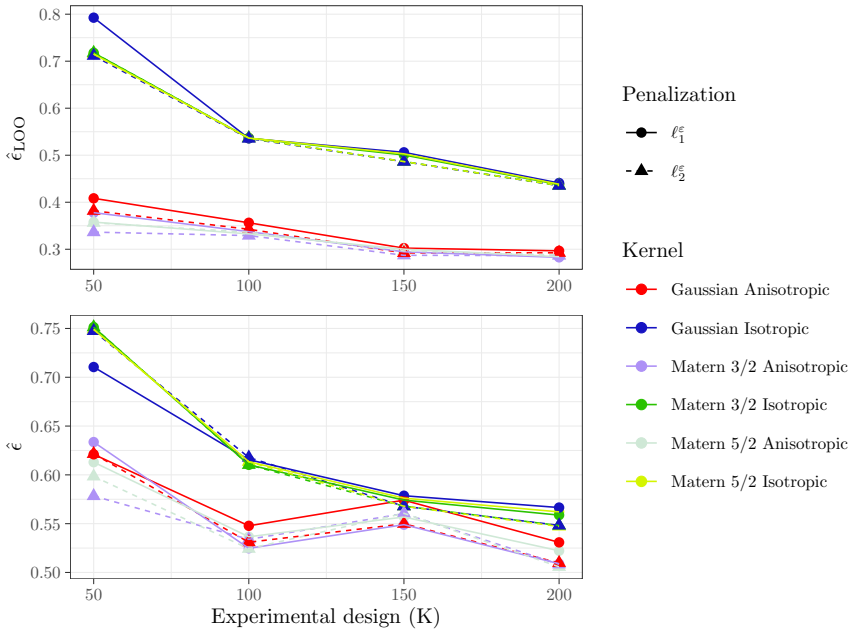


Figure 4.3: The errors $\hat{\epsilon}_{\text{LOO}}$ and $\hat{\epsilon}$ of SVM models for v_0.

Fig. 4.3 presents errors $\hat{\epsilon}_{\text{LOO}}$ and $\hat{\epsilon}$ for the maximum amplitude v_0. Let us recall that both δ_1 and v_0 are the two parameters obtained directly from time-domain signals. The overall trend of the errors is that they decrease

with increasing number of samples K. Moreover, just as in previous case, they are all below 1, better that the average. However, clearly distinguishable are two groups of errors, which correspond to anisotropic and isotropic kernels. The anisotropic have smaller errors than the isotropic ones. Regardless, $\hat{\epsilon}_{\text{LOO}}$ for both groups are larger than 0.3, and the validation error is above 0.5. However, the decreasing trend promises that with higher number of simulations the resulting models will perform better.

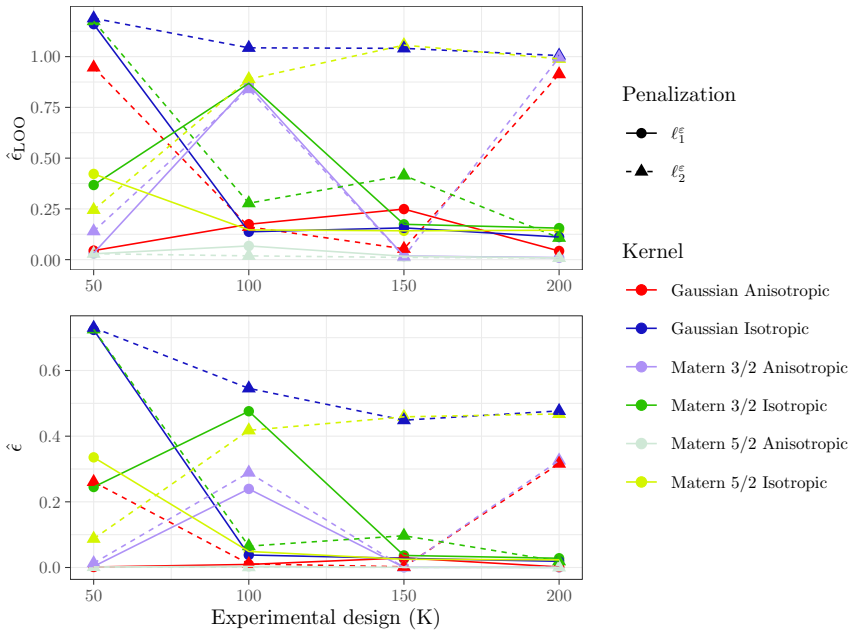


Figure 4.4: The errors $\hat{\epsilon}_{\text{LOO}}$ and $\hat{\epsilon}$ of SVM models for f.

Further, Fig. 4.4 presents the results of SVM models with respect to predicting the oscillation frequency f. In this case it can be seen that both the leave-one-out error and the *a posteriori* error indicate a very unstable behaviour of the models. It can be noticed that in the case of Gaussian isotropic kernel with l_2^ε penalization the errors are above 1, which indicates that even the arithmetic mean is a better predictor than this particular model. Among the models with the smallest errors are anisotropic Matern 5/2 with both l_1^ε and l_2^ε penalizations and anisotropic Gaussian with l_1^ε penalization. Surprisingly, the model with Matern 5/2 isotropic kernel which

uses the l_1^ε penalization can be seen as a stable model with errors decreasing along with the increase of sampling size K.

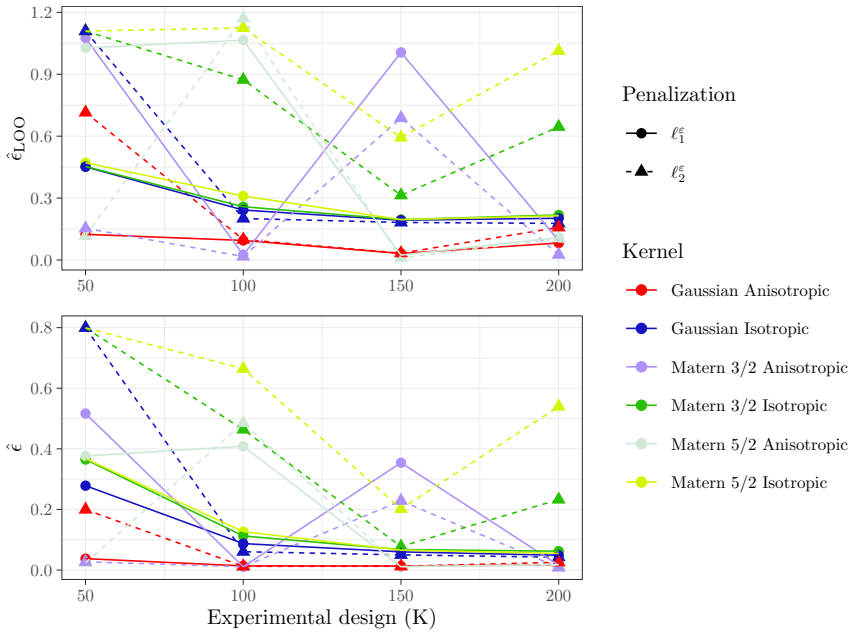


Figure 4.5: The errors $\hat{\epsilon}_{\text{LOO}}$ and $\hat{\epsilon}$ of SVM models for λ.

Similar situation as in Fig. 4.4 can be observed in Fig. 4.5. Again the models behave in an unstable manner. Here, the most stable models seem to be the Gaussian Anisotropic with l_1^ε penalization. Worse, but also stable are the three isotropic kernels with l_1^ε penalization.

Finally, Fig. 4.6 presents the errors obtained for δ_2. Here, there doesn't seem to be much difference between the different models. All the errors are below 1, and decreasing with increasing K. However, the validation errors are above 0.5.

After comparing the above models, the one that is the most stable is the anisotropic Gaussian kernel with l_1^ε.

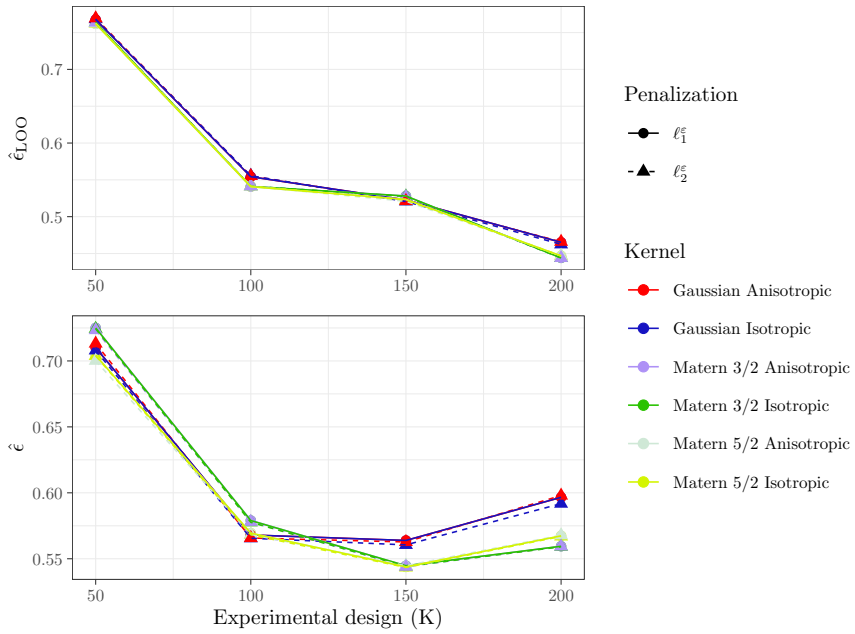


Figure 4.6: The errors $\hat{\epsilon}_{\text{LOO}}$ and $\hat{\epsilon}$ of SVM models for δ_2.

4.3 PC surrogate modelling results

This section presents the errors $\hat{\epsilon}_{\text{LOO}}$ and $\hat{\epsilon}$ for the three sparse PC models. Let us recall that there are 3 different sPC models being developed, where the sparse basis is selected using three algorithms: Least-Angle Regression, Orthogonal Matching Pursuit and Subspace Pursuit. Since all the input variables were sampled from uniform distribution, according to Wiener-Askey scheme the polynomial basis uses Legendre polynomials.

Fig. 4.7 shows the $\hat{\epsilon}_{\text{LOO}}$ and $\hat{\epsilon}$ for δ_1. It can immediately be concluded that the leave-one-out errors are much smaller than in the SVM case, however the validation errors $\hat{\epsilon}$, regardless of being below 1, are not as small as the value of $\hat{\epsilon}_{\text{LOO}}$ would suggest. Moreover, in case of OMP and SP algorithms the error actually increases with increasing number of simulations K, and reaches 0.8 in the case of SP for $K = 200$. This may indicate that the sparse bases created by the OMP and SP algorithms lead to overfitting.

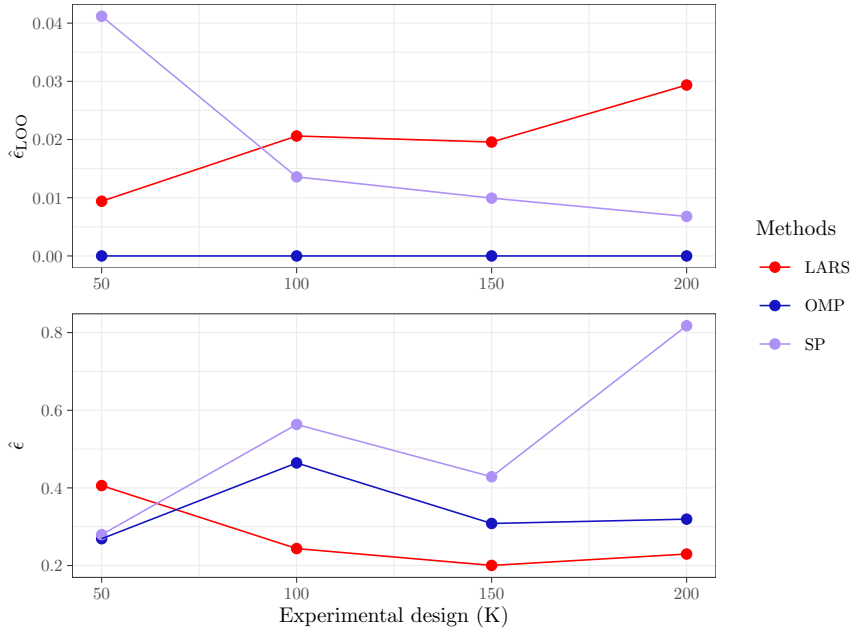


Figure 4.7: The errors $\hat{\epsilon}_{\text{LOO}}$ and $\hat{\epsilon}$ of PC models for δ_1.

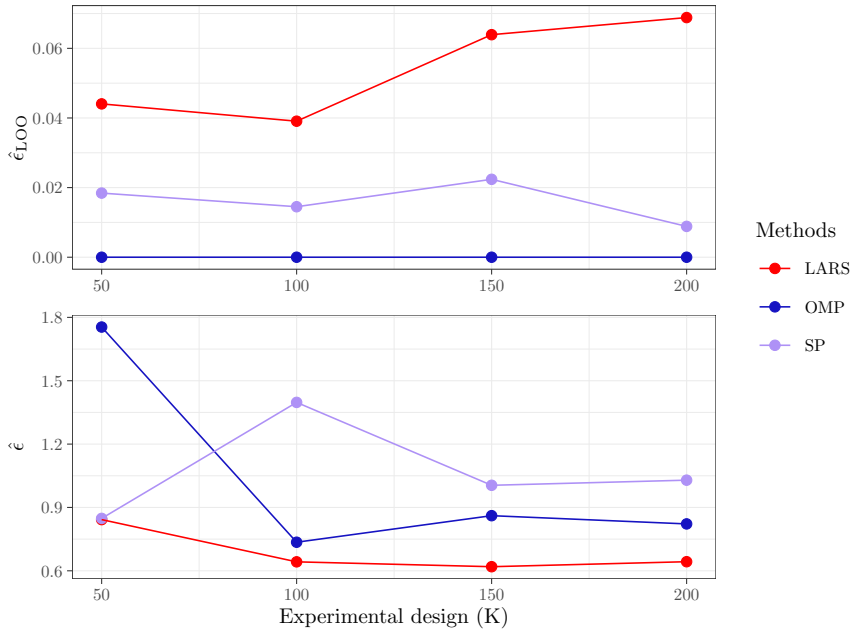


Figure 4.8: The errors $\hat{\epsilon}_{\text{LOO}}$ and $\hat{\epsilon}$ of PC models for v_0.

Further, Fig. 4.8 presents the errors of the sPC models created for v_0. A similar situation can be observed as in the case of δ_1, i.e., despite the leave-one-out errors being small, the *a posteriori* errors are large: for OMP and SP, the values of *a posteriori* errors increase 1. As previously, the most

stable algorithm for creating the basis seems to be LARS, however, even in the case of LARS, the value of $\hat{\epsilon}$ is above 0.6.

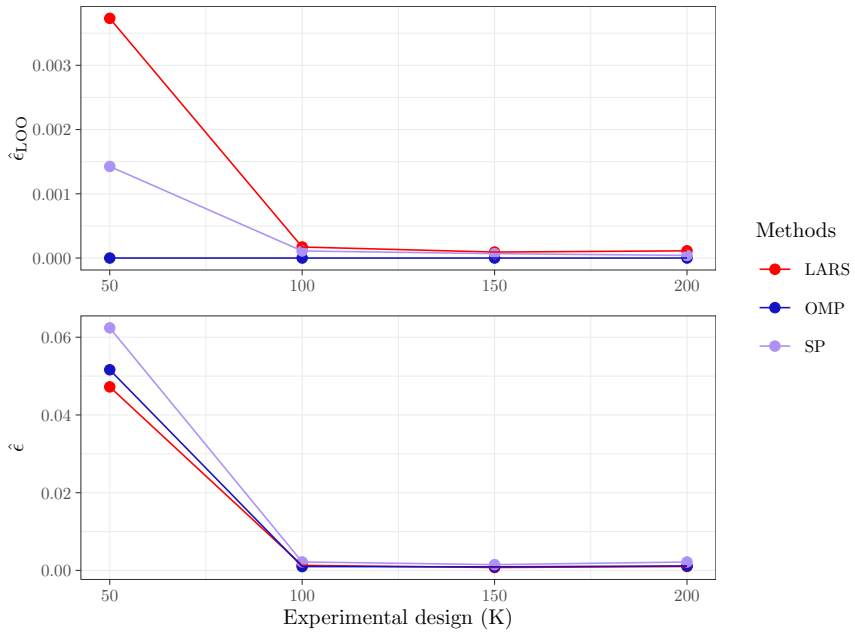


Figure 4.9: The errors $\hat{\epsilon}_{\text{LOO}}$ and $\hat{\epsilon}$ of PC models for f.

Contrary to two previous cases, in the case of frequency f, sPC models with sparse polynomial bases selected by all algorithms have small error. This relates to both the leave-one-out error and the *a posteriori* error. The errors decrease with increasing sampling size and there is not much difference between the different basis selection algorithms. It also does not seem that the models are overfitted, as the *a posteriori* error is close to 0.

Similarly, as shown in Fig. 4.10 the three sPC models created for the decay rate λ have small values of leave-one-out error $\hat{\epsilon}_{\text{LOO}}$ and *a posteriori* error $\hat{\epsilon}$. The smallest values of the *a posteriori* error are reached with the LARS algorithm. Even though the value of $\hat{\epsilon}_{\text{LOO}}$ for LARS increases with increasing the number of samples K, the differences between the errors are on the order of 0.001, i.e. small.

Lastly, Fig. 4.11 presents the models created for δ_2. Again, despite the small

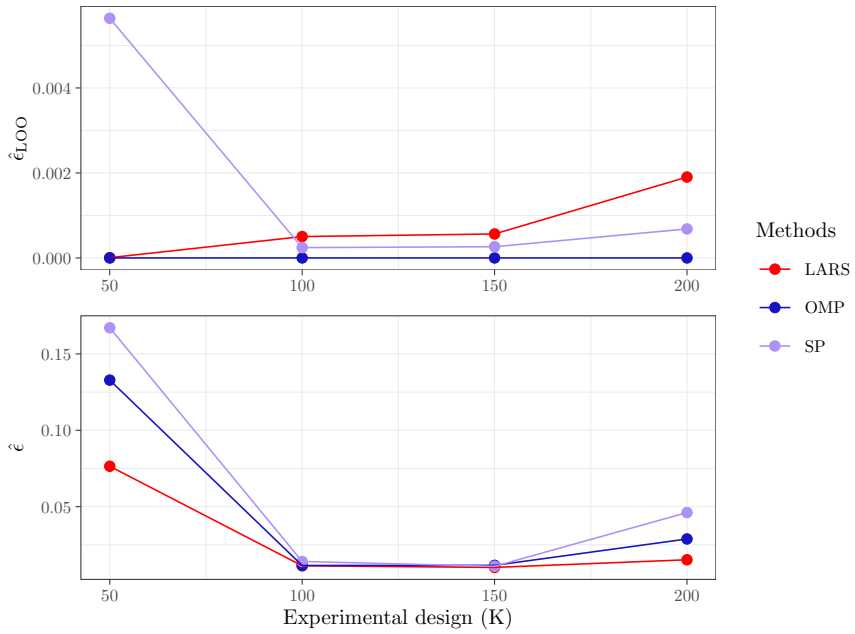


Figure 4.10: The errors $\hat{\epsilon}_{\text{LOO}}$ and $\hat{\epsilon}$ of PC models for λ.

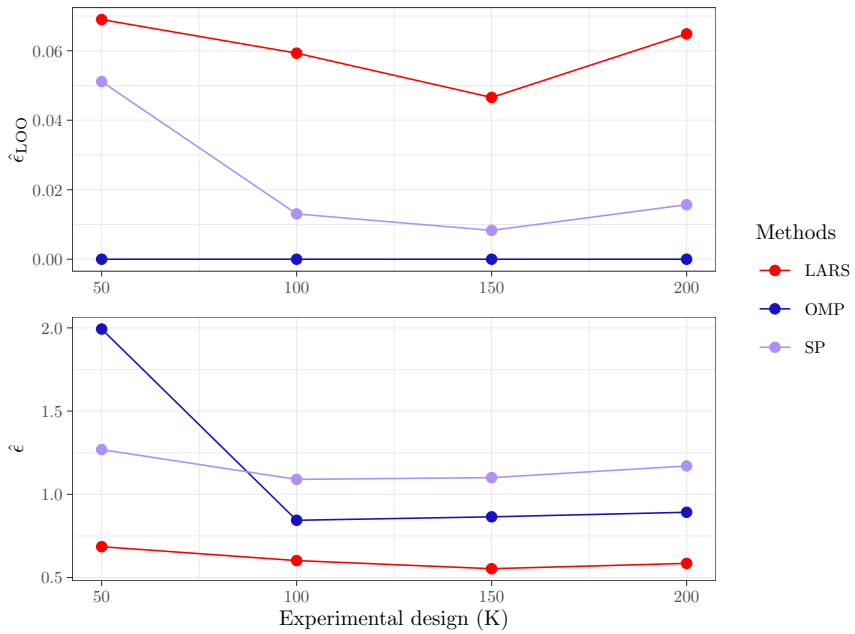


Figure 4.11: The errors $\hat{\epsilon}_{\text{LOO}}$ and $\hat{\epsilon}$ of PC models for δ_2.

values of leave-one-out errors $\hat{\epsilon}_{\text{LOO}}$, the validation errors $\hat{\epsilon}$ exceed 1 with OMP and SP algorithms. The smallest errors are again attained by the PC models with polynomial bases selected with the LARS algorithm, however, they are above 0.5.

Among the created sPC models, the one that behaves in the most stable manner and has the smallest *a posteriori* errors is the one in which sparse basis was created with the usage of LARS algorithm.

4.3.1 Comparison of sPC and SVM

Let us recall that in the case of SVM, the selected model among the studied ones is the one with Gaussian anisotropic kernel function obtained by minimizing the l_1^ε norm. In the case of sPC models, the selected one is the one where the polynomial basis was selected using LARS algorithm. When analysing the *a posteriori* errors, it seems that the highest accuracy (i.e., small *a posteriori* error) were obtained with surrogate models developed for the prediction of the oscillation frequency f as well as the decay rate λ. The surrogate models used for the prediction of maximum amplitude v_0, as well as parameters δ_1 and δ_2 were not as accurate. Even though the models developed for δ_2 are independent of these developed for v_0, f and λ, it is clear that the quality of one of the models is somehow linked to the other, since all the δ_2, are dependent on values of v_0, f and λ. However, one can ask which, among the three parameters v_0, f and λ has the highest influence on δ_2.

Fig. 4.12 presents correlation plots of each of the parameters v_0, f and λ against δ_1 as well as δ_2. Depicted are as well Pearson correlation coefficients ρ for each pair of parameters. It can be immediately recognized that the highest correlation is between δ_2 and v_0 and second highest between δ_1 and v_0. There is no obvious correlation between any of δ_1 and δ_2 and parameters f and λ. This indicates that the quality of surrogate models for v_0 will likely have an impact on the predictions of δ_2 as well as δ_1, even if these models are created independently.

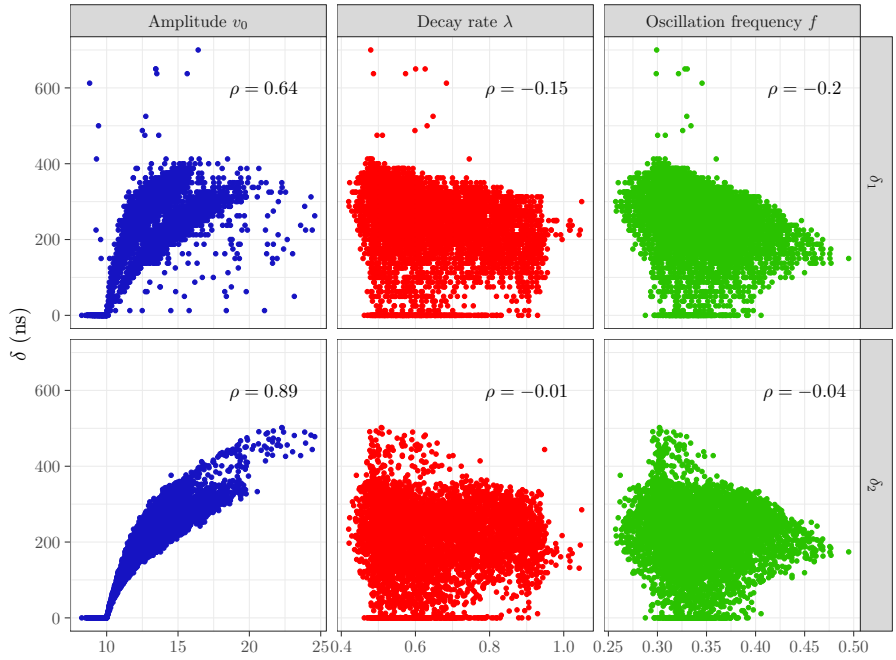


Figure 4.12: Correlation plots between the parameters v_0, f and λ of the damped oscillation, and parameters δ_1 and δ_2, with the Pearson correlation coefficient ρ computed for each pair of parameters.

Further, for the two selected sPC and SVM models developed with $K = 50, 100, 150, 200$, let us consider the empirical cumulative distribution functions (ECDF) and density functions computed from applying the surrogate models on the 5,000 LHS samples. For each model Kolmogorov-Smirnov test was conducted, which tests whether two samples come from the same distribution. In this case, the Kolmogorov-Smirnov statistics D_{SVM} and D_{sPC} were computed between MC ECDF and, respectively, SVM and sPC ECDFs; that is, the MC ECDF was used as a benchmark. The null hypothesis that the distributions are the same was then tested at a significance level $\alpha = 0.05$. If the p-value is smaller that 0.05, the null hypothesis can be rejected in favour of the alternative hypothesis that the two are different.

Fig. 4.13 presents the ECDF and distributions for δ_1. It can be immediately noticed that the null hypothesis that the surrogate model's ECDF is the same as the MC ECDF can be rejected for both SVM and sPC models, re-

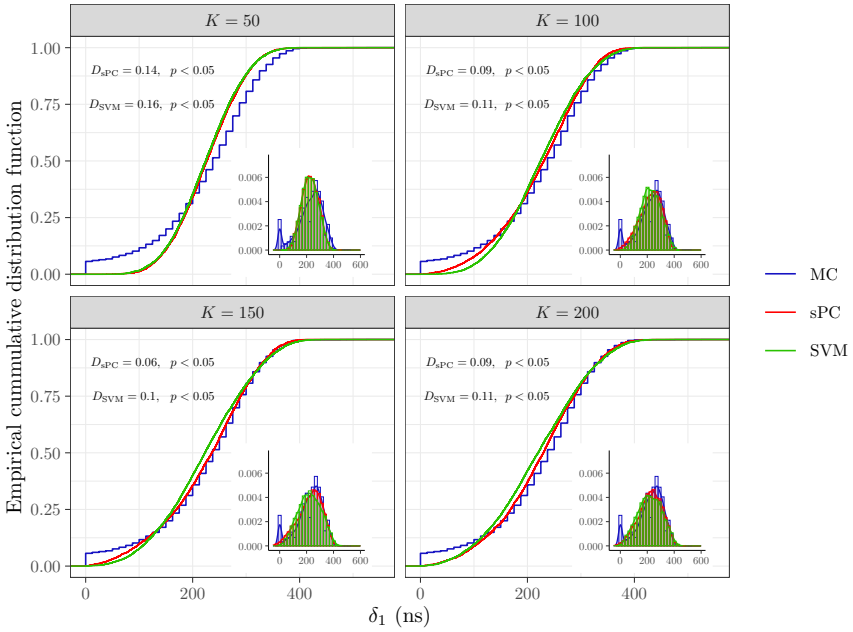


Figure 4.13: The empirical cumulative distribution functions and corresponding approximations of distributions of δ_1 for the MC, sPC and SVM models, for $K = 50, 100, 150, 200$.

gardless of the experimental design size K. Another immediate observation is that the SVM and sPC models did not capture the bi-modal characteristic of δ_1 distribution, where one mode is centred at 0 ns and the other one at 226 ns.

Fig. 4.14 presents ECDFs and distributions for v_0. Here, again in all cases the null hypothesis should be rejected in favour of the alternative. It can be seen that the surrogate models centre around the mode of the distribution, however it seems they do not capture the heavy tails of the MC distribution.

Fig. 4.15 presents ECDFs and distributions for f. Here, the depicted p-values indicate that the null hypothesis that the MC and surrogate model samples come from the same distribution, can be accepted for sPC model for the experimental design size $K = 100, 150, 200$. For the SVM model, null hypothesis can be accepted for $K = 50$ and $K = 200$, which indicates that the sPC model behaves in a more stable way. Indeed, the sPC ECDF

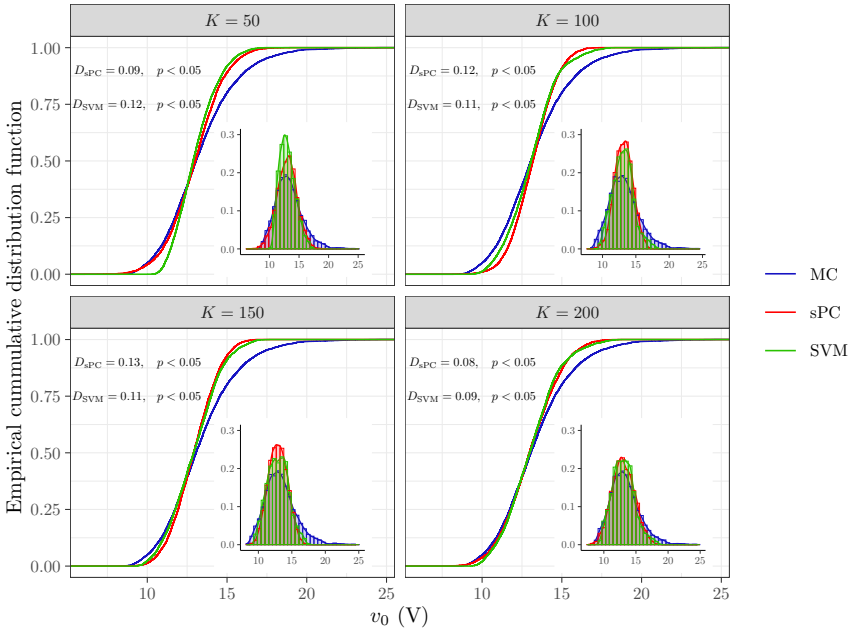


Figure 4.14: The empirical cumulative distribution functions and corresponding approximations of distributions of v_0 for the MC, sPC and SVM models, for $K = 50, 100, 150, 200$.

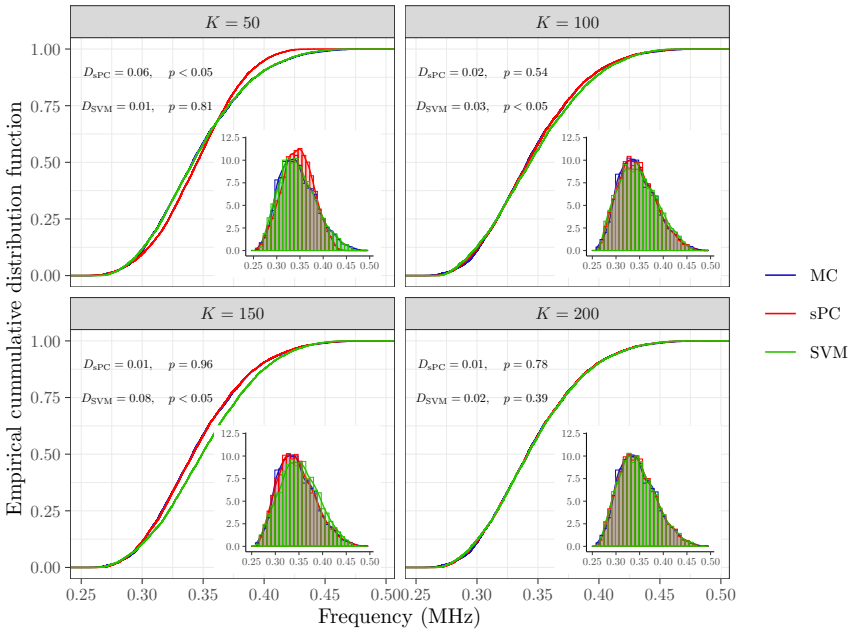


Figure 4.15: The empirical cumulative distribution functions and corresponding approximations of distributions of f for the MC, sPC and SVM models, for $K = 50, 100, 150, 200$.

and density plots are almost indistinguishable from the ones obtained with MC, and the same is true for SVM for $K = 200$.

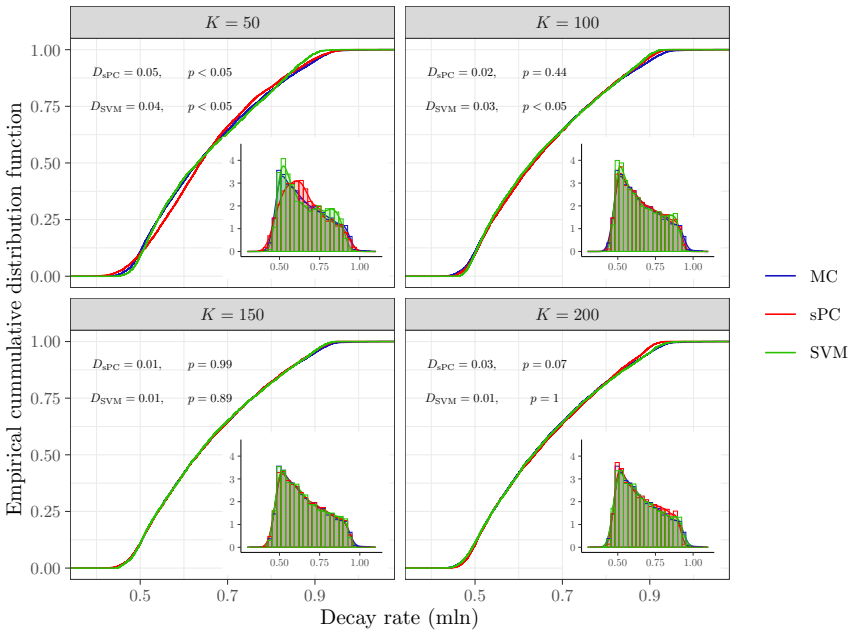


Figure 4.16: The empirical cumulative distribution functions and corresponding approximations of distributions of λ for the MC, sPC and SVM models, for $K = 50, 100, 150, 200$.

Fig. 4.16 shows ECDFs and distributions for the parameter λ. Here, similarly as in the previous case, the p-values indicate that the null hypothesis can be accepted for sPC models for experimental design size $K = 100, 150, 200$. For the SVM models the null hypothesis can be accepted for the design size $K = 150$ and $K = 200$. What is interesting is that both models are able to capture the left-skewed, triangular shape of the distributions.

Finally, Fig. 4.17 shows the ECDFs and distributions for δ_2. Unsurprisingly, just as with δ_1, the p-values indicate that null hypothesis should be rejected for the two surrogate models for each K. In particular, similarly, to δ_1, the surrogate models are not able to capture the overwhelming presence of $\delta_2 = 0$. What is visible is that for the cases where the models perform well, i.e. for f and λ, for sPC the null hypothesis can be accepted consistently for $K = 100, 150, 200$ unlike with SVM. Therefore, for the sensitivity indices,

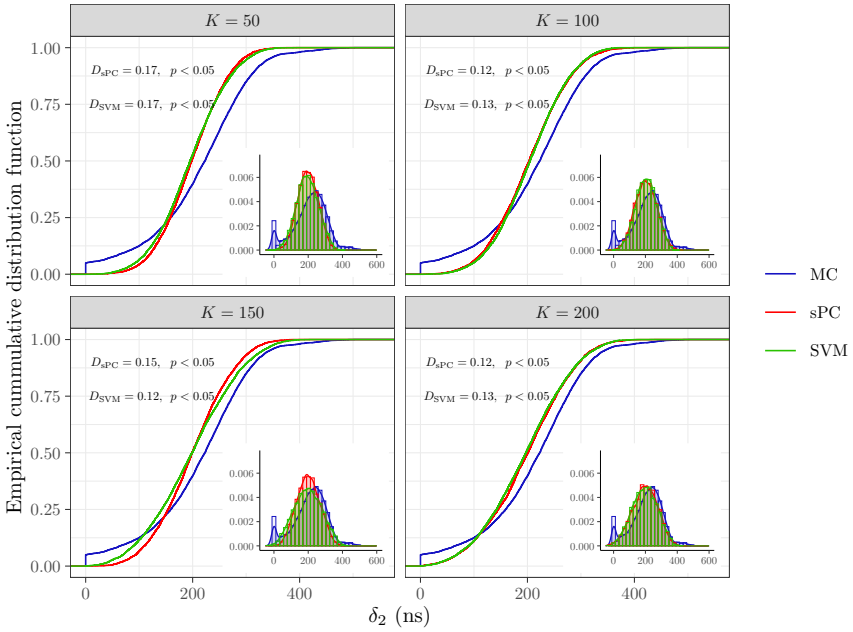


Figure 4.17: The empirical cumulative distribution functions and corresponding approximations of distributions of δ_2 for the MC, sPC and SVM models, for $K = 50, 100, 150, 200$.

only the sPC model will be used.

4.4 Sensitivity analysis

Having selected the best surrogate model, it is now possible to conduct a sensitivity analysis. This will be performed on the basis of Sobol' indices. The sPC models allow to easily extract Sobol' indices (see Appendix D). Here, two types of Sobol' indices are going to be taken into account: *first-order* and *total* Sobol' indices. Let us recall that the *first-order* index show influence of each parameter separately, while the *total* index shows a total contribution of each parameter, including mixed contributions, i.e., contributions due to interactions between parameters.

It should be mentioned that the quality of the Sobol' indices depends on the quality of the surrogate model. Therefore, the sPC models created for

f and λ can be considered the most accurate, while models for v_0, δ_1, and δ_2 should be considered with caution, and any conclusions drawn should be validated afterwards with the help of other techniques.

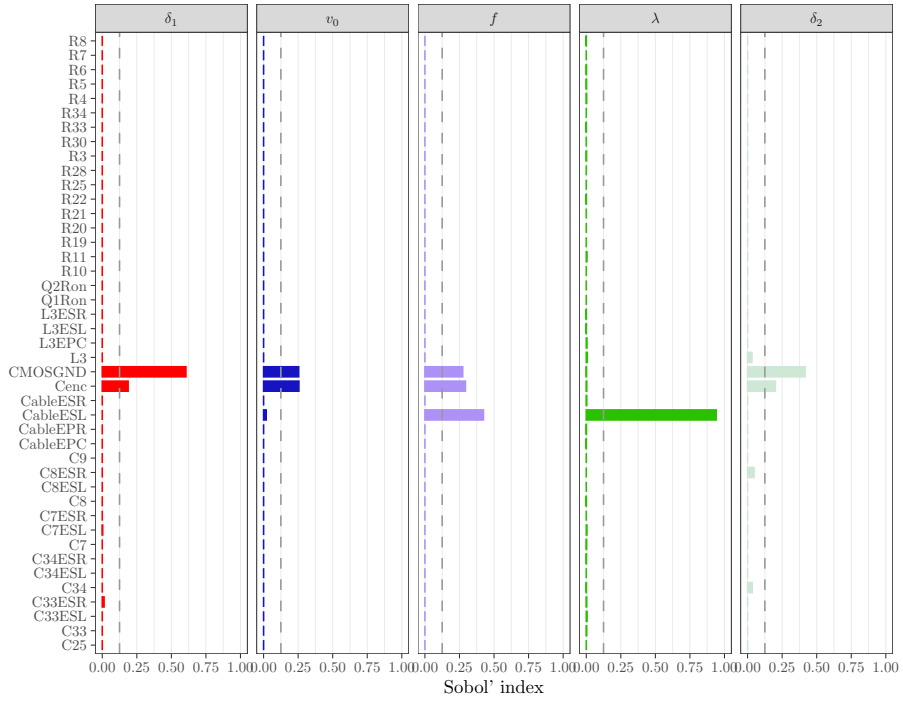


Figure 4.18: First-order Sobol' indices obtained from sPC model.

Fig. 4.18 shows the *first-order* Sobol' indices. The most important information that can be gathered from the plots is that there are only few parameters that have significant influence on the output. These are, respectively, $C_{\text{MOS}\to\text{GND}}$ and C_{enc} for δ_1; $C_{\text{MOS}\to\text{GND}}$ and C_{enc} for v_0; $C_{\text{MOS}\to\text{GND}}$ C_{enc} and L_{cable} for f; and L_{cable} for λ. This means that in order to change the QoI it suffices to play around with these parameters and neglect the other. However, what can also be seen is that in the case of v_0 the two most influential parameters, that is $C_{\text{MOS}\to\text{GND}}$ and C_{enc} sum up to only 0.5. Even though a small influence of the L_{cable} is noticeable, this indicates that there some higher order interactions which are responsible for the remaining ≈ 0.5 influence.

Indeed, the influence of higher order interactions is visible on Fig. 4.19,

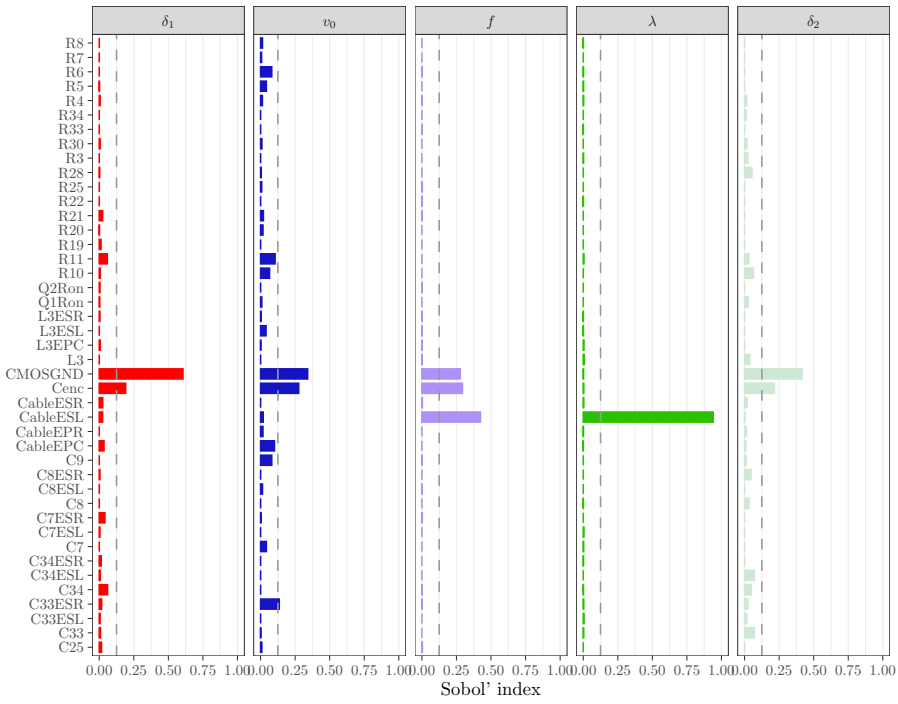


Figure 4.19: Total Sobol' indices obtained from sPC model.

which shows the total Sobol' indices. What can be immediately noticed is that for f and λ there is no visible influence of any other parameters, compared to those obtained from *first-order* indices. However, in the case of δ_1, v_0 and δ_2, it can be observed that the value of Sobol' indices for the remaining parameters is non-negligible, albeit in all cases other than $C_{\text{MOS}\to\text{GND}}$ and C_{enc} it is below 0.0125, indicated with a dashed vertical line on the plot.

Now, having identified the most influential parameters we can cheaply sample from the surrogate models and find out which values of the parameters reduce the interference zones δ. In both Fig. 4.18 and Fig. 4.19 a vertical line indicates the value of 0.0125, which represents a cut-off to select the most important variables. This cut-off value is chosen arbitrarily, and one can select it appropriately to their application.

Following both Fig. 4.18 and Fig. 4.19 for δ_1 and δ_2 the two parameters that are above the cut-off are $C_{\text{MOS}\to\text{GND}}$ and C_{enc}. Moreover, by observing the

correlation plots from Fig. 4.12 it is clear that the best way to obtain $\delta_1 = 0$ and $\delta_2 = 0$ is to reduce the amplitude v_0 below the threshold V_{th}.

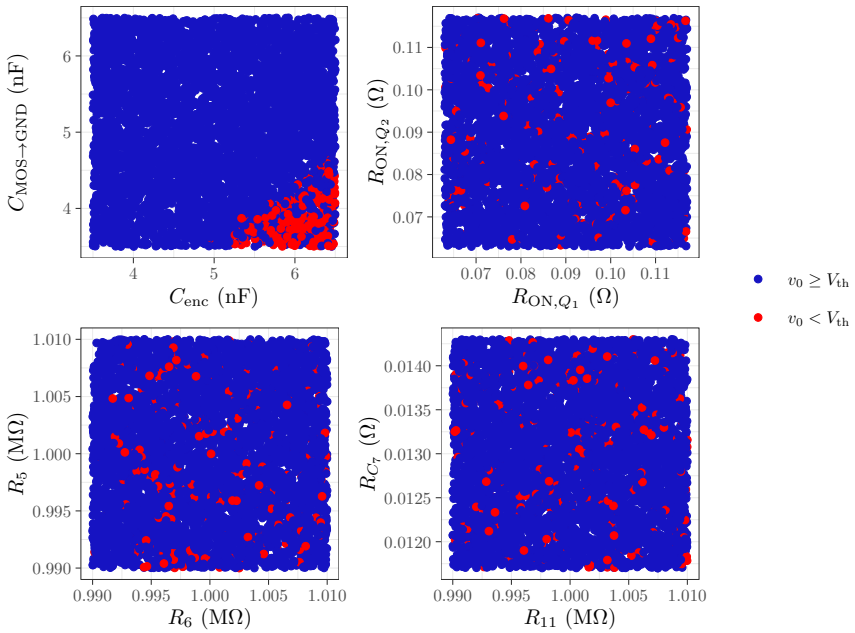


Figure 4.20: 2D scatter plots of selected parameter values obtained from 5,000 LHS samples with indicated $v_0 \geq V_{\text{th}}$ and $v_0 < V_{\text{th}}$.

Fig. 4.20 shows the values of several selected parameters from the validation set of 5,000 LHS samples. Points with red colour indicate the values of the input parameters for which $v_0 < V_{\text{th}}$, while blue colour shows those points where $v_0 \geq V_{\text{th}}$. It can be clearly recognized that for the parameters, which have been recognized as most influential, i.e., $C_{\text{MOS}\to\text{GND}}$ and C_{enc} two classes can be identified and separated; the values for which $v_0 < V_{\text{th}}$ are located in one triangular corner of the plot. For the rest of parameters the two classes are scattered across their entire axes, without clear distinction between the regions.

This shows that it is possible to identify the most important parameters as well as the region for which the value of the amplitude is mostly below the threshold V_{th}, which leads to decreasing the value of δ and as a result decreasing the value of P_{error}.

To validate whether only by changing the values of the parameters $C_{\text{MOS}\to\text{GND}}$ and C_{enc}, the following final MC simulation was conducted.

First, 5,000 LHS samples were drawn and the sPC surrogate models were evaluated for these samples. Using these samples, the data set has been classified into two classes: 1) when $v_0 < V_{\text{th}}$ and 2) when $v_0 \geq V_{\text{th}}$. A simple linear SVM model was built to separate these two classes, as shown in Fig. 4.21. The two classes are clearly distinguishable.

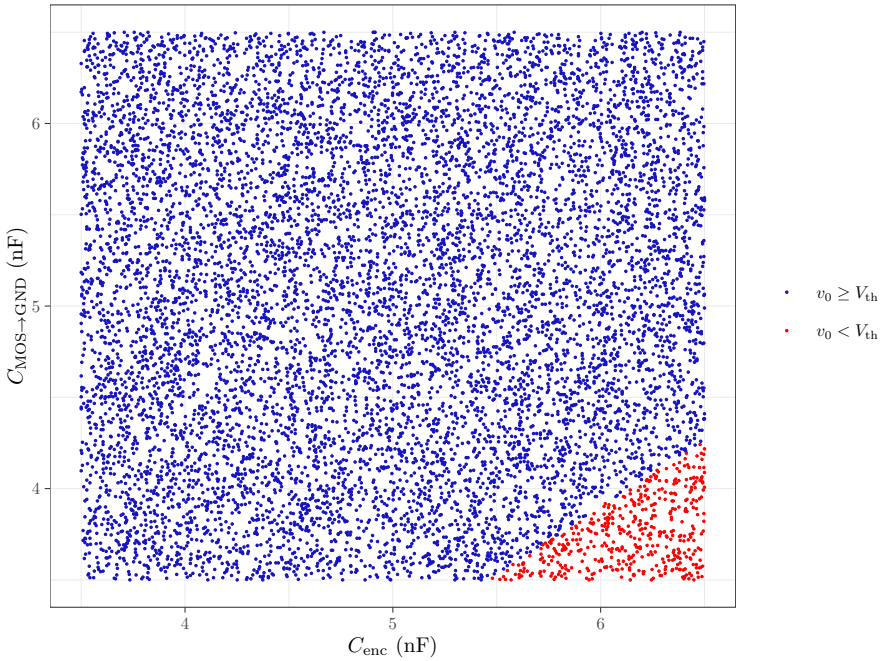


Figure 4.21: Samples of C_{enc} and $C_{\text{MOS}\to\text{GND}}$ obtained from a linear SVM classification model with red and blue colour indicating the two classes.

Next, values of parameters C_{enc} and $C_{\text{MOS}\to\text{GND}}$ were sampled from the region indicated with red colour at Fig 4.21; that is all the sampled points satisfied the following inequalities

$$C_{\text{enc}} \leq \frac{C_2 - C_1}{C_2^* - C_1^*} \left(C_{\text{MOS}\to\text{GND}} - C_2^*\right) + C_2, \tag{4.1}$$

$$C_{\text{enc}} \leq C_2^*, \tag{4.2}$$

$$C_{\mathrm{MOS}\to\mathrm{GND}} \geq C_1, \tag{4.3}$$

where

$$C_1^* = 5.46\,\mathrm{nF}, \tag{4.4}$$

$$C_2^* = 6.50\,\mathrm{nF}, \tag{4.5}$$

$$C_1 = 4.37\,\mathrm{nF}, \tag{4.6}$$

$$C_2 = 3.50\,\mathrm{nF}. \tag{4.7}$$

These values were selected using a simple procedure in which 2,000 LHS samples are first drawn from a smaller cube such that $C_1^* \leq C_{\mathrm{enc}} \leq C_2^*$ and $C_1 \leq C_{\mathrm{MOS}\to\mathrm{GND}} \leq C_2$ and only the portion satisfying inequalities (4.1)–(4.3) is selected, which results in 1024 values.

Next, two types of simulations were conducted. In the first one the remaining 41 input variables were set to their nominal values, listed in Table 3.1, and reused for 1024 simulations. In the second one, for the 41 input variables 1,024 LHS samples were drawn from uniform distribution, as previously using nominal values and tolerances from Table 3.1.

From the simulation parameters δ_1 and δ_2 were obtained and using these parameters values of P_{error} were calculated for both RanM and DetM models.

Results of the two types of simulations are juxtaposed in Tables 4.2 and 4.3. For the one where the 41 input variables were set to the nominal values and only the values of C_{enc} and $C_{\mathrm{MOS}\to\mathrm{GND}}$ were changed we can see that both δ_1 and δ_2 are equal to 0, hence the probabilities of error P_{error} are also equal to 0. This result was repeated few times to account for possible errors. This shows that if parameters of the considered circuit were constant

Table 4.2: The 5%, 25%, 50%, 75%, and 95% quantiles of δ_1 and δ_2 and the average values $\mathrm{E}(\delta_1)$ and $\mathrm{E}(\delta_2)$, as well as the corresponding probabilities of frame rejection P_{error} derived for the RanM and DetM models. The values for C_{enc} and $C_{\text{MOS}\to\text{GND}}$ satisfy conditions (4.1)–(4.3) and nominal values are assumed for the remaining 41 input parameters.

		5%	25%	50%	75%	95%	E(δ)
δ_1 (ns)		0	0	0	0	0	0
P_{error}	RanM	0.00	0.00	0.00	0.00	0.00	0.00
	DetM	0.00	0.00	0.00	0.00	0.00	0.00
δ_2 (ns)		0	0	0	0	0	0
P_{error}	RanM	0.00	0.00	0.00	0.00	0.00	0.00
	DetM	0.00	0.00	0.00	0.00	0.00	0.00

Table 4.3: The 5%, 25%, 50%, 75%, and 95% quantiles of δ_1 and δ_2 and the average values $\mathrm{E}(\delta_1)$ and $\mathrm{E}(\delta_2)$, as well as the corresponding probabilities of frame rejection P_{error} derived for the RanM and DetM models. The values for C_{enc} and $C_{\text{MOS}\to\text{GND}}$ satisfy conditions (4.1)–(4.3) and values for the remaining 41 input parameters are drawn from LHS sampling.

		5%	25%	50%	75%	95%	E(δ)
δ_1 (ns)		0	0	0	47	112	23
P_{error}	RanM	0.00	0.00	0.00	0.2298	0.4640	0.1199
	DetM	0.00	0.00	0.00	0.1064	0.2982	0.0700
δ_2 (ns)		0	0	0	57	138	29
P_{error}	RanM	0.00	0.00	0.00	0.2715	0.5365	0.1488
	DetM	0.00	0.00	0.00	0.1624	0.3702	0.0868

and consistent with their stated nominal values, the parasitics wouldn't have much impact on δ_1 and δ_2. Moreover, one could allow certain values of parasitic capacitance to be present between the circuit and ground, as simulated by the usage of C_{enc} and $C_{\text{MOS}\to\text{GND}}$. However, parasitics do exhibit some uncertain behaviour, therefore the second case shows some more realistic example, in which the values of parasitics are between their stated tolerances. From Table 4.3 we can see that even though non-zero, the probabilities of errors have reduced significantly compared to the original Monte Carlo results. This leads to the conclusion that by creating better models and repeating the same procedure with parameters for which Sobol' indices had non-zero value, one can understand what values of input parameters

(i.e., electrical parameters of the circuit) are allowed in order to reduce the error or even completely mitigate it.

4.5 Discussion

The methodology, results of which are presented in this chapter, allows to identify the most important parameters of the circuit and by selecting them optimize the circuit. In this case what is meant by optimization is that the values of the parameters can be selected such that the influence of the circuit on the probability of P_{error} is reduced. In the presented case the two parameters that were identified as the most important are two parasitic capacitors C_{enc} and $C_{\text{MOS}\rightarrow\text{GND}}$. Usually, according to 'good engineering practice,' an engineer tries to foresee the possible configurations that the PE circuit might be used in and propose mitigation techniques according to their knowledge and intuition, often performing many trial-and-error iterations. On the contrary, the proposed methodology shows that it is possible to incorporate the uncertain conditions in the simulations and instead of using the trial-and-error approach or performing time-consuming MC simulations, one can use the surrogate models, which, albeit not perfectly, allow to identify the problematic elements of the circuit at the early stage.

From this point it is up to an electrical engineer to propose mitigation techniques which result in increasing the EMC of the PE circuit. In this case, it has been shown that there are values of the parasitic capacitances which are allowed for the circuit to reduce its impact on the P_{error}. The question remains whether it is feasible to control the values of this parasitic capacitors in physical circuits. Certainly, the usage of specially designed

filters can help to mitigate the unwanted EMI. It is conceivable that the presented methodology can be used to design these filters and help identify the elements of such filters which would be the most important to mitigate the EMI, therefore reducing cost and time in their design. An experimental validation of the proposed methodology and its implementation in other applications are being currently prepared for a two journal papers.

Chapter 5

Conclusions

This section discusses topics covered in the respective Chapters of this thesis. The contributions of the thesis are recalled from the Introduction. Further, future work is discussed.

5.1 Chapters overview and contributions

In Chapter 1, the introduction to the problems considered in the thesis were introduced. The context of conducted EMI causing problems in communication systems due to the operation of PE converters was discussed. It was presented that the EMI disturbances will be modelled as damped oscillations resulting from the presence of parasitic resonant subcircuits in the PE converters. It was discussed that the parasitic parameters of the circuits exhibit uncertainties in their values, due to various manufacturing and environmental factors. Therefore, to account for the uncertainties, a statistical analysis was postulated as a main object of this thesis.

In Chapter 2, a literature survey was conducted regarding the usage of

RanM to modulate switching of PE converters as a way mitigate EMI. It was shown that the EMI mitigation using RanM is ostensible and results from the measurement procedure adopted in standards. It was argued that in the context of PE converters operating close to serial communication circuits, to achieve EMC compliance, the EMI assessment should focus on evaluating whether the PE converter interrupts the communication, rather than whether the EMI disturbance measured in the frequency domain is below the limits imposed in the standards. Based on the experimental data collected from an experiment using two RS-232/USB converters and a PE half-bridge converter it was observed that if the converter is modulated using a standard DetM with fixed switching frequency the EMI induced on the serial communication causes similar or even smaller number of errors, than when it is modulated using RanM with randomly selected frequencies. The cases for which the two modulation techniques had significantly different impact on the probability of errors were identified using statistical tests. In order to compare the two modulation techniques, two models were recalled, separately for DetM, following [63], and for RanM, following [52]. The model for DetM was then enhanced, by providing direct calculations of the probability of error in several special cases. Furthermore, it was understood and shown why in the case of DetM slight change of the (fixed) switching frequency causes different number of errors to occur; thus, the limitations of the DetM model were indicated and the way to overcome these was proposed. Finally, an average scheme was introduced to compare DetM and RanM with respect to their influence on the probability of errors in the communication scheme. The result showed that the two modulation techniques do not differ in the context of inducing EMI disturbances on the serial communication devices. Therefore, it was concluded that RanM should not be considered as an EMC compliant technique in the case when PE converters influence serial communication signals. In

the authors view, Chapter 2 showed a successful implementation of the Objectives 1 and 2 listed in Section 1.6.

In Chapter 3, the topic of influence of PE converters on the communication systems was taken to a different level. The focus was switched from the probability of errors to the properties of damped oscillations caused by resonant elements in the PE converters; due to the fact that the properties of the damped oscillations influence the probabilities of errors. Two examples of experimental setups where shown in which the presence of uncertain elements, respectively cables of different lengths and capacitors where the capacitance is given with certain tolerance, influence the resonances of the circuits. Then a PE converter was modelled in Matlab Simulink, following the schematic of the Wolfspeed converter used in the experiments, with additional elements representing cables and parasitic capacitances between the circuit and the ground. The simulation model included parasitics as Equivalent Series and Equivalent Parallel Resistances, Inductances and Capacitances. The nominal values and tolerances of the circuit elements and their parasitics were collected directly from the data sheets, indirectly through calculations based on parameters stated in the data sheets, as well as following the work of Sumsurooah *et al.* [94]. The uncertain elements of the circuit were modelled as random variables of uniform distribution. Then, two methods of extracting the time δ, during which the PE circuit can cause errors in the serial communication, were shown. Finally, two surrogate modelling techniques, PC and SVM, were presented. The notion of *a posteriori* error was introduced, and it was shown how the two methods will be compared.

Chapter 4 presented results of the simulations. The surrogate models were created for five quantities of interest:

- v_0 - the amplitude of the damped oscillation,
- f - the oscillation frequency,
- λ - the damping factor,
- δ_1 and δ_2 - the length of the interference zone obtained from two methods discussed in Chapter 3.

The models were created using $K = 50, 100, 150, 200$ input samples, i.e. much less than is required using MC approach. Among the PC models the one where the coefficients were selected using LARS algorithm was chosen to be the best, according to the *a posteriori* error. Among the SVM models the best one was identified as the one which used ℓ_1 penalization function and Gaussian anisotropic kernel. The methods were compared with MC results by the usage of Kolmogorov-Smirnov test and ECDFs. The tests and ECDFs indicated that both methods perform well for predicting the value of f and λ, and worse for predicting v_0, δ_1 and δ_2. It was identified, with the help of correlation plots and Pearson's correlation coefficient that the highest correlation was among the v_0 and δ_1, and v_0 and δ_2. On the basis of this it was understood why, despite the models' good performance for f and λ, their performance on the v_0, δ_1 and δ_2 was worse. Among the two models, the PC model performed better than SVM. Therefore, using the PC model, the sensitivity indices, so-called Sobol' indices were computed, which indicated the most influential parameters of the circuit. It was identified that the most important parameters were two parasitic capacitances C_{enc} and $C_{\text{MOS}\rightarrow\text{GND}}$. This result confirmed the intuition that these two parasitic capacitances allow for the EMI disturbances to occur. Next, the values of these two capacitors were selected in such a way that allowed to reduce the values of the parameters δ_1 and δ_2, and as a result reduce the probability of error P_{error}. The result was confirmed with MC

simulations. It was therefore concluded that with the help of surrogate models and statistical analysis it is possible to optimize the PE circuit, in this case understood in terms of reducing the probability of errors that the PE circuit may induce on a serial communication system. Therefore, the proposed methodology could be used in other applications instead of an 'intuition-based' and 'trial-and-error' methods for optimizing the circuit parameters.

In the authors view, Chapters 3 and 4 successfully answer the objectives 3 and 4 listed in Section 1.6, and as a result, the main objective expressed in Section 1.6 is also achieved.

5.2 Future work

The topics covered in this thesis give rise to many improvements, some of which have already started to be considered by the author of this thesis and his collaborators.

Regarding the improvements of the work presented in Chapter 2, it was clearly stated that the developed models assessing the probability of errors in PE converters operating with RanM and DetM were derived using simple assumptions. These models can therefore be extended to consider more realistic, complex assumptions, in particular varying modulation depths. The analysis presented in Table 2.4 used a brute-force algorithm. If it is not possible to completely mitigate EMI, using expensive filters, it might be possible to apply the approach of the analysis in order to create an algorithm that selects appropriate switching frequencies to mitigate the risk of errors in the serial communication systems. Such an algorithm could be used in real-time systems for the prevention of error occurrence. The

comparison of DetM model, presented in Chapter 2 is needed with other frameworks, in particular that of Li *et al.* in [92], where the authors applied χ^2 tests for inferring errors in serial communication systems disturbed by repetitive (deterministic) EMI disturbances, as well as that of Musoline and Crovetti in [26, 62].

Regarding the topics covered in Chapters 3 and 4, an experimental validation as well as the implementation of the methods to other application is currently being prepared as proposals of two journal papers. Furthermore, it is considered that the parameter δ_2 could be obtained from methods such as Prony's method and Vector Fitting [96–98]. This could potentially improve the quality of surrogate models and allow even smaller number of simulations to be performed, therefore saving time. Next, it is considered that other types of sensitivity indices could be used for the selection of the most influential circuit parameters. In particular, the Kucherenko [103] and Morris indices are considered. The question remains, whether these indices can be computed in fast but reliable manner. By performing preliminary MC simulations not shown in this thesis, it has already been identified that in some cases, the Sobol' indices are close to zero, when its real value is non-zero. This result will be built upon and researched in the future. Furthermore, it is considered that the methodology presented in Chapters 3 and 4 could be used for designing PE circuits and EMI filters. This requires further collaborations with EMC experts.

Finally, as the author of the thesis comes from a mathematical background, two questions regarding the mathematical details behind the PC model are of his concern. The two questions are:

- Having selected the basis $\{\Psi_{\boldsymbol{\alpha}} : \boldsymbol{\alpha} \in \mathcal{A}\}$ and the coefficients $\{c_{\boldsymbol{\alpha}} : \boldsymbol{\alpha} \in \mathcal{A}\}$, now it is easy to compute the mean $\mathrm{E}(\mathcal{M}^{\mathrm{PC}}(\boldsymbol{X}))$ and the

variance $\mathrm{Var}(\mathcal{M}^{\mathrm{PC}}(\boldsymbol{X}))$. Can higher order moments be computed efficiently, or can the resulting distribution be guessed?

- Is it possible to mathematically prove which PC model should be considered to a given task, and what is the optimal selection of the truncation?

Since these questions are more general and abstract, if answered, PC models could be applied to a wide range of EMC and PE-related issues. Until now, any new model needs to be accompanied by MC simulations which confirm its reliability and accuracy.

All the above indications for future work have been already discussed to some extent with existing and potential collaborators. Apart from two journal papers being currently prepared, the mathematical questions posed at the end of this chapter are also being actively researched. Moreover, some approaches using statistical analysis have already been tackled in paper co-authored by the author of this thesis and presented at international EMC conferences [100, 106, 107].

Appendices

Appendix A

Monte Carlo

The EMC community has already recognized the problem of efficient treatment of the uncertain parameters [53]. In many papers, MC methods are used to perform repetitive simulations and asses the QoI, in particular the mean or the standard deviation [108, 109]. The simplicity of MC makes it one of the most popular methods for dealing with any problems which require inclusion of randomness.

The origins of the method date back to the late 1940's, when the experiments with thermal nuclear weapon were taking place in Los Alamos. Metropolis [110] refers that the method was a product of Stanisław Ulam's casual discussions with John von Neumann, who attempted to solve the problem of neutron diffusion in fissile materials using a statistical approach. The name 'Monte Carlo' was proposed by Metropolis himself, acknowledging Ulam's interest in probabilistic games and "not unrelated to the fact that Stan had an uncle who would borrow money from relatives because 'he just had to go to Monte Carlo'"[110].

Despite the singular tense 'method', MC describes in fact a suite of meth-

ods, all of which consist of drawing pseudo-random samples from a given probability distribution. Let X be a random variable, and let us consider a function $f : \mathbb{R} \to \mathbb{R}$. Clearly, $f(X)$ is a random variable. The typical task is then of estimating the expected value $\mathrm{E}\left(f(X)\right)$ by

$$\mathrm{E}(f(X)) = \int_{\mathbb{R}} f(x)p(x)\mathrm{d}x, \tag{A.1}$$

where $p(x)$ is the probability density function associated with the distribution of X.

The simplest form of the Monte Carlo method is based on drawing a random sample $x^{(1)}, \ldots, x^{(n)}$ of n realizations of the random variable X and approximating the expected value $\widehat{\mathrm{E}}(f(X))$ by [111]

$$\widehat{\mathrm{E}}(f(X)) = \frac{1}{n}\sum_{i=1}^{n} f(x^{(i)}). \tag{A.2}$$

By Kolmogorov's law, the estimator $\widehat{\mathrm{E}}(f(X))$ converges to $\mathrm{E}\left(f(X)\right)$ almost surely for $n \to \infty$; however, this convergence can be very slow.

In a more general setting, one might want to know the distribution of the random variable $f(X)$. However, often the complexity of $f(X)$ prevents it from being known analytically. Then, by generating large sample $x^{(1)}, \ldots, x^{(n)}$, we can estimate the probability with an empirical distribution. As a consequence of the Glivenko-Cantelli theorem, for a large enough sample, such empirical distribution converges uniformly to the true distribution [112]. Even then, the required number of samples might be substantial, and therefore Monte Carlo method is often a 'last-resort' or treated as benchmark for developing other techniques [54, 55, 70, 71].

Appendix B

Polynomial Chaos

PC is a method of modelling in which the uncertain output is expressed in terms of orthogonal polynomials. Let $\boldsymbol{X} = (X_1, \ldots, X_n)^T$ be an n-dimensional random variable. PC model can be expressed as follows [101]

$$\mathcal{M}^{\mathrm{PC}}(\boldsymbol{X}) = \sum_{\boldsymbol{\alpha} \in \mathcal{A}} c_{\boldsymbol{\alpha}} \Psi_{\boldsymbol{\alpha}}(\boldsymbol{X}), \tag{B.1}$$

where

- $\mathcal{A} \subset \mathbb{N}^n$ is a set which consists of multi-indices $\boldsymbol{\alpha} = (\alpha_1, \ldots, \alpha_n)$, with α_i indicating the highest degree of polynomial standing next to random variable X_i for any $i = 1, \ldots, n$,
- $\Psi_{\boldsymbol{\alpha}}(\cdot)$ are the orthogonal polynomials,
- $c_{\boldsymbol{\alpha}}$ are the coefficients of the expansion.

The orthogonality of the polynomials $\Psi_{\boldsymbol{\alpha}}$ follows directly from their form

$$\Psi_{\boldsymbol{\alpha}}(\boldsymbol{X}) = \psi_{\alpha_1}(X_1)\psi_{\alpha_2}(X_2)\cdots\psi_{\alpha_n}(X_n), \tag{B.2}$$

where $\psi_{\alpha_1}, \ldots, \psi_{\alpha_n}$ are univariate orthogonal polynomials. For a given $i = 1, \ldots, n$, two polynomials $\psi_\alpha(X_i)$ and $\psi_{\alpha'}(X_i)$ are orthogonal when

$$\langle \psi_\alpha(X_i), \psi_{\alpha'}(X_i) \rangle = \begin{cases} \|\psi_\alpha(X_i)\|, & \text{if } \psi_\alpha(X_i) = \psi_{\alpha'}(X_i), \\ 0, & \text{otherwise,} \end{cases} \tag{B.3}$$

where $\langle \psi_\alpha(X_i), \psi_{\alpha'}(X_i) \rangle$ is the inner product of $\psi_\alpha(X_i)$ and $\psi_{\alpha'}(X_i)$ and $\|\psi_\alpha(X_i)\|$ is the norm of the function $\psi_\alpha(X_i)$. If, additionally, $\|\psi_\alpha(X_i)\| = \|\psi_{\alpha'}(X_i)\| = 1$, we say that $\psi_\alpha(X_i)$ and $\psi_{\alpha'}(X_i)$ are *orthonormal*.

B.1 Selection of polynomial basis: Wiener-Askey scheme

For any $i = 1, \ldots, n$ and some $\alpha, \alpha' \in \mathbb{N}$ the inner product $\langle \psi_\alpha(X_i), \psi_{\alpha'}(X_i) \rangle$ can be expressed as [101]

$$\begin{aligned} \langle \psi_\alpha(X_i), \psi_{\alpha'}(X_i) \rangle &= \mathrm{E}\left(\psi_\alpha(X_i)\psi_{\alpha'}(X_i)\right) \\ &= \int_{\mathbb{R}} \psi_\alpha(x)\psi_{\alpha'}(x)p(x)\mathrm{d}x \end{aligned} \tag{B.4}$$

where $p(x)$ is the probability density function associated with the distribution of random variable X_i. It is easy to see that this definition can be easily extended for the product $\Psi_{\boldsymbol{\alpha}}(\boldsymbol{X})$.

Orthogonal polynomials which satisfy the condition expressed in Eq. (B.3) with respect to an arbitrary distribution can be found using a classical Gram-Schmidt orthonormalization procedure [113], which requires evaluating integrals such as (B.4).

However, a simpler approach exists, known as a Stieltjes procedure, which

takes advantage of a recurrence formula for orthogonal polynomials. Let us recall Eq. (B.2). Further, to focus attention, for some $x \in \mathbb{R}$ consider a sequence of polynomials $\psi_0(x), \psi_1(x), \psi_2(x) \ldots$. Next, for any $d = 1, 2, \ldots$ let $\pi_d(x)$ be a monic[1] polynomial corresponding to $\psi_d(x)$. It can be shown that a sequence of orthogonal polynomials $\psi_0(x), \psi_1(x), \psi_2(x) \ldots$ satisfies the following three-term recurrence formulae [114]

$$\psi_{d+1}(x) = (a_d x + b_d)\psi_d(x) + c_d \psi_{d-1}(x), \tag{B.5}$$

where coefficients a_d, b_d and c_d are given by

$$a_d = \frac{\|\pi_d(x)\|}{\|\pi_{d+1}(x)\|}, \tag{B.6}$$

$$b_d = -\frac{\langle \pi_d(x), x\pi_d(x) \rangle}{\|\pi_d(x)\| \|\pi_{d+1}(x)\|}, \tag{B.7}$$

$$c_d = -\frac{\|\pi_d(x)\|^2}{\|\pi_{d-1}(x)\| \|\pi_{d+1}(x)\|}. \tag{B.8}$$

Stieltjes procedure aims to find these coefficients by recursively solving corresponding integrals and finding corresponding monic polynomials. Integrals can be evaluated numerically by replacing them with a sum, as proposed by Gautschi [115] or applying various quadrature rules, such as Gauss-Kronrod or Chebyshev rules [101, 114].

For several known distributions general formulas for coefficients a_d, b_d and c_d have been derived and can be used to generate families of polynomials. The scheme that offers a polynomial family corresponding to an input probability distribution is known as the Wiener-Askey scheme [116]. Table B.1 juxtaposes the polynomial family names and coefficients a_d, b_d and c_d for selected input distributions. In the work shown in this thesis, it is assumed

[1] A polynomial $\psi(x) = a_n x^n + a_{n-1}x^{n-1} + \ldots + a_1 x + a_0$ is 'monic' if $a_n = 1$. If $a_n \neq 1$, then $\pi(x) = x^n + \frac{a_{n-1}}{a_n}x^{n-1} + \ldots + \frac{a_1}{a_n}x + \frac{a_0}{a_n}$ is a monic polynomial corresponding to $\psi(x)$ for $a_n \neq 0$.

Table B.1: Wiener-Askey scheme for few known distributions.

Distribution	**Polynomial family name**	**Coefficients a_d, b_d, c_d**
Normal $\mathcal{N}(0,1)$	Hermite	$a_d = \frac{1}{\sqrt{d+1}}$ $b_d = 0$ $c_d = -\sqrt{\frac{d}{d+1}}$
Uniform $\mathcal{U}(-1,1)$	Legendre	$a_d = \frac{\sqrt{(2d+1)(2d+3)}}{d+1}$ $b_d = 0$ $c_d = -\frac{d\sqrt{2d+3}}{(d+1)\sqrt{2d-1}}$
Gamma $\Gamma(k,1,0)$	Laguerre	$a_d = \frac{1}{\sqrt{(d+1)(d+k+1)}}$ $b_d = -(2d+k+1)a_d$ $c_d = -\sqrt{(d+k)d}a_d$
Poisson $\mathcal{P}(\lambda)$	Charlier	$a_d = -\frac{1}{\sqrt{\lambda(d+1)}}$ $b_d = \frac{d+\lambda}{\sqrt{\lambda(d+1)}}$ $c_d = -\sqrt{1-\frac{1}{d+1}}$

that all the input random variables follow uniform distributions, therefore, the polynomial family used in for surrogate modelling in Chapters 3 and 4 is the Legendre family.

The first five Legendre polynomials are as follows

$$\psi_0(x) = 1, \tag{B.9}$$

$$\psi_1(x) = x, \tag{B.10}$$

$$\psi_2(x) = \frac{1}{2}\left(-1 + 3x^2\right), \tag{B.11}$$

$$\psi_3(x) = \frac{1}{2}\left(-3x + 5x^3\right), \tag{B.12}$$

$$\psi_4(x) = \frac{1}{8}\left(3 - 30x^2 + 35x^4\right). \tag{B.13}$$

B.2 Finding the coefficients of a PC model

The coefficients $c_{\boldsymbol{\alpha}}$ of the PC model can be found using various techniques. One can broadly classify these methods into *intrusive* and *non-intrusive* [101]. The classical approach, which belongs to the first class of methods, is the so-called 'Galerkin projection' which takes into account the relationship [101]

$$c_{\boldsymbol{\alpha}} = \frac{\langle Y, \Psi_{\boldsymbol{\alpha}}(\boldsymbol{X})\rangle}{\|\Psi_{\boldsymbol{\alpha}}(\boldsymbol{X})\|}, \tag{B.14}$$

for $\boldsymbol{\alpha} \in \mathcal{A}$. The coefficients are found by assuming that Y is a solution to a known differential equation or a product of mathematical operation, such as multiplication, exponentiation, inversion etc. The equation is projected onto the selected orthogonal basis, and results in a system of equations, where the coefficients $c_{\boldsymbol{\alpha}}$ are coupled with countably many other equations. In the EMC world, such approach has been used in [55] to derive per-unit-length inductance and capacitance, and finally assess the mean and standard deviation of far-end voltage for a transmission line model. Since the projection method will not be used in this work, the reader is referred to [101] for more information.

The term *intrusive* rightly suggests that these methods require some form of intrusion into the model, e.g. deriving coupled equations through projection. Unlike *intrusive* methods, the *non-intrusive* ones find the coefficients through evaluating the model 'as-is'. That is, Y can represent the response of a simulation model, which, given sequence $\mathbb{X} = \left(\boldsymbol{x}^{(1)}, \ldots, \boldsymbol{x}^{(K)}\right)$ of K realizations of the random vector $\boldsymbol{X}$ produces outputs $y^{(1)}, \ldots, y^{(K)}$ for some $K \in \mathbb{N}$.

Let us denote $\mathcal{Y} = \left(y^{(1)}, \ldots, y^{(K)}\right)^T$. Coefficients $c_{\boldsymbol{\alpha}}$ can then be obtained from Eq. (B.14) using quadrature rules such as Gaussian quadrature or

Smolyak' sparse quadrature [117], or through Ordinary Least Squares (OLS) technique [101, 102]. In the latter, used in this work, the aim is to find $\widehat{\boldsymbol{c}} = (\widehat{c}_{\boldsymbol{\alpha}_1}, \ldots, \widehat{c}_{\boldsymbol{\alpha}_P})^T$ such that [102]

$$\widehat{\boldsymbol{c}} = \arg\min_{\boldsymbol{c}\in\mathbb{R}^P} \mathrm{E}\left(\mathcal{Y} - \boldsymbol{\Psi}(\mathbb{X})^T\boldsymbol{c}\right)^2, \tag{B.15}$$

where $\boldsymbol{c} = (c_{\alpha_1}, \ldots, c_{\alpha_P})^T$ and

$$\boldsymbol{\Psi}(\mathbb{X}) = \begin{bmatrix} \Psi_{\boldsymbol{\alpha}_1}\left(\boldsymbol{x}^{(1)}\right) & \Psi_{\boldsymbol{\alpha}_2}\left(\boldsymbol{x}^{(1)}\right) & \cdots & \Psi_{\boldsymbol{\alpha}_P}\left(\boldsymbol{x}^{(1)}\right) \\ \Psi_{\boldsymbol{\alpha}_1}\left(\boldsymbol{x}^{(2)}\right) & \Psi_{\boldsymbol{\alpha}_2}\left(\boldsymbol{x}^{(2)}\right) & \cdots & \Psi_{\boldsymbol{\alpha}_P}\left(\boldsymbol{x}^{(2)}\right) \\ \vdots & \vdots & \ddots & \vdots \\ \Psi_{\boldsymbol{\alpha}_1}\left(\boldsymbol{x}^{(K)}\right) & \Psi_{\boldsymbol{\alpha}_2}\left(\boldsymbol{x}^{(K)}\right) & \cdots & \Psi_{\boldsymbol{\alpha}_P}\left(\boldsymbol{x}^{(K)}\right) \end{bmatrix}. \tag{B.16}$$

In the OLS, the solution can be simply derived as [101, 102]

$$\widehat{\boldsymbol{c}} = \left(\boldsymbol{\Psi}(\mathbb{X})^T\boldsymbol{\Psi}(\mathbb{X})\right)^{-1}\boldsymbol{\Psi}(\mathbb{X})^T\mathcal{Y}. \tag{B.17}$$

B.3 Sparse Polynomial Chaos

In the considerations presented above, the number P relates to the cardinality of the set of indices $\mathcal{A}$. A natural question arises as to the magnitude of P, i.e. the number of elements in the polynomial basis. In other words: when should one truncate the PC expansion? A standard approach imposes a maximum total polynomial degree p, and constructs the set $\mathcal{A}$ as the set [103]

$$\mathcal{A} = \{\boldsymbol{\alpha} = (\alpha_1, \ldots, \alpha_n) : \alpha_1 + \cdots + \alpha_n \leq p\}; \tag{B.18}$$

that is, $\mathcal{A}$ indexes the polynomial basis where the sum of degrees of the one-dimensional polynomials is smaller or equal some fixed p. It is easy to see that in such case the cardinality of $\mathcal{A}$ is equal to $P = (n+p)!/(n!p!)$. Moreover, clearly, when the number of variables n increases, the cardinality of $\mathcal{A}$ (and hence, the number of coefficients and complexity of the PC model) increases almost exponentially. Since usually such exponential increase of coefficients leads to an exponential increase in the required number of simulations, there has been many approaches that aim to limit this number. One can apply so-called *hyperbolic truncation scheme* [118], which is based on the idea that the most important interactions between input variables are low-order interactions. In this truncation scheme, the set $\mathcal{A}$ is created as

$$\mathcal{A} = \left\{ (\alpha_1, \ldots, \alpha_n) : \sqrt[q]{\alpha_1^q + \ldots + \alpha_n^q} \leq p \right\}, \tag{B.19}$$

where $0 < q \leq 1$. Moreover, it is often the case that coefficients of the PC expansion are negligibly small, i.e. zero or close to zero [103]. Therefore, only a portion of the coefficients can be selected to create the PC model. A model which uses only a small set of the initial coefficients is called sPC model. A sparse basis of polynomials can be either selected 'manually' by the engineer, who anticipates certain low-order interactions between variables, or can be computed by algorithms such as LARS, OMP, or SP [119].

B.4 PC-based derivation of moments

The orthogonality property of the polynomials in the PC model enables to efficiently derive the mean $\mathrm{E}\left(\mathcal{M}^{\mathrm{PC}}(\boldsymbol{X})\right)$ and variance $\mathrm{Var}\left(\mathcal{M}^{\mathrm{PC}}(\boldsymbol{X})\right)$ of the QoI. Indeed, let us assume that the polynomials $\Psi_{\boldsymbol{\alpha}}$ for $\boldsymbol{\alpha} \in \mathcal{A}$ create an

orthonormal basis. The mean $\mathrm{E}\left(\mathcal{M}^{\mathrm{PC}}(\boldsymbol{X})\right)$ and variance $\mathrm{Var}\left(\mathcal{M}^{\mathrm{PC}}(\boldsymbol{X})\right)$ can be expressed as follows [101]:

$$\mathrm{E}\left(\mathcal{M}^{\mathrm{PC}}(\boldsymbol{X})\right) = c_{(0,\ldots,0)}, \tag{B.20}$$

$$\mathrm{Var}\left(\mathcal{M}^{\mathrm{PC}}(\boldsymbol{X})\right) = \sum_{\boldsymbol{\alpha}\in\mathcal{A}\setminus\{(0,\ldots,0)\}} c_{\boldsymbol{\alpha}}^2. \tag{B.21}$$

That is, the mean value of the PC expansion is the coefficient which corresponds to the constant polynomial $\Psi_{(0,\ldots,0)}$, and the variance of the PC expansion is the sum of all the coefficients squared, except the coefficient corresponding to the constant polynomial $\Psi_{(0,\ldots,0)}$.

Appendix C

Support Vector Machines

SVM is a method which belongs to a class of machine learning techniques, where a predominant task is to create models based on the data rather than the sole knowledge of the underlying physical phenomena [120]. SVM was primarily used for classification tasks, i.e. finding an optimal hyperplane, which would separate distinct classes of observations. However, the idea that stands behind SVM can easily be extended to solve regression problems and as such is known under the name of Support Vector Regression (SVR) [103]. The idea behind SVR is the following: given a data set $\left\{\left(\boldsymbol{x}^{(i)}, y^{(i)}\right) : i = 1, \ldots, K\right\}$ of realizations $\boldsymbol{x}^{(i)}$ of n-dimensional random vector $\boldsymbol{X}$, and corresponding realizations $y^{(i)}$ of random variable Y, find a hyperplane

$$\mathcal{M}^{\mathrm{SVM}}(\boldsymbol{X}) = \boldsymbol{c}^T \boldsymbol{X} + c_0, \tag{C.1}$$

which approximates the functional relationship between $\boldsymbol{x}^{(i)}$ and $y^{(i)}$ for each $i = 1, \ldots, K$, where K is the number of points in the dataset, $\boldsymbol{c} = (c_1, \ldots, c_n)^T$ is the vector of coefficients of the linear combination and c_0 is the bias term.

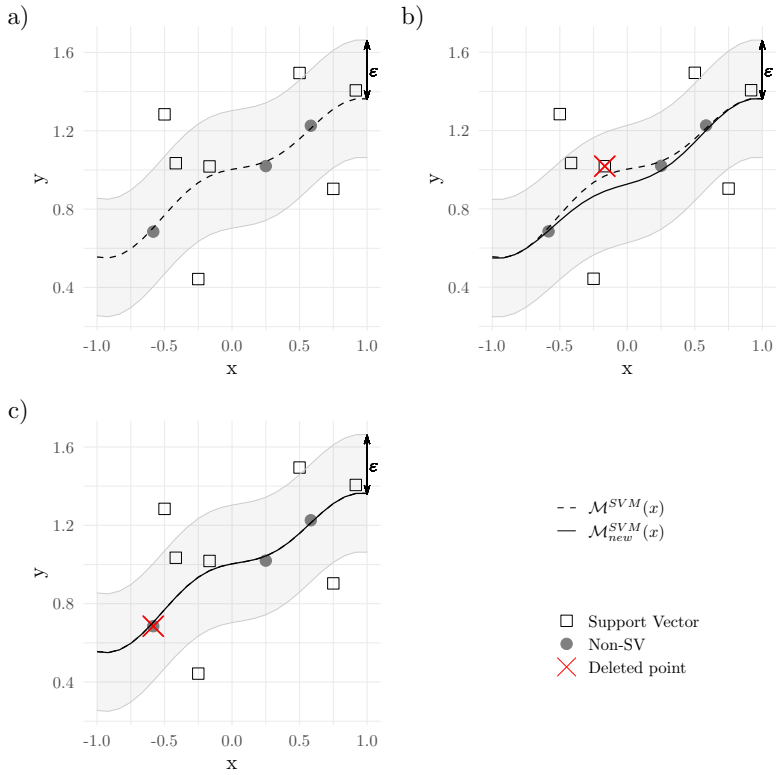


Figure C.1: Visual representation of the ε-parametrized SVM model and support vectors, adopted from [72].

Coefficients $c_0, c_1, \ldots, c_n$ of the SVM model are found by minimizing an error function. Contrary to [70, 71] where the authors consider so-called Least Squares-SVM (LS-SVM), in this work, the two considered formulations are so-called L1 and L2 formulations. The error functions to be minimized, respectively, ℓ_1^ε and ℓ_2^ε, write

$$\ell_1^\varepsilon\left(y - \mathcal{M}^{\mathrm{SVM}}(x)\right) = \begin{cases} 0, & \text{if } |y - \mathcal{M}^{\mathrm{SVM}}(x)| \leq \varepsilon, \\ |y - \mathcal{M}^{\mathrm{SVM}}(x)| - \varepsilon, & \text{otherwise} \end{cases} \tag{C.2}$$

and

$$\ell_2^\varepsilon\left(y - \mathcal{M}^{\mathrm{SVM}}(x)\right) = \begin{cases} 0, & \text{if } |y - \mathcal{M}^{\mathrm{SVM}}(x)| \leq \varepsilon, \\ (|y - \mathcal{M}^{\mathrm{SVM}}(x)| - \varepsilon)^2, & \text{otherwise.} \end{cases} \tag{C.3}$$

Fig. C.1 a) shows the idea behind SVM. The SVM model $\mathcal{M}^{\mathrm{SVM}}(\boldsymbol{X})$, represented by a dashed line, is created from data points $\left(\boldsymbol{x}^{(i)}, y^{(i)}\right)$ which lie inside and outside a shaded zone of width ε. Width parameter ε is present in both L1 and L2 formulations, as seen in equations (C.2) and (C.3). Fig. C.1 b) and c) indicate the importance of so-called *support vectors* (SVs). SVs are significant points, exclusion of one of which results in changing the SVM model. In Fig. C.1 support vectors are indicated by black empty squares, while non-support vectors (Non-SVs) are shown with grey dots. Fig. C.1 b) shows the situation in which a support vector is deleted from the initial dataset. As a result a new SVM model $\mathcal{M}^{\mathrm{SVM}}_{\mathrm{new}}(\boldsymbol{X})$ is built, shown with a solid black line. It is observed that the new model deviates from the original SVM model. In contrary, the exclusion of Non-SV does not lead to changing the SVM model, as depicted in Fig. C.1 c). The excluded point is once again depicted with a red cross and the solid line indicates a newly built SVM model. As it is seen, the new SVM model completely overlaps with the original one. In each case, the SVM regression model uses the same value ε of the width parameter.

C.1 Nonlinearity

In many cases one has to deal with nonlinear behaviour in which a simple hyperplane does not provide a good solution to the problem. One could therefore postulate a mapping $\mathbb{R}^n \ni \boldsymbol{X} \mapsto \phi(\boldsymbol{X}) \in \mathbb{R}^N$ such that the n-dimensional data is mapped onto a N-dimensional *feature* space, with $N > n$, in which a $N-1$-dimensional hyperplane can be found such that the data is well approximated. Such a mapping however may require heavy computations due to the fact that N can be very large.

C.1.1 Kernel trick

To leverage this, one defines the so-called kernel function $k\left(\boldsymbol{X}; \boldsymbol{x}^{(i)}, \boldsymbol{\sigma}\right)$ as

$$k\left(\boldsymbol{X}; \boldsymbol{x}^{(i)}, \boldsymbol{\sigma}\right) = \phi\left(\boldsymbol{x}^{(i)}\right)^T \phi\left(\boldsymbol{X}\right) \tag{C.4}$$

and rephrases the original SVM formulation as follows [120]

$$\mathcal{M}^{\mathrm{SVM}}(\boldsymbol{X}) = \sum_{i=1}^{K} c_i' \, k\left(\boldsymbol{X}; \boldsymbol{x}^{(i)}, \boldsymbol{\sigma}\right) + c_0', \tag{C.5}$$

where c_i' for $i = 1, \ldots, K$ are the (new) coefficients of the linear combination of $k\left(\boldsymbol{X}; \boldsymbol{x}^{(i)}, \boldsymbol{\sigma}\right)$ and c_0' is the (new) bias term.

It has been shown that any function satisfying Mercer's conditions [120] can be used as a kernel function; moreover, many authors derive non-Mercer kernel functions for various tasks [121, 122]. In this work three well-known kernel functions are used:

- Gaussian:

$$k\left(\boldsymbol{X}; \boldsymbol{x}^{(i)}, \sigma\right) = \exp\left(-\frac{\|\boldsymbol{X} - \boldsymbol{x}^{(i)}\|^2}{2\sigma^2}\right),$$

- Matern 3/2:

$$k\left(\boldsymbol{X}; \boldsymbol{x}^{(i)}, \sigma\right) = \left(1 + \sqrt{3}\frac{\|\boldsymbol{X} - \boldsymbol{x}^{(i)}\|}{\sigma}\right) \exp\left(-\sqrt{3}\frac{\|\boldsymbol{X} - \boldsymbol{x}^{(i)}\|}{\sigma}\right),$$

- Matern 5/2:

$$k\left(\boldsymbol{X}; \boldsymbol{x}^{(i)}, \sigma\right) = \left(1 + \sqrt{5}\frac{\|\boldsymbol{X} - \boldsymbol{x}^{(i)}\|}{\sigma}\right) \exp\left(-\sqrt{5}\frac{\|\boldsymbol{X} - \boldsymbol{x}^{(i)}\|}{\sigma}\right) + \frac{5}{3}\frac{\|\boldsymbol{X} - \boldsymbol{x}^{(i)}\|^2}{\sigma^2} \exp\left(-\sqrt{5}\frac{\|\boldsymbol{X} - \boldsymbol{x}^{(i)}\|}{\sigma}\right).$$

In each of the above functions a parameter σ was introduced, which is one

of the hyperparameters that need to be tuned in order to obtain a well-generalized SVM model. Note that the usage of kernel functions does not require evaluating $\phi(\boldsymbol{X})$. This is the so-called *kernel trick.*

C.1.2 Anisotropic kernel functions

All the above kernel functions are called *isotropic,* which means that they do not change with respect the dimension of $\boldsymbol{X}$. However, sometimes a parametrization separate for each dimension is desired. Such kernel is then defined as [103]

$$k\left(\boldsymbol{X}; \boldsymbol{x}^{(i)}, \boldsymbol{\sigma}\right) = \prod_{j=1}^{n} k\left(X_j; x_j^{(i)}, \sigma_j\right), \tag{C.6}$$

where $x_j^{(i)}$ and X_j are the j-th coordinates of, respectively, $\boldsymbol{x}^{(i)}$ and $\boldsymbol{X}$, and $k\left(X_j; x_j^{(i)}, \sigma_j\right)$ is an appropriate kernel function parameterized by σ_j and applied to 1-dimensional points. Kernels defined as in Eq. (C.6) are called *anisotropic.*

C.2 Solving the SVM problem

In order to find the optimal SVM approximation an appropriate minimization problem can be solved. The most convenient way of solving it is by finding the coefficients $\alpha = (\alpha_1, \ldots, \alpha_M)$ and $\alpha^* = (\alpha_1^*, \ldots, \alpha_M^*)$ in the dual space in which the original SVM minimization problem becomes a convex quadratic problem and as such has a unique and global solution. In L1

formulation this optimization problem writes

$$\begin{aligned} \min_{\alpha,\alpha^*} \frac{1}{2} &\begin{bmatrix} \alpha \\ \alpha^* \end{bmatrix}^T \begin{bmatrix} \mathbf{K} & -\mathbf{K} \\ -\mathbf{K} & \mathbf{K} \end{bmatrix} \begin{bmatrix} \alpha \\ \alpha^* \end{bmatrix} \\ &+ \begin{bmatrix} \varepsilon - \mathbf{y} \\ \varepsilon + \mathbf{y} \end{bmatrix}^T \begin{bmatrix} \alpha \\ \alpha^* \end{bmatrix}, \\ \text{subject to } &\begin{bmatrix} \mathbf{1} \\ -\mathbf{1} \end{bmatrix}^T \begin{bmatrix} \alpha \\ \alpha^* \end{bmatrix} = \begin{bmatrix} \mathbf{0} \\ \mathbf{0} \end{bmatrix}, \\ &0 \leq \alpha, \alpha^* \leq H, \end{aligned} \tag{C.7}$$

where $\mathbf{K}$ is a kernel matrix, (i,j)-th element of which is $k(\boldsymbol{x}^{(j)}; \boldsymbol{x}^{(i)}, \sigma)$. Finding the coefficients α and α^* corresponds to finding the parameters $\beta' = (\beta'_1, \ldots, \beta'_M)$ in (C.5). The bias term β_0 can be then retrieved from the coefficients. L2 formulation in the dual space is the following

$$\begin{aligned} \min_{\alpha,\alpha^*} \frac{1}{2} &\begin{bmatrix} \alpha \\ \alpha^* \end{bmatrix}^T \begin{bmatrix} \mathbf{K}^* & -\mathbf{K}^* \\ -\mathbf{K}^* & \mathbf{K}^* \end{bmatrix} \begin{bmatrix} \alpha \\ \alpha^* \end{bmatrix} \\ &+ \begin{bmatrix} \varepsilon - \mathbf{y} \\ \varepsilon + \mathbf{y} \end{bmatrix}^T \begin{bmatrix} \alpha \\ \alpha^* \end{bmatrix}, \\ \text{subject to } &\begin{bmatrix} \mathbf{1} \\ -\mathbf{1} \end{bmatrix}^T \begin{bmatrix} \alpha \\ \alpha^* \end{bmatrix} = \begin{bmatrix} \mathbf{0} \\ \mathbf{0} \end{bmatrix}, \\ &\alpha, \alpha^* \geq 0, \end{aligned} \tag{C.8}$$

where kernel matrix $\mathbf{K}$ has been replaced by

$$\mathbf{K}^* = \mathbf{K} + (1/H)\mathbf{I}, \tag{C.9}$$

with $\mathbf{I}$ being the the identity matrix. Parameter H is another hyperparameter, present in both L1 and L2 formulations. Note that the difference is that in the former, parameter H provides an upper bound for α and α^*, while in the latter case α and α^* are only assumed to be non-negative and H is present in the kernel matrix $\mathbf{K}^*$, where it controls the complexity or 'flatness' of the SVM model.

C.3 Hyperparameter optimization

In the earlier work [72] three hyperparameter optimization algorithms are compared. The parameters that need to be optimized are the width of the error tube ε, complexity parameter H and kernel parameter σ or a set of parameters $\{\sigma_j : j = 1, \ldots, n\}$ in case of anisotropic kernels functions. The optimization algorithms are briefly described below. Each of these algorithms is an iterative algorithm and each stops after reaching a convergence or exceeding a maximum allowed number of iterations.

Broyden–Fletcher–Goldfarb–Shanno (BFGS)

This is an algorithm which belongs to the class of quasi-Newton algorithms. In each step k the search direction s_k is found as a solution to the equation involving the approximation of the Hessian $\widetilde{H}_k$ and gradient ∇f of the error function. Next, an acceptable step in the direction s_k is obtained by performing a 1-dimensional cubic line search. Finally, the hyperparameters and the Hessian are updated. The main advantage of this method over the standard Newton's method is that the inverse of the Hessian approximation $\widetilde{H}_{k+1}^{-1}$ is efficiently derived from previous steps.

Cross-Entropy (CE)

This algorithm selects the best set of hyperparameters by sampling points in the search space. In each step N_{pop} sets of hyperparameters are drawn from a truncated Normal distribution and corresponding SVM models are built. For each model SLOO is computed and N_{SVM} models with the smallest error are selected. Mean and variable of the Normal distribution are updated with a convex combination of the best set of parameters obtained so far and the mean and variance computed from the previously selected N_{SVM} hyperparameters. Sampling and updating procedure is repeated until convergence.

Genetic Algorithm (GA)

The genetic algorithm starts with randomly sampled sets of hyperparameters. In each step an error function is calculated and samples with the smallest errors are chosen as parents. The next generation is obtained both by applying a random 'mutation' to parents and combining the hyperparameters of parents or, in other words, by applying a cross-over.

C.3.1 Error estimate for hyperparameter optimization

In order to tune the hyperparameters some notion of error need to be introduced. The error that will be used is known under the name of span leave-one-out error (SLOO) and in case of L1 formulation writes

$$\hat{\epsilon}_{LOO} = \frac{1}{M}\left(\sum_{i\in\mathcal{I}}(\alpha+\alpha^*)S_i^2 + \sum_{i\in\mathcal{I}}(\xi_i+\xi_i^*)\right) + \varepsilon, \tag{C.10}$$

where ξ_i, ξ_i^* are the so-called slack variables, $\mathcal{I}$ is the set of indices of the support vectors and S_i^2 is the span of support vector $\boldsymbol{x}^{(i)}$. In the L2 formulation the SLOO is reduced to

$$\hat{\epsilon}_{LOO} = \frac{1}{M_{SV}} \left(\sum_{i \in \mathcal{I}} (\alpha + \alpha^*) S_i^2 \right) + \varepsilon, \tag{C.11}$$

where $M_{SV} = |\mathcal{I}|$ indicates the number of support vectors. The reader is referred to [123] for further discussion on computing the span S_i^2.

C.3.2 Selection of the 'best' hyperparameter optimization algorithm

In my earlier work [72], the three hyperparameter optimization algorithms described above were compared. It was identified that the most accurate and the fastest algorithm is BFGS, therefore, for the purpose of this work, only the BFGS algorithm is used to optimize the hyperparameters.

Appendix D

Sensitivity analysis through Sobol' decomposition

Sobol' indices are variance-based measures that among the random variables $X_1, \ldots, X_n$ allow to identify those, which have the highest influence on the QoI. In order to derive Sobol' indices, the function $\mathcal{M}(\boldsymbol{X})$ under consideration has to admit a so-called Sobol' decomposition [105]. Let us assume that random variables $X_1, \ldots, X_n$ have been scaled such that $0 \leq X_i \leq 1$ for each $i = 1, \ldots, n$. A Sobol' decomposition of function $\mathcal{M}(\boldsymbol{X})$ writes [102]

$$\begin{aligned} \mathcal{M}(\boldsymbol{X}) = \mathcal{M}_0 + \sum_{1 \leq i \leq n} \mathcal{M}_i(X_i) + \sum_{1 \leq i < j \leq n} \mathcal{M}_{i,j}(X_i, X_j) \\ + \cdots + \mathcal{M}_{1,2,\ldots,n}(X_1, X_2, \ldots, X_n), \end{aligned} \tag{D.1}$$

where $\mathcal{M}_0 = \mathrm{E}\left(\mathcal{M}(\boldsymbol{X})\right)$ is the expected value of $\mathcal{M}(\boldsymbol{X})$, and for each $1 \leq l \leq k \leq n$ we have

$$\int_0^1 \mathcal{M}_{i_1,\ldots,i_k}(X_{i_1}, \ldots, X_{i_k}) \mathrm{d}X_{i_l} = 0; \tag{D.2}$$

that is, only the expected value $\mathrm{E}\left(\mathcal{M}(\boldsymbol{X})\right)$ is responsible for a constant translation. In order for $\mathcal{M}(\boldsymbol{X})$ to admit Sobol' decomposition, it has to be integrable and random variables $X_1, \ldots, X_n$ have to be mutually independent, i.e. such that the probability of X_i does not depend on the probability of X_j, for all $i, j \in \{1, \ldots, n\}$ and $i \neq j$.

D.1 Sobol' indices

If $\mathcal{M}(\boldsymbol{X})$ admits Sobol' decomposition (D.1) one can compute the sensitivity indices. For each $1 \leq k \leq n$ these indices measure the impact of a group of variables $\{X_{i_1}, \ldots, X_{i_k}\}$ on the output function $\mathcal{M}(\boldsymbol{X})$. More precisely, assessed is the ratio between partial variance which involves random variables $X_{i_1}, \ldots, X_{i_k}$ and the variance D of $\mathcal{M}(\boldsymbol{X})$. The variance D is simply [105]

$$\begin{aligned} D &:= \operatorname{Var} \mathcal{M}(\boldsymbol{X}) \\ &= \left(\int_{[0,1]^n} \mathcal{M}^2(\boldsymbol{X}) \mathrm{d}\boldsymbol{X} \right) - \mathcal{M}_0^2, \end{aligned} \tag{D.3}$$

while for each $1 \leq k \leq n$ partial variances $D_{i_1,\ldots,i_k}$ can be expressed as [105]

$$\begin{aligned} D_{i_1,\ldots,i_k} &= \operatorname{Var} \mathcal{M}_{i_1,\ldots,i_k}(X_{i_1}, \ldots, X_{i_k}) \\ &= \int_0^1 \cdots \int_0^1 \mathcal{M}^2_{i_1,\ldots,i_k}(X_{i_1}, \ldots, X_{i_k}) \mathrm{d}X_{i_1} \cdots \mathrm{d}X_{i_k}. \end{aligned} \tag{D.4}$$

D.1.1 Sensitivity measures

Once the variance D and partial variances $D_{i_1,\ldots,i_k}$ are known, one can compute the sensitivity indices. A sensitivity index $S_{i_1,\ldots,i_k}$ which measures the contribution of a group of random variables $X_{i_1}, \ldots, X_{i_k}$ on $\mathcal{M}(\boldsymbol{X})$ is

defined as the ratio

$$S_{i_1,\ldots,i_k} = \frac{D_{i_1,\ldots,i_k}}{D}. \tag{D.5}$$

Index S_i, for $i = 1, \ldots, n$ corresponding to single variable X_i is called a *first-order* index. Index $S_{i_1,\ldots,i_k}$, which involves more than one random variable is referred to as *higher order* index, respectively second order for two random variables, third order for three random variables, etc. Another notion, used in the analysis presented in this thesis, is that of *total* Sobol' index, which measures the total contribution of a particular random variable X_i. The total Sobol' index S_i^{T} corresponding to the variable X_i is defined as

$$S_i^{\mathrm{T}} = \sum_{\{i_1,\ldots,i_k\} \ni i} S_{i_1,\ldots,i_k}; \tag{D.6}$$

i.e., S_i^{T} takes into account the first order index as well as all higher order indices which involve random variable X_i.

D.2 Estimation of Sobol' indices

Sobol' indices (D.5) can be estimated via Monte Carlo samples [105, 124]. However, as widely known, estimation based on standard MC methods requires a lot of computational overhead, especially if the function $\mathcal{M}(\boldsymbol{X})$ represents a complex time-consuming simulation. In the case of the simulations presented in this work, at least 1,000 MC samples should be collected for each variable, which gives 43,000 simulations in total to compute index for each variable [103]. However, since surrogate models are cheap to evaluate, a possible estimation is through MC evaluations of an SVR or PC model. Few approaches exist which try to estimate sensitivity indices based solely on the analytical form of the underlying surrogate model. In the case of SVR, Wu *et al.* [125] present estimation of Sobol' indices, however de-

rived solely for the case when the underlying SVR model uses Gaussian Radial Basis function. In [126], Cheng and Lu estimate Sobol' indices by creating a PC expansion out of an SVR model. This is possible due to the work of Sudret [127], who proposed calculation of Sobol' indices using PC surrogate model. In PC, due to the known orthogonality property, the variance of $\mathcal{M}(\boldsymbol{X})$ is obtained from Eq. (B.21), while partial variances corresponding to (D.5) can be estimated from [127]

$$\mathrm{Var}\left(\mathcal{M}_{i_1,\ldots,i_k}(X_{i_1},\ldots,X_{i_k})\right) = \sum_{\boldsymbol{\alpha}\in\mathcal{A}_k} \mathcal{M}^2_{\boldsymbol{\alpha}}(\boldsymbol{X}), \tag{D.7}$$

where

$$\mathcal{A}_k = \left\{(\alpha_1,\ldots,\alpha_n) : \forall_{1\le s\le k\le n}\ \alpha_{i_s} > 0\right\}. \tag{D.8}$$

In the case of PC the indices can be shown on a simple example. Let us consider the following PC model for 2 input variables $\boldsymbol{X} = (X_1, X_2)$, where the total truncation scheme has been applied with $p = 3$:

$$\begin{aligned}\mathcal{M}^{\mathrm{PC}}(\boldsymbol{X}) = {} & c_{(0,0)}\Psi_{(0,0)}(\boldsymbol{X}) + c_{(1,0)}\Psi_{(1,0)}(\boldsymbol{X}) \\ & + c_{(2,0)}\Psi_{(2,0)}(\boldsymbol{X}) + c_{(3,0)}\Psi_{(3,0)}(\boldsymbol{X}) \\ & + c_{(0,3)}\Psi_{(0,3)}(\boldsymbol{X}) + c_{(2,1)}\Psi_{(2,1)}(\boldsymbol{X}) \\ & + c_{(1,2)}\Psi_{(1,2)}(\boldsymbol{X}) + c_{(0,2)}\Psi_{(0,2)}(\boldsymbol{X}) \\ & + c_{(0,1)}\Psi_{(0,1)}(\boldsymbol{X}) + c_{(1,1)}\Psi_{(1,1)}(\boldsymbol{X}).\end{aligned} \tag{D.9}$$

Note that in this case the cardinality of $\mathcal{A}$ is equal to $(2+3)!/(3!2!) = 10$. After arranging the terms it is also easy to see that this function admits Sobol' decomposition (D.1), and the respective terms are

$$\begin{aligned}\mathcal{M}_0 &= c_{(0,0)}\Psi_{(0,0)}(\boldsymbol{X}), \\ \mathcal{M}_1(X_1) &= c_{(1,0)}\Psi_{(1,0)}(\boldsymbol{X}) + c_{(2,0)}\Psi_{(2,0)}(\boldsymbol{X})\end{aligned} \tag{D.10}$$

$$+ c_{(3,0)}\Psi_{(3,0)}(\boldsymbol{X}), \tag{D.11}$$

$$\mathcal{M}_2(X_2) = c_{(0,1)}\Psi_{(0,1)}(\boldsymbol{X}) + c_{(0,2)}\Psi_{(0,2)}(\boldsymbol{X}) + c_{(0,3)}\Psi_{(0,3)}(\boldsymbol{X}), \tag{D.12}$$

$$\mathcal{M}_{1,2}(X_1, X_2) = c_{(1,1)}\Psi_{(1,1)}(\boldsymbol{X}) + c_{(2,1)}\Psi_{(2,1)}(\boldsymbol{X}) + c_{(1,2)}\Psi_{(1,2)}(\boldsymbol{X}). \tag{D.13}$$

Next, the variance D can be easily computed from

$$\begin{aligned} D = {} & c^2_{(1,0)} + c^2_{(2,0)} + c^2_{(3,0)} \\ & + c^2_{(0,1)} + c^2_{(0,2)} + c^2_{(0,3)} \\ & + c^2_{(1,1)} + c^2_{(2,1)} + c^2_{(1,2)} \end{aligned} \tag{D.14}$$

and variances D_1, D_2 and $D_{1,2}$ can be computed from

$$D_1 = c^2_{(1,0)} + c^2_{(2,0)} + c^2_{(3,0)}, \tag{D.15}$$

$$D_2 = c^2_{(0,1)} + c^2_{(0,2)} + c^2_{(0,3)}, \tag{D.16}$$

$$D_{1,2} = c^2_{(1,1)} + c^2_{(2,1)} + c^2_{(1,2)}. \tag{D.17}$$

Finally, the sensitivity indices S_1, S_2 and $S_{1,2}$ can be calculated directly using Eq. (D.5). While the total Sobol' indices S_1^{T} and S_2^{T} are simply

$$S_1^{\mathrm{T}} = S_1 + S_{1,2}, \tag{D.18}$$

$$S_2^{\mathrm{T}} = S_2 + S_{1,2}. \tag{D.19}$$

Bibliography

[1] R. W. Erickson and D. Maksimović, "Introduction," in *Fundamentals of Power Electronics*. Boston, MA: Springer US, 2001, pp. 1–10.

[2] A. Yazdani and R. Iravani, "Controlled-frequency vsc system," in *Voltage-Sourced Converters in Power Systems: Modeling, Control, and Applications*. Wiley-IEEE Press, 2010, pp. 245–269.

[3] J. O. Gonzalez, R. Wu, S. Jahdi, and O. Alatise, "Performance and Reliability Review of 650 V and 900 V Silicon and SiC Devices: MOSFETs, Cascode JFETs and IGBTs," *IEEE Transactions on Industrial Electronics*, vol. 67, no. 9, pp. 7375–7385, 2020.

[4] J. Morroni and P. Shenoy, "Understanding the Trade-offs and Technologies to Increase Power Density," April 2023.

[5] N. Mohan, T. M. Undeland, and W. P. Robbins, *Power Electronics: Converters, Applications, and Design*. John Wiley & Sons, 2002.

[6] R. W. Erickson and D. Maksimović, "Principles of steady-state converter analysis," in *Fundamentals of Power Electronics*. Boston, MA: Springer US, 2001, pp. 13–37.

[7] R. Smolenski, *Conducted electromagnetic interference (EMI) in smart grids*, ser. Power Systems. London: Springer-Verlag, 2012.

[8] J. Luszcz, "Conducted emission origins in switch-mode power converters," in *High Frequency Conducted Emission in AC Motor Drives Fed By Frequency Converters: Sources and Propagation Paths*. Wiley-IEEE Press, 2018, pp. 21–44.

[9] B. Zhang and X. Wang, "EMI and EMC of Switching Power Converters," in *Chaos Analysis and Chaotic EMI Suppression of DC-DC Converters*. Wiley-IEEE Press, 2013, pp. 93–108.

[10] C. R. Paul, "Signal Spectra—the Relationship between the Time Domain and the Frequency Domain," in *Introduction to Electromagnetic Compatibility*, K. Chang and C. R. Paul, Eds. John Wiley & Sons, Ltd, 2005, ch. 3, pp. 91–175.

[11] "Directive 2014/30/EU of the European Parliament and of the Council of 26 February 2014 on the harmonisation of the laws of the Member States relating to electromagnetic compatibility," *Official Journal of the European Union*, March 2014.

[12] J. Luszcz and R. Smolenski, "Low frequency conducted emissions of grid connected static converters," *IEEE Electromagnetic Compatibility Magazine*, vol. 4, no. 1, pp. 86–94, 2015.

[13] S. K. Salman, "Introduction to the Smart Grid concept," in *Introduction to the Smart Grid*. 978-1-78561-120-9, 2017, ch. 1, pp. 1–23.

[14] F. Leferink, "Conducted Interference, Challenges and Interference Cases," *IEEE Electromagnetic Compatibility Magazine*, vol. 4, no. 1, pp. 78–85, 2015.

[15] S. Jeschke, A. H. Razavi, J. Loos, and J. Baerenfaenger, "Impact of HV Battery Cables' Emissions on the Signal Integrity of 2-Wire

Ethernet Communication in Automotive Application," in *2019 International Symposium on Electromagnetic Compatibility - EMC EUROPE*, 2019, pp. 754–758.

[16] D. Franco, M. Aguado, C. Pinedo, I. Lopez, I. Adin, and J. Mendizabal, "A Contribution to Safe Railway Operation: Evaluating the Effect of Electromagnetic Disturbances on Balise-to-BTM Communication in Railway Control Signaling Systems," *IEEE Vehicular Technology Magazine*, vol. 16, pp. 104–112, 2021.

[17] Y. Fan, L. Zhang, and K. Li, "EMI and IEMI Impacts on the Radio Communication Network of Electrified Railway Systems: A Critical Review," *IEEE Transactions on Vehicular Technology*, pp. 1–16, 2023.

[18] S. Schaffenroth, H.-P. Schmidt, and A. Kölpin, "Measurement setup for industrial communication techniques under electromagnetic interference," *2022 IEEE Sensors Applications Symposium (SAS)*, pp. 1–6, 2022.

[19] F. Leferink, C. Keyer, and A. Melentjev, "Static energy meter errors caused by conducted electromagnetic interference," *IEEE Electromagnetic Compatibility Magazine*, vol. 5, no. 4, pp. 49–55, 2016.

[20] T. Hartman, B. t. Have, J. Dijkstra, R. Grootjans, N. Moonen, and F. Leferink, "Susceptibility of Static Energy Meters due to Amplifier Clipping Caused by a Rogowski Coil," *IEEE Transactions on Electromagnetic Compatibility*, vol. 64, no. 6, pp. 2024–2032, 2022.

[21] B. t. Have, M. A. Azpúrua, T. Hartman, M. Pous, N. Moonen, F. Silva, and F. Leferink, "Waveform Model to Characterize Time-Domain Pulses Resulting in EMI on Static Energy Meters," *IEEE*

Transactions on Electromagnetic Compatibility, vol. 63, no. 5, pp. 1542–1549, 2021.

[22] B. t. Have, T. Hartman, N. Moonen, and F. Leferink, "Static energy meters and the electrical environment comply to the standards but are not compatible," *IEEE Electromagnetic Compatibility Magazine*, vol. 12, no. 1, pp. 59–68, 2023.

[23] N. Ginot, M. A. Mannah, C. Batard, and M. Machmoum, "Application of power line communication for data transmission over pwm network," *IEEE Transactions on Smart Grid*, vol. 1, no. 2, pp. 178–185, Sep. 2010.

[24] W. E. Sayed, P. Lezynski, R. Smolenski, A. Madi, M. Pazera, and A. Kempski, "Deterministic vs. Random Modulated Interference on G3 Power Line Communication," *Energies*, vol. 14, no. 11, 2021.

[25] W. E. Sayed, P. Lezynski, R. Smolenski, N. Moonen, P. Crovetti, and D. W. P. Thomas, "The Effect of EMI Generated from Spread-Spectrum-Modulated SiC-Based Buck Converter on the G3-PLC Channel," *Electronics*, vol. 10, no. 12, 2021.

[26] P. S. Crovetti and F. Musolino, "Interference of Periodic and Spread-Spectrum-Modulated Waveforms with Analog and Digital Communications," *IEEE Electromagnetic Compatibility Magazine*, vol. 11, no. 2, pp. 73–83, 2022.

[27] Y. Wang, H. Wen, X. Hou, H. Tang, H. Sun, K. Zheng, and S. Li, "Comparison of Differential-Mode and Mixed-Mode Conducted Emission for Household Appliances in Power-Line Communication System," *IEEE Transactions on Electromagnetic Compatibility*, vol. 59, no. 6, pp. 2023–2028, 2017.

[28] M. Basford, "Robust, high-speed intra-vehicular communication networks for the vehicles of tomorrow," July 2021. [Online]. Available: http://eprints.nottingham.ac.uk/64281/

[29] R. Shirai, K. Wada, and T. Shimizu, "Failure protection method for can communication against emi noise generated by switched-mode power supplies," *IEEE Journal of Emerging and Selected Topics in Power Electronics*, vol. 9, no. 5, pp. 6152–6160, 2021.

[30] A. Pena-Quintal, K. Niewiadomski, V. Muneeswaran, S. Greedy, M. Sumner, and D. W. P. Thomas, "The effect of spread spectrum modulation for a buck converter coupled with a single wired communication link," in *2021 IEEE International Joint EMC/SI/PI and EMC Europe Symposium*, 2021, pp. 445–450.

[31] R. Smolenski, private communication, June 2019.

[32] *Electromagnetic Compatibility Regulations 2016*, Statutory guidance, Office for Product Safety and Standards, 2023. [Online]. Available: https://www.gov.uk/government/publications/electromagnetic-compatibility-regulations-2016/electromagnetic-compatibility-regulations-2016-great-britain

[33] K. Mainali and R. Oruganti, "Conducted EMI Mitigation Techniques for Switch-Mode Power Converters: A Survey," *IEEE Transactions on Power Electronics*, vol. 25, no. 9, pp. 2344–2356, 2010.

[34] CENELEC, "Industrial, scientific and medical equipment - Radio-frequency disturbance characteristics - Limits and methods of measurement," *EN 55011:2016*, 2016.

[35] J.-J. Chen, Y.-S. Hwang, C.-S. Jheng, Y.-T. Ku, and C.-C. Yu, "A Low-Electromagnetic-Interference Buck Converter With Continuous-

Time Delta-Sigma-Modulation and Burst-Mode Techniques," *IEEE Transactions on Industrial Electronics*, vol. 65, no. 9, pp. 6860–6869, Sep. 2018.

[36] R. Gamoudi, D. Elhak Chariag, and L. Sbita, "A Review of Spread-Spectrum-Based PWM Techniques—A Novel Fast Digital Implementation," *IEEE Transactions on Power Electronics*, vol. 33, no. 12, pp. 10 292–10 307, Dec 2018.

[37] W.-H. Yang, S.-W. Chiu, C.-C. Kuo, Y.-T. Lin, Y.-J. Lai, H.-W. Chen, Y.-S. Ma, K.-H. Chen, Y.-H. Lin, S.-R. Lin, and T.-Y. Tsai, "A True-Random-Number-Based Pseudohysteresis Controller for Buck DC–DC Converter in High-Security Internet-of-Everything Devices," *IEEE Transactions on Power Electronics*, vol. 35, no. 3, pp. 2969–2978, March 2020.

[38] S. U. Hasan and G. E. Town, "An Aperiodic Modulation Method to Mitigate Electromagnetic Interference in Impedance Source DC–DC Converters," *IEEE Transactions on Power Electronics*, vol. 33, no. 9, pp. 7601–7608, Sep. 2018.

[39] A. Dove, J. Naudé, and I. Hofsajer, "An Argument for the Relationship Between Spectral Spreading and Probability Spreading for EMI-Reduction in DC–DC Converter," *IEEE Transactions on Power Electronics*, vol. 35, no. 2, pp. 1459–1472, Feb 2020.

[40] C.-C. Chou and T.-L. Wu, "Analysis of Peak and Statistical Spectrum of Random Nonreturn-to-Zero Digital Signals," *IEEE Transactions on Electromagnetic Compatibility*, vol. 59, no. 6, pp. 2002–2013, Dec 2017.

[41] R. Wang, Z. Lin, J. Du, J. Wu, and X. He, "Direct Sequence Spread Spectrum-Based PWM Strategy for Harmonic Reduction and Com-

munication," *IEEE Transactions on Power Electronics*, vol. 32, no. 6, pp. 4455–4465, June 2017.

[42] B. Li and D. Mansson, "Effect of Periodicity in Frequency Responses of Networks From Conducted EMI," *IEEE Transactions on Electromagnetic Compatibility*, vol. 59, no. 6, pp. 1897–1905, Dec 2017.

[43] H. Li, Z. Yang, B. Wang, V. G. Agelidis, and B. Zhang, "On Thermal Impact of Chaotic Frequency Modulation SPWM Techniques," *IEEE Transactions on Industrial Electronics*, vol. 64, no. 3, pp. 2032–2043, March 2017.

[44] H.-P. Park, M. Kim, and J.-H. Jung, "Spread Spectrum Technique to Reduce EMI Emission for an LLC Resonant Converter Using a Hybrid Modulation Method," *IEEE Transactions on Power Electronics*, vol. 33, no. 5, pp. 3717–3721, May 2018.

[45] ——, "Spread-Spectrum Technique Employing Phase-Shift Modulation to Reduce EM Noise for Parallel–Series LLC Resonant Converter," *IEEE Transactions on Power Electronics*, vol. 34, no. 2, pp. 1026–1031, Feb 2019.

[46] J. Chen, D. Jiang, Z. Shen, W. Sun, and Z. Fang, "Uniform Distribution Pulsewidth Modulation Strategy for Three-Phase Converters to Reduce Conducted EMI and Switching Loss," *IEEE Transactions on Industrial Electronics*, vol. 67, no. 8, pp. 6215–6226, Aug 2020.

[47] Z. Wang, Y. Xu, P. Liu, Y. Zhang, and J. He, "Zero-Voltage-Switching Current Source Inverter Fed PMSM Drives With Reduced EMI," *IEEE Transactions on Power Electronics*, vol. 36, no. 1, pp. 761–771, Jan 2021.

[48] Y. Shan, X. Pei, T. Sun, M. Zhang, P. Zhou, and D. Jiang, "Space

spread-spectrum strategy for mmc to reduce the conducted emi," *IEEE Transactions on Industrial Electronics*, vol. 69, no. 11, pp. 10 807–10 818, 2022.

[49] C.-H. Moon, C.-J. Chen, and S.-W. Lee, "A Random Modulation Spread-Spectrum Digital PWM for a Low System Clock Digital Buck Converter," *IEEE Access*, vol. 9, pp. 156 663–156 671, November 2021.

[50] P. Lezynski, R. Smolenski, H. Loschi, D. Thomas, and N. Moonen, "A novel method for EMI evaluation in random modulated power electronic converters," *Measurement*, vol. 151, p. 107098, February 2020.

[51] P. Lezynski, "Random Modulation in Inverters With Respect to Electromagnetic Compatibility and Power Quality," *IEEE Journal of Emerging and Selected Topics in Power Electronics*, vol. 6, no. 2, pp. 782–790, 2018.

[52] R. Smolenski, J. Bojarski, A. Kempski, and P. Lezynski, "Time-Domain-Based Assessment of Data Transmission Error Probability in Smart Grids With Electromagnetic Interference," *IEEE Transactions on Industrial Electronics*, vol. 61, no. 4, pp. 1882–1890, May 2014.

[53] C. Christopoulos, "The challenges of numerical modelling in EMC studies," in *2010 Asia-Pacific International Symposium on Electromagnetic Compatibility*, Beijing, 2010, pp. 154–157.

[54] P. Manfredi, D. Vande Ginste, D. De Zutter, and F. G. Canavero, "Generalized Decoupled Polynomial Chaos for Nonlinear Circuits with Many Random Parameters," *IEEE Microwave and Wireless Components Letters*, 2015.

[55] P. Manfredi, D. V. Ginste, I. S. Stievano, D. D. Zutter, and F. G. Canavero, "Stochastic transmission line analysis via polynomial chaos methods: an overview," *IEEE Electromagnetic Compatibility Magazine*, vol. 6, no. 3, pp. 77–84, 2017.

[56] A. H. Beshir, L. Wan, F. Grassi, P. S. Crovetti, X. Liu, X. Wu, W. El Sayed, G. Spadacini, and S. A. Pignari, "Electromagnetic Interference of Power Converter with Random Modulation on the Power Line Communication System," *Electronics*, vol. 10, no. 23, 2021.

[57] A. H. Beshir, W. El Sayed, L. Wan, F. Grassi, P. S. Crovetti, X. Liu, X. Wu, A. Madi, R. Smolenski, and S. A. Pignari, "Influence of Random Modulated Power Converter on G3 Power Line Communication," *Applied Sciences*, vol. 12, no. 11, 2022.

[58] C.-H. Moon, C.-J. Chen, and S.-W. Lee, "A Random Modulation Spread-Spectrum Digital PWM for a Low System Clock Digital Buck Converter," *IEEE Access*, vol. 9, pp. 156 663–156 671, 2021.

[59] J. Chen, D. Jiang, W. Sun, Z. Shen, and Y. Zhang, "A Family of Spread-Spectrum Modulation Schemes Based on Distribution Characteristics to Reduce Conducted EMI for Power Electronics Converters," *IEEE Transactions on Industry Applications*, vol. 56, no. 5, pp. 5142–5157, 2020.

[60] G. Marsala and A. Ragusa, "Spread spectrum in random PWM DC-DC converters by PSO&GA optimized randomness levels," in *2017 IEEE 5th International Symposium on Electromagnetic Compatibility (EMC-Beijing)*, 2017, pp. 1–6.

[61] J. Meng, "Noise Analysis of Power-Line Communications Using Spread-Spectrum Modulation," *IEEE Transactions on Power Delivery*, vol. 22, no. 3, pp. 1470–1476, 2007.

[62] F. Musolino and P. S. Crovetti, "Interference of Spread-Spectrum Modulated Disturbances on Digital Communication Channels," *IEEE Access*, vol. 7, pp. 158 969–158 980, 2019.

[63] R. Smolenski, J. Bojarski, P. Lezynski, and Z. Sadowski, "Diophantine equation based model of data transmission errors caused by interference generated by DC-DC converters with deterministic modulation," *Bulletin of the Polish Academy of Sciences: Technical Sciences*, vol. 64, no. 3, pp. 575–580, September 2016.

[64] L. Ran, S. Gokani, J. Clare, K. J. Bradley, and C. Christopoulos, "Conducted electromagnetic emissions in induction motor drive systems. I. Time domain analysis and identification of dominant modes," *IEEE Transactions on Power Electronics*, vol. 13, no. 4, pp. 757–767, July 1998.

[65] T. Kato, K. Inoue, and K. Nishimae, "Worst-Case Tolerance Analysis for a Power Electronic System by Modified Genetic Algorithms," in *2006 CES/IEEE 5th International Power Electronics and Motion Control Conference*, vol. 2, aug 2006, pp. 1–5.

[66] T. Ding, L. Zhang, R. Trinchero, I. S. Stievano, and F. G. Canavero, "Worst-Case analysis of electrical and electronic equipment via affine arithmetic," in *2017 International Conference on Electromagnetics in Advanced Applications (ICEAA)*, 2017, pp. 991–993.

[67] L. R. A. X. De Menezes, D. W. P. Thomas, C. Christopoulos, A. Ajayi, and P. Sewell, "The use of Unscented Transforms for statistical analysis in EMC," in *2008 International Symposium on Electromagnetic Compatibility - EMC Europe*, 2008, pp. 1–5.

[68] P. M. Ivry, O. A. Oke, D. W. P. Thomas, and M. Sumner, "Predicting conducted emissions of multiple VSCs using dimension reduction

technique," in *2015 IEEE International Symposium on Electromagnetic Compatibility (EMC)*, aug 2015, pp. 213–218.

[69] M. Ferber, A. Korniienko, G. Scorletti, C. Vollaire, F. Morel, and L. Krähenbühl, "Systematic LFT Derivation of Uncertain Electrical Circuits for the Worst-Case Tolerance Analysis," *IEEE Transactions on Electromagnetic Compatibility*, vol. 57, no. 5, pp. 937–946, oct 2015.

[70] R. Trinchero, P. Manfredi, I. S. Stievano, and F. G. Canavero, "Machine learning for the performance assessment of high-speed links," *IEEE Transactions on Electromagnetic Compatibility*, 2018.

[71] R. Trinchero, M. Larbi, H. M. Torun, F. G. Canavero, and M. Swaminathan, "Machine Learning and Uncertainty Quantification for Surrogate Models of Integrated Devices With a Large Number of Parameters," *IEEE Access*, vol. 7, pp. 4056–4066, 2019.

[72] K. Niewiadomski, S. Sumsurooah, and D. W. P. Thomas, "Comparison of Selected Support Vector Machine Approaches for Stochastic Power Electronic Circuit Simulation with Parasitics," in *2021 IEEE International Joint EMC/SI/PI and EMC Europe Symposium*, 2021, pp. 591–596.

[73] K. Niewiadomski, R. Smolenski, P. Lezynski, J. Bojarski, D. W. P. Thomas, and F. Blaabjerg, "Comparative Analysis of Deterministic and Random Modulations Based on Mathematical Models of Transmission Errors in Series Communication," *IEEE Transactions on Power Electronics*, vol. 37, no. 10, pp. 11 985–11 995, 2022.

[74] K. Niewiadomski, A. Pena-Quintal, D. W. Thomas, and S. Sumsurooah, "Sensitivity analysis of parasitics in power electronic circuit

through sobol' indices," in *2021 Asia-Pacific International Symposium on Electromagnetic Compatibility (APEMC)*, 2021, pp. 1–4.

[75] K. Niewiadomski, P. Leżyński, R. Smoleński, J. Bojarski, M. Sumner, and D. W. P. Thomas, "Time-domain Assessment of Data Transmission Errors in Systems with Multiple DC/DC Converters," in *2020 International Symposium on Electromagnetic Compatibility - EMC EUROPE*, 2020, pp. 1–6.

[76] J. Balcells, A. Santolaria, A. Orlandi, D. Gonzalez, and J. Gago, "EMI Reduction in Switched Power Converters Using Frequency Modulation Techniques," *IEEE Transactions on Electromagnetic Compatibility*, vol. 47, no. 3, pp. 569–576, 2005.

[77] H. Loschi, P. Lezynski, R. Smolenski, D. Nascimento, and W. Sleszynski, "FPGA-Based System for Electromagnetic Interference Evaluation in Random Modulated DC/DC Converters," *Energies*, vol. 13, no. 9, May 2020.

[78] M. Kim, H.-P. Park, and J.-H. Jung, "Spread Spectrum Technique With Random-Linear Modulation for EMI Mitigation and Audible Noise Elimination in IH Appliances," *IEEE Transactions on Industrial Electronics*, vol. 69, no. 8, pp. 8589–8593, 2022.

[79] H. Loschi, D. Nascimento, R. Smolenski, W. El Sayed, and P. Lezynski, "Shaping of converter interference for error rate reduction in PLC based smart metering systems," *Measurement*, vol. 203, p. 111946, 2022.

[80] H.-P. Park, M. Kim, J. Baek, M. Kang, and J.-H. Jung, "Spread Spectrum Based Power Line Communication and EM Noise Reduction Technique for Bidirectional HB CLLC Resonant Converter," in

2020 IEEE Energy Conversion Congress and Exposition (ECCE), 2020, pp. 5470–5473.

[81] W. El Sayed, P. Crovetti, N. Moonen, P. Lezynski, R. Smolenski, and F. Leferink, "Electromagnetic Interference of Spread-Spectrum Modulated Power Converters in G3-PLC Power Line Communication Systems," *IEEE Letters on Electromagnetic Compatibility Practice and Applications*, vol. 3, no. 4, pp. 118–122, 2021.

[82] S. Robson and M. Haddad, "A Chirp Spread Spectrum Modulation Scheme for Robust Power Line Communication," *IEEE Transactions on Power Delivery*, vol. 37, no. 6, pp. 5299–5309, 2022.

[83] X. He, R. Wang, J. Wu, and W. Li, "Nature of power electronics and integration of power conversion with communication for talkative power," *Nature Communications*, vol. 11, no. 2479, 2020.

[84] C. E. Shannon, "A Mathematical Theory of Communication," *The Bell System Technical Journal*, vol. 27, no. 3, July 1948.

[85] P. S. Crovetti and F. Musolino, "Interference of spread-spectrum emi and digital data links under narrowband resonant coupling," *Electronics*, vol. 9, no. 1, 2020.

[86] B. Auinger, B. Deutschmann, and G. Winkler, "Elimination of electromagnetic interference in communication channels by using spread spectrum techniques," in *2017 International Symposium on Electromagnetic Compatibility - EMC EUROPE*, 2017, pp. 1–6.

[87] E. Axell, T. Ranström, S. Linder, K. Wiklundh, and K. Fors, "On the impact of spread spectrum emi on communication performance," in *2022 International Symposium on Electromagnetic Compatibility – EMC Europe*, 2022, pp. 13–18.

[88] R. G. Newcombe, "Interval estimation for the difference between independent proportions: comparison of eleven methods," *Statistics in Medicine*, vol. 17, no. 8, pp. 873–890, April 1998.

[89] B. t. Have, T. Hartman, N. Moonen, and F. Leferink, "Why frequency domain tests like iec 61000-4-19 are not valid; a call for time domain testing," in *2019 International Symposium on Electromagnetic Compatibility - EMC EUROPE*, Sep. 2019, pp. 124–128.

[90] B. J. A. M. van Leersum, R. B. Timens, F. J. K. Buesink, and F. B. J. Leferink, "Time domain methods for the analysis of conducted interference on the power supply network of complex installations," in *2014 International Symposium on Electromagnetic Compatibility*, Sep. 2014, pp. 605–610.

[91] P. Hall, "The Distribution of Means for Samples of Size N Drawn From a Population In Which The Variate Takes Values Between 0 and 1, All Such Values Being Equally Probable," *Biometrika*, vol. 19, no. 3-4, pp. 240–244, December 1927.

[92] K.-J. Li, Y.-Z. Xie, F. Zhang, and Y.-H. Chen, "Statistical Inference of Serial Communication Errors Caused by Repetitive Electromagnetic Disturbances," *IEEE Transactions on Electromagnetic Compatibility*, vol. 62, no. 4, pp. 1160–1168, August 2020.

[93] T. Cover and J. Thomas, *Maximum Entropy.* John Wiley & Sons, Ltd, 2005, ch. 12, pp. 409–425.

[94] S. Sumsurooah, M. Odavic, S. Bozhko, and D. Boroyevich, "Robust Stability Analysis of a DC/DC Buck Converter under Multiple Parametric Uncertainties," *IEEE Transactions on Power Electronics*, 2018.

[95] L. E. Kinsler, A. R. Frey, A. B. Coppens, and J. V. Sanders, *Fundamentals of Acoustics*. Wiley, 2000.

[96] B. Gustavsen and A. Semlyen, "Rational approximation of frequency domain responses by vector fitting," *IEEE Transactions on Power Delivery*, vol. 14, no. 3, pp. 1052–1061, 1999.

[97] A. Gallego, F. Roman, and E. Pineda, "Vector Fitting-Cauchy Method for the Extraction of Complex Natural Resonances in Ground Penetrating Radar Operations," *Algorithms*, vol. 15, no. 7, 2022.

[98] J. Hauer, C. Demeure, and L. Scharf, "Initial results in Prony analysis of power system response signals," *IEEE Transactions on Power Systems*, vol. 5, no. 1, pp. 80–89, 1990.

[99] C. Lataniotis, E. Torre, S. Marelli, and B. Sudret, "UQLab user manual – The Input module," Chair of Risk, Safety and Uncertainty Quantification, ETH Zurich, Switzerland, Tech. Rep., 2021, report # UQLab-V1.4-102.

[100] E. Ballukja, K. Niewiadomski, A. Pena-Quintal, D. W. P. Thomas, S. Sumsurooah, and M. Sumner, "Stochastic Modelling of Power Electronic Converters under Uncertainties," in *2022 IEEE International Symposium on Electromagnetic Compatibility & Signal/Power Integrity (EMCSI)*, 2022, pp. 232–237.

[101] T. J. Sullivan, *Stochastic Galerkin Methods*. Cham: Springer International Publishing, 2015, pp. 251–276.

[102] S. Marelli, N. Lüthen, and B. Sudret, "UQLab user manual – Polynomial chaos expansions," Chair of Risk, Safety and Uncertainty Quantification, ETH Zurich, Switzerland, Tech. Rep., 2022, report UQLab-V2.0-104.

[103] M. Moustapha, C. Lataniotis, S. Marelli, and B. Sudret, *UQLab user manual - Support vector machines for regression, Report UQLab-V1.3-111*, Chair of Risk, Safety & Uncertainty Quantification, ETH Zurich, 2019.

[104] R. Trinchero and F. G. Canavero, "Combining LS-SVM and GP Regression for the Uncertainty Quantification of the EMI of Power Converters Affected by Several Uncertain Parameters," *IEEE Transactions on Electromagnetic Compatibility*, vol. 62, no. 5, pp. 1755–1762, 2020.

[105] I. Sobol, "Sensitivity Estimates for Nonlinear Mathematical Models," *Mathematical Modelling and Computational Experiments*, vol. 4, pp. 407–414, 1993.

[106] E. Ballukja, I. Aitbar, K. Niewiadomski, M. Sumner, D. W. P. Thomas, and R. Smolenski, "Stochastic Approach to Modelling Emissions of Multiple Power Electronic Converters," in *2023 IEEE 7th Global Electromagnetic Compatibility Conference (GEMCCON)*, 2023, pp. 28–28.

[107] E. Ballukja, K. Niewiadomski, D. W. P. Thomas, S. Sumsurooah, M. Sumner, and J. Bojarski, "A statistical approach to predict the low frequency common mode current in multi-converter setups," in *2023 IEEE Symposium on Electromagnetic Compatibility & Signal/Power Integrity (EMC+SIPI)*, 2023, pp. 7–12.

[108] W. S. Davies, "Monte Carlo estimates of incidence of basic access ISDN generated EMI," *Electronics Letters*, vol. 26, no. 14, pp. 2048–2050, jul 1990.

[109] S. K. Goudos, E. E. Vafiadis, and J. N. Sahalos, "Monte Carlo simulation for the prediction of the emission level from multiple sources

inside shielded enclosures," *IEEE Transactions on Electromagnetic Compatibility*, vol. 44, no. 2, pp. 291–308, may 2002.

[110] N. Metropolis, "THE BEGINNING of the MONTE CARLO METHOD," *Los Alamos Science*, 1987.

[111] J. S. Liu, *Introduction and Examples*. New York, NY: Springer New York, 2004, pp. 1–21.

[112] V. N. Vapnik, *Consistency of Learning Processes*. New York, NY: Springer New York, 2000, pp. 35–68.

[113] A. Kostrikin, *Introduction to Algebra*, A. Kostrikin, Ed. Springer New York, 1982.

[114] W. Gautschi, "Orthogonal polynomials: applications and computation," *Acta Numerica*, vol. 5, pp. 45–119, 1996.

[115] ——, "On Generating Orthogonal Polynomials," *SIAM Journal on Scientific and Statistical Computing*, vol. 3, no. 3, pp. 289–317, 1982.

[116] D. Xiu and G. Karniadakis, "The wiener-askey polynomial chaos for stochastic differential equations," *SIAM J. Sci. Comput.*, vol. 24, pp. 619–644, 2002.

[117] T. Gerstner and M. Griebel, "Numerical integration using sparse grids," *Numerical Algorithms*, vol. 18, pp. 209–232, 1 1998.

[118] G. Blatman and B. Sudret, "Adaptive sparse polynomial chaos expansion based on least angle regression," *Journal of Computational Physics*, vol. 230, no. 6, pp. 2345–2367, 2011.

[119] ——, "Efficient computation of global sensitivity indices using sparse polynomial chaos expansions," *Reliability Engineering and System Safety*, 2010.

[120] K. P. Murphy, *Machine Learning: A Probabilistic Perspective*. The MIT Press, 2012.

[121] H. Sahbi, J. Audibert, J. Rabarisoa, and R. Keriven, "Robust matching and recognition using context-dependent kernels," *Proceedings of the 25th International Conference on Machine Learning - ICML '08*, 2008.

[122] C. Gagné, M. Schoenauer, M. Sebag, and M. Tomassini, "Genetic programming for kernel-based learning with co-evolving subsets selection," *Parallel Problem Solving From Nature - PPSN IX*, pp. 1008–1017, 2006.

[123] O. Chapelle, V. Vapnik, O. Bousquet, and S. Mukherjee, "Choosing Multiple Parameters for Support Vector Machines," *Machine Learning*, vol. 46, no. 1, pp. 131–159, 2002. [Online]. Available: https://doi.org/10.1023/A:1012450327387

[124] I. Azzini, T. A. Mara, and R. Rosati, "Comparison of two sets of Monte Carlo estimators of Sobol' indices," *Environmental Modelling & Software*, vol. 144, p. 105167, 2021.

[125] Z. Wu, D. Wang, P. Okolo N, F. Hu, and W. Zhang, "Global sensitivity analysis using a Gaussian Radial Basis Function metamodel," *Reliability Engineering & System Safety*, vol. 154, pp. 171–179, 2016.

[126] K. Cheng and Z. Lu, "Adaptive sparse polynomial chaos expansions for global sensitivity analysis based on support vector regression," *Computers & Structures*, vol. 194, pp. 86–96, 2018.

[127] B. Sudret, "Global sensitivity analysis using polynomial chaos expansions," *Reliability Engineering & System Safety*, vol. 93, no. 7, pp. 964–979, 2008.